# Modeling of Brain Tumors: Effects of Microenvironment and Associated Therapeutic Strategies

by

Gibin George Powathil

A thesis
presented to the University of Waterloo
in fulfillment of the
thesis requirement for the degree of
Doctor of Philosophy
in
Applied Mathematics

Waterloo, Ontario, Canada, 2009

I hereby declare that I am the sole author of this thesis. This is a true copy of the thesis, including any required final revisions, as accepted by my examiners.

I understand that my thesis may be made electronically available to the public.

Gibin George Powathil

# Abstract

Gliomas are the most common and aggressive primary brain tumors. The most common treatment protocols for these brain tumors are combinations of surgery, chemotherapy and radiotherapy. However, even with the most aggressive combination of surgery and radiotherapy and/or chemotherapy schedules, gliomas almost always recur resulting in a median survival time for patients of not more than 12 months. This highly diffusive and invasive nature of brain tumors makes it very important to study the effects of these combined therapeutic strategies in an effort to improve the survival time of patients. It is also important to study the tumor microenvironment, since the complex nature of the cerebral vasculature, including the blood brain barrier and several other tumor-induced conditions such as hypoxia, high interstitial pressure, and cerebral edema affect drug delivery as well as the effectiveness of radiotherapy. Recently, a novel strategy using antiangiogenic therapy has been studied for the treatment of brain tumors. Antiangiogenic therapy interferes with the development of tumor vasculature and indirectly helps in the control of tumor growth. Recent clinical trials suggest that anti-angiogenic therapy is usually more effective when given in combination with other therapeutic strategies.

In an effort to study the effects of the aforementioned therapeutic strategies, a spatio-temporal model is considered here that incorporates the tumor cell growth and the effects of radiotherapy and chemotherapy. The effects of different schedules of radiation therapy is then studied using a generalized linear quadratic model and compared against the published clinical data. The model is then extended to include the interactions of tumor vasculature and oxygen concentration, to explain tumor hypoxia and to study various methods of hypoxia characterizations includ-

ing biomarker estimates and needle electrode measurements. The model predicted hypoxia is also used to analyze the effects of tumor oxygenation status on radiation response as it is known that tumor hypoxia negatively influences the radiotherapy outcome. This thesis also presents a detailed analysis of the effects of heterogenous tumor vasculature on tumor interstitial fluid pressure and interstitial fluid velocity. A mathematical modeling approach is then used to analyze the changes in interstitial fluid pressure with or without antiangiogenic therapy.

# Acknowledgments

First and foremost, I would like to thank God for giving me wisdom and guidance throughout my life.

> I will say of the LORD, "He is my refuge and my fortress
> my God, in whom I trust." Psalm 91.2

I would like to thank my supervisors, Prof. Siv Sivaloganathan and Prof. Mohammad Kohandel for their continuous support throughout my PhD program. Siv has always been there for me to listen and to give advice. He was the one responsible for involving me in this mathematical medicine program in the first place. It was his online talk on Fields webpage that made me curious and became interested in this new area and I found myself joining his group weeks after I came across that online lecture. Mohammad was the one most responsible for helping me finishing the writing of this thesis as well as challenging the research behind it. He taught me how to ask questions and express my ideas, showed me the various ways to approach and solve a problem and most importantly taught me how to write good academic papers. He has been a great friend and mentor, had confidence in me when I doubted myself and brought out new ideas in me.

I would also like to thank Dr. Mike Milosevic (Princess Margaret Hospital, Toronto) for helping me throughout this project with his clinical expertise and for giving me insightful suggestions and advices whenever I needed them the most. I am grateful to Paul FJW Rijken (Department of Radiotherapy, University of Nijmegen, The Netherlands) who provided me with original images of glioma xenograft cross-sections, which I have used in one of the modeling project. A special thanks to Prof. Pino Tenti for teaching me what it takes to become a good researcher as well as a good presenter and for asking me good questions to help me think through my

problems. I am deeply grateful to Prof. Marek Stastna for being very helpful in problems related to numerical computations.

Special thanks go to Prof. Jack Tuszynski, Prof. Matthew Scott, Prof. Marek Stastna and Prof. Paul Marriott for serving as my committee members. Their valuable comments and suggestions are very important in improving the quality of this thesis.

I would like to say "Thank You" to my friend and fellow graduate student, Colin Turner for his relentless help in carefully reviewing and proof reading my papers and the thesis and also for being a wonderful friend. Thanks to my fellow graduate students Colin Phipps and Sean Speziale for co-authorship and stimulating discussions and my office mates Mohammad Alwan and Yanwei Wang for their support during my work on this thesis. Many thanks also to all my dear friends and members of Applied Mathematics department for making my life in here so joyful and meaningful.

I greatly acknowledge the financial support of NSERC, CIHR and assistantships from Applied Mathematics as well as University Graduate Student Office.

Finally, I would like to express my deepest gratitude to my family for being there whenever I needed your support and for your unconditional love and encouragement.

# Dedication

To my dear family

“ Act as if what you do makes a difference. It does” - William James

# Contents

# List of Tables

# List of Figures

# List of Abbreviations

| | |
|---|---|
| **AA** | Anaplastic Astrocytoma |
| **ANOVA** | Analysis of Variance |
| **AUC** | Area Under Concentration Time Curve |
| **BBB** | Blood Brain Barrier |
| **BED** | Biologically Effective Dose |
| **bFGF** | basic Fibroblast Growth Factor |
| **CA-IX** | Carbonic anhydrase IX |
| **CT** | Computed Tomography |
| **CTV** | Clinically Target Volume |
| **DSB** | Double Strand Breaks |
| **EBRT** | External Beam Radiotherapy |
| **F-MISO** | F-fluro-misonidazole |
| **GBM** | Glioblastoma Multiform |
| **GLUT** | Glucose transporters |
| **HF** | Hyperfractionated |
| **HIF1** | Hypoxia inducible factor 1 |
| **GLQ** | Generalized Linear Quadratic |
| **GTV** | Gross Tumor Volume |
| **IR** | Incomplete Repair |

| | |
|---|---|
| **IFP** | Interstitial Fluid Pressure |
| **IFV** | Interstitial Fluid Velocity |
| **LQ** | Linear Quadratic |
| **MLQ** | Modified Linear Quadratic |
| **MRI** | Magnetic Resonance Imaging |
| **MVP** | Micro-Vascular Pressure |
| **NS** | Norton Simmon |
| **ODE** | Ordinary Differential Equation |
| **PDE** | Partial Differential Equation |
| **PET** | Positron emission tomography |
| **VEGF** | Vascular Endothelial Growth Factor |

# Chapter 1

# Introduction

## 1.1 Aim and Outline of the Thesis

The physiological and genetic processes underlying cancer are highly complex and dynamic in nature; cancer cells undergo constant evolution and mutations, making them extremely difficult to control and eliminate. The initiation of some cancers may be due to various reasons such as environmental damage to DNA, exposure to radiation and DNA damage by carcinogens. Although the causes of cancers are not very well understood, the progression and evolution of these lethal diseases is mostly due to the evolutionary and genetic advantages acquired by cancer cells over normal cells [13, 137]. These somatic evolutionary changes underlying cancer often occur as a result of the response of cancer cells toward their rapidly changing, unfavorable microenvironment. Characteristic features of the tumor microenvironment that often help in creating the aggressive phenotype of cancer cells include tumor hypoxia, interstitial fluid pressure and acidosis [132]. Hence, in order to better understand cancer progression and to plan proper treatment protocols, one has to analyze the

microenvironmental changes underlying tumorigenesis and study how they affect various treatment strategies. Mathematical modeling is one of many ways through which such understanding can be gained, by providing a robust framework in which to study cancer progression and its relationship with the microenvironment.

The main focus of this thesis is primarily concerned with gliomas, which are at once the most aggressive and most common primary brain tumors (constituting 50 % of all brain tumors) [76]. Studies are carried out with an underlying objective of using available information from clinical images (such as CT scan and MRI) to model various processes involved in glioma growth and invasion. A schematic outline of the thesis is given in Figure 1.1. This thesis starts with mathematical modeling of glioma growth and associated optimum therapeutic strategies, on a macroscopic level [93]. As various microenvironmental factors are also involved in the multiphase tumorigenesis of gliomas, subsequent studies are focused on examining the roles of hypoxia, vasculature, growth factors and interstitial fluid pressure in determining the effects of cytotoxic and antiangiogenic therapies. With respect to chapters, the thesis is structured in the following manner.

Chapter 2 starts with an introduction to cancer biology, discussing various biological aspects of tumor growth and evolution. Here, tumorigenesis is considered as a multi-step process wherein various genetic and environmental changes occur, giving rise to more aggressive and invasive phenotypes; the role of tumor angiogenesis in cancer metastasis and its contributions towards a rapidly-evolving tumor microenvironment are also discussed in this chapter. As a particular case, we have considered various biological details of gliomas.

Chapter 3 presents a review of mathematical models that have been used in understanding various concepts associated with cancer progression. Here, we discuss previous models that were used to study tumor growth and tumor angiogenesis,

as well as different microenviromental factors such as hypoxia and interstitial fluid pressure. To prepare the reader for the subsequent chapters, modeling details of different therapeutic strategies are also discussed here.

Chapter 4 gives the general framework of our mathematical modeling of glioma growth and invasion by considering a homogenous as well as heterogenous spatio-temporal model. Here, we also discuss parameter estimation techniques and the numerical scheme that is used to simulate the model.

Chapter 5 considers the aforementioned spatio-temporal mathematical model based on proliferation and diffusion of cells and further modifies it by incorporating the effects of radio- and chemo-therapeutic treatments. The effects of different schedules of radiation therapy, including fractionated and hyperfractionated external beam radiatiotherapy, are studied using a generalized linear quadratic model. The results are compared with published clinical data. The results of combination therapy (radiotherapy with temozolomide, a novel chemotherapeutic agent) as proposed in recent clinical trials are also discussed. The model is then used to predict optimal sequencing of postoperative treatments in brain. This chapter is mainly adapted from our paper [93].

Chapter 6 introduces a mathematical model to simulate tumor hypoxia using a known spatial distribution of tumor vasculature obtained from image data. The model is used to analyze the accuracy of polarographic needle electrode readings in quantifying tumor hypoxia, and also to determine the minimum number of measurements required to satisfactorily evaluate tumor oxygenation status and quantify the effects of radiation on hypoxia. An article discussing various results of this chapter is under review for publication [92].

Chapter 7 discusses the effects of heterogenous tumor vasculature in tumor

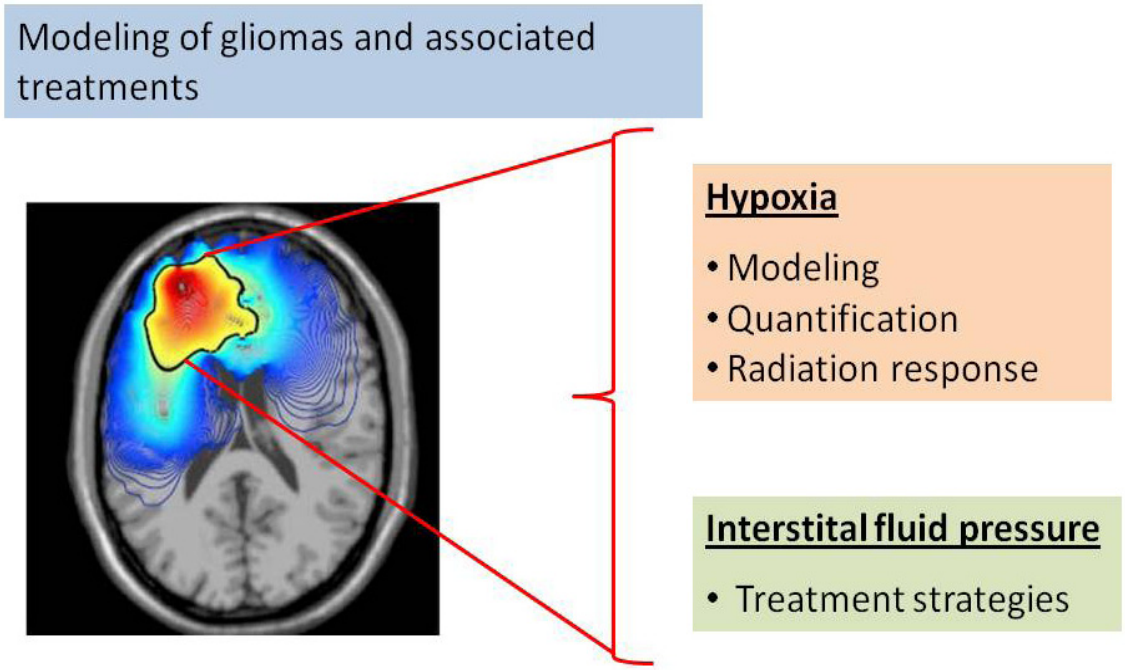


Figure 1.1: Schematic outline of the thesis

interstitial fluid pressure (IFP) and interstitial fluid velocity (IFV) by considering the vascular distributions used in Chapter 6. A dynamic model for IFP is also incorporated in the model to study possible mechanisms for altering tumor IFP. This is achieved by introducing the effects of the surrounding vasculature using an empirically-derived formula in such a way that the resulting profiles are consistent with the experimental data. This work also aims to compare the effects of anti-angiogenic therapy on cancer growth as well as on tumor IFP.

The thesis concludes with a brief discussion of the work and ideas presented, as well as some suggestions of possible directions for the future work.

# Chapter 2

# Introduction to Cancer Biology

## 2.1 Introduction

Cancer is one of the most deadly diseases to beset humanity and is often incurable. It has always pushed our traditional medical knowledge to its limits and still remains a challenge to humanity. While nearly everyone knows someone whose life has been changed or ended by cancer, it is still relevant to ask, what is cancer? Cancer may be viewed as a cellular disease since it represents the collapse of physiological cellular functions normally maintained by a myriad of signaling pathways and cell cycling checkpoints– naturally resulting in uncontrolled growth of cells within the body [137]. It may also be viewed as a genetic disease, since the uncontrolled growth of cells appears to be due the result of genetic alterations or mutations [42]. These genetic changes may be caused by environmental factors, viral infection or other external causes. Moreover, the emergence of clinically-diagnosable cancer through the uncontrolled growth of neoplastic cells usually requires the accumulation of a number of genetic mutations (thus this concept is often referred to as *multi-*

*stage carcinogenesis* [120]). Oncogenes and tumor suppressor genes are two main classes of cancer-related genes, changes to which may lead to cancer initiation and progression. Oncogenes are genes that if up-regulated, may lead to uncontrolled cell proliferation and tumor growth. On the other hand, the inactivation by genetic mutation of tumor suppressor genes that function as cellular "gatekeepers" (act directly) or "caretakers" (indirectly) may cause the formation of a malignant cell [137].

The most common types of cancers include those of the lung, colon, prostate, breast, cervix/ovary and brain. The tumors can originate from epithelial cells (in which case they are called carcinomas) or from bone, cartilage, muscle, fibrous connective tissue or fatty tissue (called sarcomas). Cancer may also develop at the blood or blood forming organs ( called leukemias) or within the lymphatic system of the body (lymphomas). As suggested above the etiologies of tumor formation are varied and are not completely understood. In some cases, tumors remain benign, without causing life-threatening problems, while in malignant cases they invade surrounding tissues (through a process called metastasis) by developing their own blood vessels (angiogenesis). In the latter case, the interactions between the tumor cells and their surrounding tumor microenvironment are extremely important in cancer progression and metastasis [134]. This relationship might be explained through the concept of *somatic evolution of cancer* where the process of cancer initiation and progression are illustrated through evolutionary theory and Darwinian selection [42].

In the Darwinian selection process, the survival of a cell lineage depends on how well it can adapt to its microenvironment [42]. Malignant cells created as a result of multiple mutations have abnormal regulatory mechanisms that bestow an advantage over normal cells. The more oncogenic mutations they acquire, the

better they adapt to their surrounding environments and as a result, cells that grow best will be selected over the less-fit genotypes. Genetic instability, due to various mutations, also plays a vital role in this selection process since the unstable cells may be able to evolve faster and adapt to changing environments and selective barriers more readily than stable cells [13]. In the following sections we will see various microenvironmental factors that affect tumor progression and the ways through which tumor cells adapt to these selective barriers.

## 2.2 Angiogenesis and Metastasis

Tumor angiogenesis is one of the critical steps in tumor development and cancer progression. Through this process, the malignant tumor develops its own vascular network in order to obtain oxygen and nutrients and to grow beyond a relatively small radius of 1 mm. These new blood vessels can either be built from existing local endothelial cells or from recruited endothelial progenitor cells. This creation of new vasculature is determined by a shift in the balance of pro- and anti- angiogenic factors such as vascular endothelial growth factor (VEGF), basic fibroblast growth factor (bFGF), angiostatin and endostatin [52]. In normal tissues these factors remain in balance, while tumor cells shift the balance away from inhibition and in favor of promotion through the excess production of pro-angiogenic factors [96]. Excess production of pro-angiogenic factors may also be due to the tumor cell's response to its abnormal microenvironment, which is often characterized by hypoxia, high interstitial fluid pressure and acidosis. The tumor vascular networks thus created are usually immature and abnormal in nature; this is mostly due to the poor development of vessel walls, lack of pericyte coverage and irregular, structurally abnormal basement membrane. Tumor blood vessels are also very chaotic,

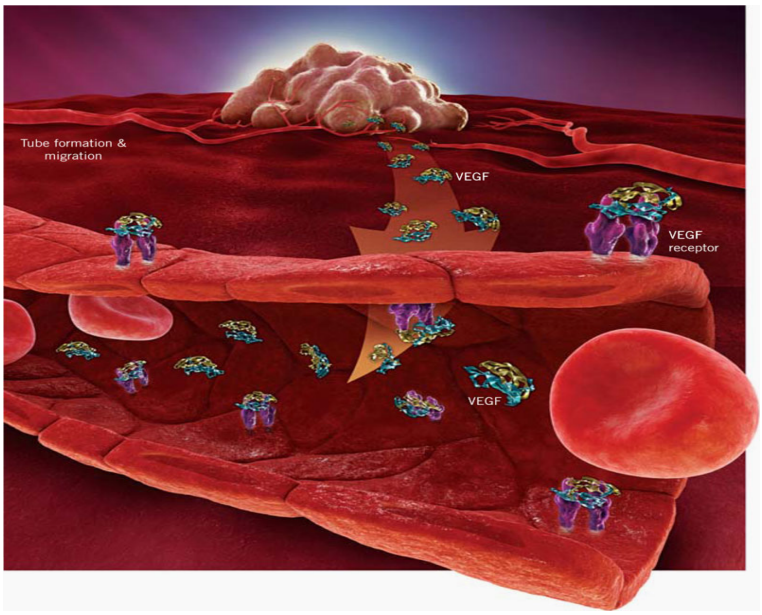


Figure 2.1: The process of angiogenesis (courtesy of Genentech biooncology)

featuring complex branching patterns and irregular vessel diameters. These abnormalities of tumor vasculature make it spatially and temporally heterogenous in nature and structurally and functionally different from normal vessels [52].

One of the immediate consequences of tumor angiogenesis is the invasion of tumor cells into various other organs of the body. This ability of cancer cells to break away from the primary tumor and spread to other locations is termed "metastasis". Two major routes of this metastatic spread are the blood and lymphatic vessels. Clinically, metastases are subdivided into two main categories: those in regional lymph nodes that are spread through the local lymph nodes, and the those seen in more distant regions that have usually spread via blood vessels [119]. In most of the cases, an organ-site specificity is observed in the development of metastases from particular types of primary tumors. For example, prostatic carcinoma usu-

ally metastasizes to bone, whereas melanoma in the skin can metastasize to either liver, brain or bowel [119]. The process of metastasis usually involves several steps including the ability to invade into and out of blood vessels (intravasation and extravasation, respectively) and to settle and grow in the new location. The development of metastatic potential may be considered to be one of the late stages of cancer progression and hence controlling angiogenesis may also help in preventing metastasis of primary tumors [137].

## 2.3 Cancer and its Microenvironment

The microenvironment in which a tumor develops plays a key role in its initiation and somatic evolution. The tumor microenvironment is often recognized as the product of a developing relationship between various cell types such as cancer cells, normal cells, various growth factors and extracellular matrix [133]. The actual composition of this microenvironment is highly variable and is often altered further as the disease progresses. The cooperation and communication between a tumor and its microenvironment are very important in turning a benign tumor into an advanced, life-threatening malignancy. The microenvironment usually provides the necessary signals that turn on various transcription factors, that will help the cancer cells to develop critical abilities such as the ability to move, the capacity to degrade extracellular matrix, the ability to develop its own vascular system, the aptitude to survive and ability to establish itself in another location [87, 137].

As the growing tumor develops its own microenvironment that is favorable to its own existence and progression, the conditions within this tumor microenvironment differ greatly from that of normal tissues. A tumor microenvironment is usually characterized by hypoxia, acidity (low pH), and high interstitial fluid pressure.

All these conditions may even be considered as consequences of structurally and functionally abnormal blood vessels [52]. A detailed discussion of the microenvironmental effects on tumor progression is given below.

### 2.3.1 Hypoxia

Tumor hypoxia is often considered one of the key hallmarks of locally advanced solid tumors, occurring due to the imbalance between oxygen consumption and supply [48]. A few major consequences of a hypoxic microenvironment among many are the production of metastatic phenotypes with increased mutation rates, increased angiogenesis, decreased apoptosis and upregulation of various pathways involved in the metastatic cascade [13]. Hypoxia can occur due to the cumulative effects of many factors such as abnormal tumor vasculature, insufficient blood vessels within the tumor, large intervascular distances and reduced capacity of oxygen transport [133]. Figure 2.2 shows the relationship between hypoxia and blood vessels in a tumor biopsy. It also shows the necrotic area with zero oxygen levels.

Hypoxia can be broadly classified as either diffusion limited (chronic) hypoxia or perfusion limited (acute) hypoxia [120]. In the former case, oxygen is treated as a limiting factor–as the tumor grows, the intervascular distances within the tumor become larger than within normal tissue and consequently, cancer cells at greater distances from the vasculature begin to be deprived of oxygen. Perfusion limited hypoxia, the result of intermittent flow, mainly occurs because of the abnormality of the tumor vascular architecture and transient changes in tumor blood flow [13]. As we discussed in the previous sections, the tumor microenvironment is a complex dynamical system with abnormal vascular networks that vary both spatially and temporally and is characterized by defective endothelium, basement membrane, and

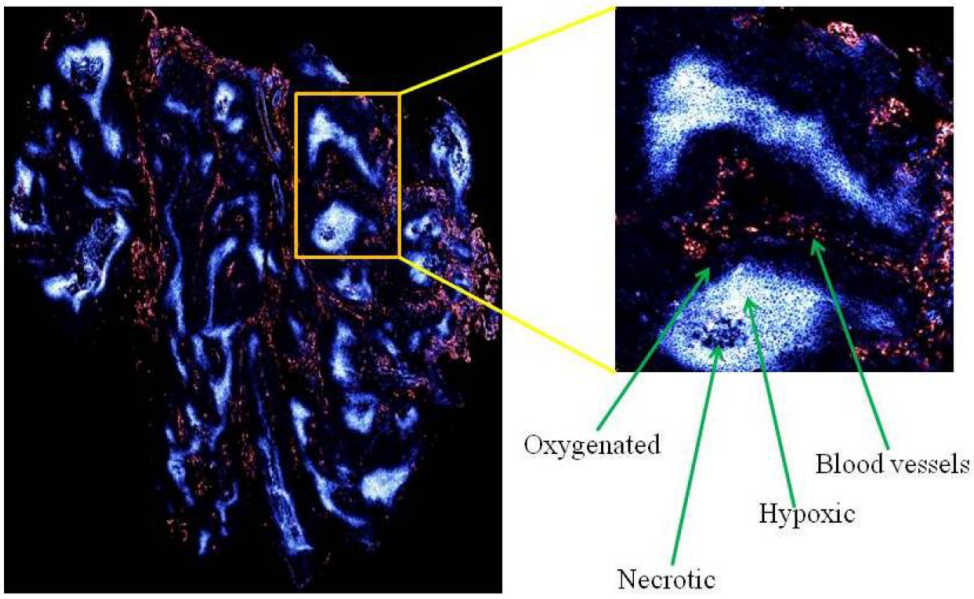


(a) A cervix cancer biopsy stained for hypoxia and blood vessels (Courtesy of Dr. M Milosevic, Princess Margaret Hospital, Toronto, Canada)

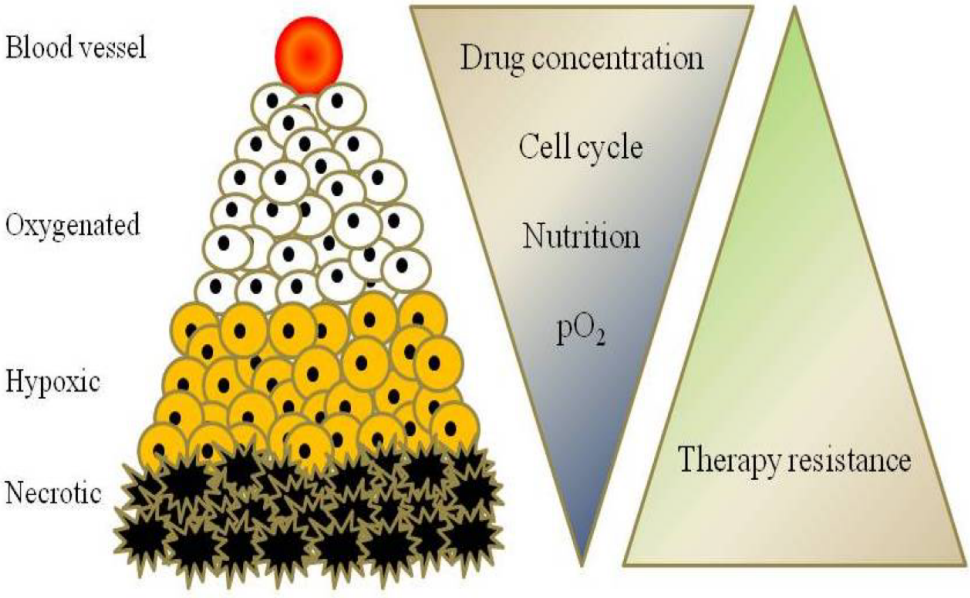


(b) Pictorial representation of various characteristics of hypoxia

Figure 2.2: Tumor Hypoxia

pericyte coverage, as well as interstitial hypertension and acidosis [52]. Due to this irregular nature of the tumor microenvironment, the density of the vascular networks may not perfectly correlate with oxygen distribution – that is, acute and/or chronic hypoxia may be present in tumor tissue regardless of the concentration of blood vessels.

### Estimation of Hypoxia

The role of hypoxia in treatment resistance to radiotherapy is well– documented in the literature and thus it is often considered an important prognostic marker in cancer treatments. The importance of hypoxia in determining radiation response indicates the need for obtaining accurate estimates of clinically relevant hypoxia (see Figure 2.2). Tissue hypoxia is usually measured by direct (invasive) measurements of tumor oxygen tension using needle electrodes or through quantification of intrinsic or extrinsic biomarkers [65]. In preclinical models, diffusion limited hypoxia is usually quantified using the immunohistochemical analysis of biomarkers such as pimonidazole and EF5, whereas perfusion limited hypoxia is estimated using two consecutively-injected perfusion markers, including Hoechst 33342 and DiOC [129]. Some examples of clinically approved extrinsic biomarkers (drugs or chemicals that accumulate after administration under hypoxic conditions) are pimonidazole, EF5 and F-MISO. On the other hand, some genes and proteins involved in hypoxic response such as hypoxia inducable factor 1 (HIF1), carbonic anhydrases - IX (CA-IX) osteopontin and glucose transporter 1 (GLUT1), are used as intrinsic biomarkers to estimate hypoxia [65].

An example of direct estimation methods is the polarographic needle electrode method. Here, tissue oxygen measurements are taken through a protocol usually called the “pilgrim movement”. Here, the needle electrode is initially inserted 1 to

2 mm into the tumor in order to adapt to the tissue environment. Then, the probe is moved through the tissue in 1 mm steps in the forward direction followed by a 0.3 mm step retraction, giving a net step length of 0.7 mm between subsequent measurements. The length of each track is usually determined according to the size of the tumor. Ideally, five to six tracks of 20-30 measurements per tracks are taken to quantify the oxygenation status of the tumor microenvironment [75].

Direct measurement through the needle electrode technique gives a rapid, real-time measurement of tumor oxygen partial pressures [75]; however, its usefulness is limited by the fact that it is a feasible technique only in the case of easily-accessible tumor tissues. It is also found that, due to the invasive nature of the procedure and the uncertainties that result from using linear track measurements to sample a three-dimensional tumor volume, the needle electrode method alone may not always give entirely reliable readings of the tumor oxygen status [75]. Hence, it is advisable to compare the results of two or more estimation methods to study the correlation between their respective hypoxic predictions. These techniques may provide different or potentially complementary information about tumor oxygenation in relation to oxygen levels and the time course of oxygen dynamics. In some experimental studies, hypoxia measurements obtained through examining the biomarkers pimonidazole and EF5 have been compared with needle electrode readings. Conclusions of such studies have been inconsistent, with one showing a correlation between estimates of the hypoxic fraction of cells quantified via biomarker binding and needle $pO_2$ readings while others indicate no significant relationship [57, 95, 56, 82]. These apparently contradictory results may be due to a number of factors, including differences in method-specific definitions of hypoxia, as well as differences in timing of the analysis. A detailed comparison and analysis of various hypoxic estimations are given in Chapter 6.

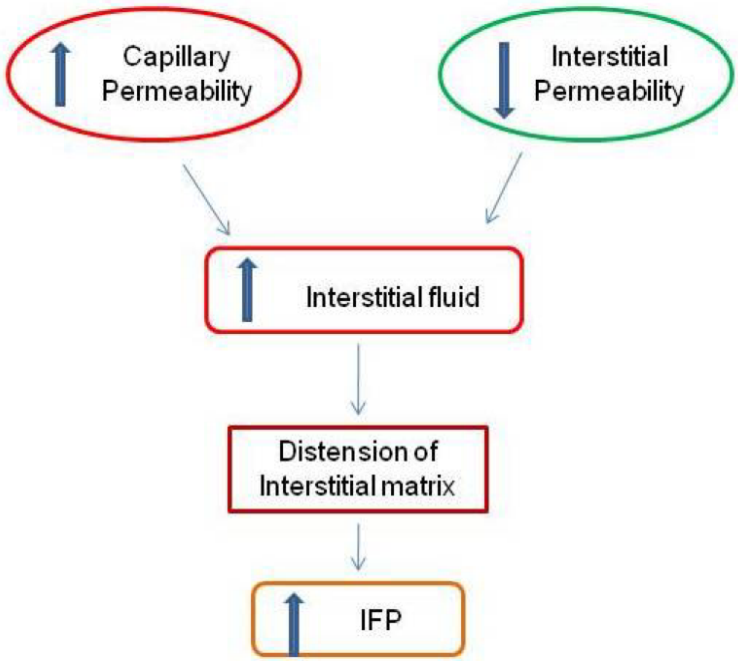


Figure 2.3: Mechanism of elevated IFP in tumor (Courtesy of Dr. M. Milosevic)

### 2.3.2 Interstitial Fluid Pressure (IFP)

In most normal tissues IFP is close to zero whereas most solid tumors show a significantly elevated IFP nearly as high as the microvascular pressure, often ranging from 10 to 100 mm Hg [54]. This tumor IFP is observed to be uniform throughout the centre of the tumor and to drop suddenly at its periphery. As with tumor hypoxia, the main reasons behind high tumor IFP are the abnormal tumor vasculature that arises from unregulated angiogenesis and the lack of a functional lymphatic system within the tumor. The abnormalities of tumor vasculature lead to the leakage of excess fluid that accumulates within the interstitial space and further distends the elastic interstitial matrix, elevating the IFP (Figure 2.3) [75].

Several experimental studies suggest that high IFP is often correlated with a poor prognosis. It has also been considered as a marker of vascular 'normality' [75] and a cause of poor drug delivery within the tumor. One of the reasons for this impaired drug delivery is the decreased transvascular transport (convection or diffusion) caused by relatively high IFP within the tumor, leading to a decreased uptake of drugs or other therapeutic agents into the tumor. Hence, the estimation of tumor IFP is important since it may help in planning various therapeutic strategies such as antiangiogenic therapy and chemotherapy. A theoretical analysis of the various dynamics of tumor IFP is further discussed in Chapter 7.

#### Estimation of IFP

Interstitial fluid pressure is usually measured using the "wick-in-needle" technique, and it represents a simple and rapid method for measurements of interstitial fluid pressure [39]. This technique consists of a hypodermic needle connected to a pressure transducer via a saline filled tube. The needle is filled with wick (nylon fibers) to allow a better contact between the probe and the tissue. The needle is then placed in the tumor tissue where the pressure is to be measured and this pressure is then converted into a voltage by transducer. This method is often used in clinical settings to measure pressure deep in tissues such as the more central parts of the tumor [75].

### 2.3.3 Acidosis and Glycolysis

Like hypoxia and high IFP, acidity also plays an important role in tumor development and invasion. It is yet another direct consequence of the abnormal vasculature, and the effects of acidosis are similar to hypoxia as they promote metastasis, inva-

sion and mutation [43]. Under hypoxic conditions, tumor cells undergo glycolysis (anaerobic respiration) in an effort to survive in these unfavorable conditions and produce lactic acid, decreasing the tumor pH [43]. It has also been observed that some tumor cells rely on glycolysis even in the presence of sufficient oxygen (aerobic glycolysis, or the Warburg effect) in order to produce energy. This may be due to the adaptation of tumor cells to consistently hypoxic and acidic microenvironment by developing cellular traits with constitutive upregulation of glycolysis and resistance to acidic toxicity [43].

## 2.4 Brain Tumors

Primary tumors of the central nervous system represent about 3 % of all cancers. Over 44,500 people in the United States and 10,000 people in Canada are diagnosed with brain tumors every year. The term "brain tumor" generally refers to a collection of primary intracranial tumors, each with its own biology, pathophysiology and prognosis [76]. Primary brain tumors are classified into over 100 different types and the most common are astrocytomas, oligodendrogliomas, meningiomas and mixed oligodendrogliomas [35]. Astrocytomas are further subdivided into diffuse astrocytomas, Anaplastic astrocytomas (AA) and glioblastomas (GBM). These distinctions are made mainly based on pathophysiological similarities between normal glial cells and tumor cells, as well as protein expression similarities observed using immunohistochemistry.

### 2.4.1 Brain Biology

The brain is the principal integrative area of the nervous system and is located in the cranial cavity. It is classified into a number of functional parts, such as the cerebrum, cerebellum and brainstem [76]. The cerebrum is the largest and most developmentally advanced portion of the brain. It is divided into left and right hemispheres, which are further subdivided into frontal, parietal, temporal and occipital lobes which control a number of higher functions including speech, the olfactory senses and intellectual and emotional functions. The brain is mainly composed of two different types of tissues, generally called grey matter and white matter (Figure 2.4). Grey matter consists of neural cell bodies, their dendrites, axon terminals and glial cells. On the other hand, white matter contains mostly long myelinated axons that connect the grey matter areas of the brain to each other and carry sensory information between neurons [76]. The differences between these two types of tissues play an important role in the progression of brain tumors since the invasion capability of tumor cells is highly dependent on surrounding tissue types, as will be discussed in later sections.

#### Blood Brain Barrier (BBB)

The blood brain barrier is both a metabolic and a physical barrier that restricts the entry of potentially harmful chemicals into the brain while allowing the passage of materials that are necessary for metabolic function. This barrier is mainly created by the capillary networks that supply blood to the brain. The blood vessels that maintain this BBB are mostly characterized by tight junctions (TJ), adherens junctions (AJ), transfer proteins and high ionic resistance [138]. In brain tumors, these BBB has usually deteriorated, contributing to the leakage of blood vessels

(a) Axial view of the brain (b) Grey matter (c) White matter

Figure 2.4: Grey and white matter in the brain (Brainweb)

and thus increasing tumor IFP. However, this determined BBB may not necessarily help in the drug delivery within the brain tumor since the increased size of drug molecules reduces the movement across BBB [76].

### 2.4.2 Glioblastoma Multiforme (GBM)

Glioblastoma multiforme is the most common type of primary brain tumor in adults, constituting 50% of all primary brain tumors. GBM can generally be divided into two main subgroups: while primary gliomas most often occur in elderly patients, secondary GBM arises in much younger populations [76]. These gliomas are extremely aggressive and invasive in nature. It has been observed that glioma cells diffuse more quickly in white matter than in grey matter and hence, the invasive nature of gliomas is highly dependent on their locations within the brain. The median survival time for glioma patients is about three months without any treatment. After treatment with surgery, radiotherapy and/or chemotherapy, this life expectancy may be increased up to 12 months [35]. Recently, postoperative radio-

therapy combined with a chemotherapeutic drug called temozolomide was found to be effective in treating GBM [114]. A mathematical model of GBM survival analysis using various postoperative strategies is later given in Chapter 5.

## 2.5 Short Summary

In the present chapter, we have discussed various biological aspects of tumorigenesis and its interactions with the surrounding microenvironment. From the discussion, it can be clearly seen that the tumor microenvironment plays a key role in the evolution of a benign tumor into a malignant tumor and hence it is important to consider its effects in order to develop an accurate mathematical model with predictive capability. We have also seen that the heterogenous nature of the brain tissue may also affect the invasiveness of brain tumors, which will be later used in our mathematical model to investigate brain tumor growth and invasion (see Chapter 4,5).

# Chapter 3

# Introduction to Mathematical Oncology

## 3.1 Introduction

Although the interaction between mathematics and medical sciences has a long history, it is only more recently that it has started to gain more importance and acceptance because of its significant contributions towards many unsolved problems in medicine and biology. Recently, many mathematical models have played important roles in the area of clinical research with their good predictive capabilities with respect to different trial outcomes. These models have the potential to help clinicians to develop successful treatment plans for various diseases. Gatenby and Gawlinski [42] comment, "it is clear from centuries of experience in the physical sciences that the complex dynamics of systems dominated by non-linear phenomena such as carcinogenesis cannot be determined by intuition and verbal reasoning alone. Rather, they must be computed through interdisciplinary, interactive re-

search in which mathematical models, informed by extant data and continuously revised by new information, guide experimental design and interpretation". This realization by medical researchers has attracted the interest of many applied mathematicians and engineers in recent times. The result has been the emergence of the new discipline of Mathematical Medicine, one aspect of which is the study of the dynamics of tumor growth, which can be called "Mathematical Oncology". This is precisely the focus of this Thesis.

In general, a tumor starts with one or more gene mutations which trigger uncontrolled proliferation of cells (by suppressing cellular control mechanisms that normally exist); this can happen at any age and anywhere in the body. In some cases tumors are benign, without any vasculature. Benign tumors are not life-threatening although they can cause some health problems. Other tumors proliferate very fast, invading organs and tissues nearby. They may also recruit their own blood vessels to help them proliferate and migrate. The sheer complexity of these biological systems makes the study of the dynamics of tumor growth a daunting task. However, the experience and success gained by scientists in the use of mathematical models in the physical, chemical and engineering sciences makes it reasonable to expect that similar accomplishments will soon be made in oncology as well.

Mathematical models have the virtue of being much simpler than actual real-life systems. They are akin to a caricature of a person. But just like a caricature stresses and exaggerates a particular characteristic of a person, while still leaving the person recognizable, so a good mathematical model captures the essence of the actual system and neglects all other minor aspects of reality. Once such a model has been built it can be used, with the help of experimental data, to study and simulate the growth of tumors, find possible optimum therapeutic strategies and analyze various other aspects of cancer growth. The modeling strategies can be

broadly classified into two categories: (a) stochastic modeling strategies and (b) deterministic modeling strategies.

As already mentioned, tumor growth and invasion are a complex process mostly governed by different intrinsic and extrinsic factors some of which are random in nature. This inherent randomness involved in the processes of birth, death and mutation events may be modeled as stochastic processes, either through various discrete modeling approaches such as cellular automata or agent based methods, or using stochastic differential equations. One of the earliest stochastic models that describes the process of tumorigenesis is the model by Armitage and Doll, [6] which investigates the age-specific incidence rates of various adult cancers. These models that describe the multistage process of tumorigenesis were further modified by various other researchers to investigate the differences between hereditary and spontaneous cancers [58, 69], to study the effects of apoptosis [126] and to analyze the effects of various mutation rates on tumorigenesis [127]. Recently, in a series of stochastic models Nowak *et al.* [91] discussed the contribution of genetic mutations to the DNA in the process of multistage carcinogenesis and how the architecture of renewing epithelial tissues could affect the accumulation of these mutations [41]. On the other hand, there are several other models that have been developed to study the intrinsic heterogeneity of interacting population and its influences on the fluctuating microenvironment. Some of these include the models by Jansson and Revesz [55], Michelson *et al.* [74] and Chen *et al.* [25]. Stochastic modeling approaches have also been used in the literature to study the effects of various therapeutic strategies and in particular radiation therapy [118, 102, 130]. In recent work, Sachs *et al.* [102] introduced a stochastic model to investigate the role of radiotherapy in the development of secondary cancers. Other recent examples of stochastic models can be seen in the works of Komarova *et al.* [141].

On the other hand, from even a cursory look at the literature, it can be seen that the mathematical modeling of tumor growth has mainly focused on deterministic approaches. Deterministic models can also be classified into many categories such as ordinary differential equation (ODE) models or temporal models, partial differential equation (PDE) models or spatio-temporal, etc. Mathematical analysis of solid tumor growth using deterministic models started in the early 1950's. Aruaujo *et al.* [5] give a good review of the history and contribution of various mathematical models by explaining different modeling strategies used in the literature.

Ordinary differential equations have been used to model tumor growth for many years. Generally, it is simpler and easy to handle and at the same time, it can provide early, useful results particularly when the spatial dependence plays a less significant role. ODE models can be used to analyze various characteristics of tumor growth, including growth dynamics [98, 86, 83, 62], various treatment strategies [84, 85, 49, 101] as well as the role of different cell signalling pathways in cancer initiation and growth [110, 97]. ODE models are also commonly used in studying the pharmacokinetics and pharmacodynamics of various anti-cancer drugs and their effects in cancer growth. Examples include the models by Panetta *et al.* [90] and Chuang [26]. Recently, Sachs *et al.* [101] used a simple ODE model to investigate the essential interactions between the tumor and angiogenesis during cancer growth or therapy. Although these simple modeling approaches capture the essence of complicated interactions, the spatial aspects of cancer that are of critical importance often necessitate the use of PDEs or spatiotemporal models.

There are a variety of PDE models in the literature that aim at modeling various aspects of tumorigenesis and most of them use the concept of reaction-diffusion processes to achieve this. Early works include the modeling of avascular tumor as homogenous/heterogenous populations that grow under the influence of various nu-

trients such as oxygen [17, 45, 73, 2]. These models are further modified to include various cell-cell interactions [19] as well as the interactions of the tumor with its microenvironment such as tumor angiogenesis [21, 23, 4, 60], hypoxia [104, 125] and interstitial fluid pressure [53]. In this thesis, we focus on the deterministic, or continuum approach to modeling brain tumor growth and associated therapies using a spatio-temporal mathematical model and hence we refer readers to subsequent chapters for further discussions of various PDE based models. Here, we also study the effects of various factors associated with the tumor microenvironment on the growth and control of brain tumors. In the following sections, we will see various mathematical models that have been used in the literature to study different aspects of tumor growth, including tumor microenvironment effects and therapeutical strategies.

## 3.2 Growth Dynamics

Over the past few decades, the most common approach to describing tumor growth has been the use of a simple temporal model, which can be written as

$$\frac{dN}{dt} = f(N) \quad \text{with} \quad N(0) = N_0, \tag{3.1}$$

where $N$ is the total number of tumor cells and $f(N)$ describes the tumor cell growth dynamics.

The simplest approach to modeling the experimental data is using exponential growth dynamics, where the cell doubling time remains the same through out the growth period. For exponential growth, the function $f(N)$ can be written as

$$f(N) = \rho\, N, \tag{3.2}$$

where $\rho$ is the net proliferation rate. However, the exponential growth model results in the unlimited growth of the cancer cells and can only be applied for short time scales. To ensure that the growth rate of the population decays as the cell density approaches maximum capacity, one can either choose a logistic growth or Gompertzian model [86, 83, 62, 98], which are given by

$$f(N) = \begin{cases} -\rho\ N \ln\left(\frac{N}{N_\infty}\right): & \text{Gompertzian model} \\ \rho\ N\left(1 - \frac{N}{N_\infty}\right): & \text{Logistic model} \end{cases} \tag{3.3}$$

Here, $N_\infty$ denote the carrying capacity which the cancer growth asymptotically approaches as its growth rate decreases over time.

A general form of growth pattern incorporating all the above growth laws can be written as [60],

$$f(N) = \alpha_1 N - \alpha_2 (N)^{\gamma+1}, \tag{3.4}$$

with $\alpha_1$ and $\alpha_2$ being two different parameters. When $\alpha_2 = 0$, this general form reduces to the above discussed exponential growth dynamics and when we set $\alpha_1 = \rho/\gamma$ and $\beta_2 = \rho/(\gamma N_\infty^\gamma)$ $(\gamma > 0)$, we will obtain a generalized logistic growth function,

$$f(N) = \left(\frac{\rho N}{\gamma}\right)\left[1 - \left(\frac{N}{N_\infty}\right)^\gamma\right]. \tag{3.5}$$

This generalized logistic growth model can be used to derive the above discussed simple logistic and Gompertzian models by choosing $\gamma = 1$ and $\gamma << 1$, respectively.

Although there have been several attempts to formulate a universal growth law for cancer growth [98, 140], it is rather difficult to prove the existence of a unique growth law even for humans cancers [46]. For the purpose of this thesis, a logistic growth dynamics is used to model tumor growth since it enforces a bounded growth

pattern. However, in the time frame of interest, i.e. before the tumor becomes fatal (the period when treatments are applied), exponential growth dynamics may also be acceptable for modeling purposes.

## 3.3 Modeling Angiogenesis

Mathematical modeling of angiogenesis has become an active research field in recent years, especially in the context of tumor growth and invasion. One of the early works on the modeling of tumor-induced angiogenesis is by Balding and McElwain [7], who studied the growth of capillary networks in terms of capillary tip densities and capillary sprout densities in response to tumor angiogenic factors. Since then, there have been many models considering the response of endothelial cells to various angiogenesis promoting factors secreted by cancer cells of solid tumors. Examples include models by Chaplain *et al.* [22, 20, 24], Byrne *et al.* [18], Levine *et al.*[64] and Kohandel *et al.* [59]. Most of these models use a continuum modeling approach where quantities such as tumor cell density, endothelial cell density and densities of various angiogenic growth factors are dealt with a macroscopic scale through a system of nonlinear PDEs. Later in Chapter 7, we will see a coarse grain modeling approach for incorporating vasculature and its role in elevating tumor interstitial fluid pressure (IFP).

The inability of macroscopic models to capture microscopic features of the angiogenic processes, as well as various other morphological properties of emerging capillary networks, encouraged the formulation of discrete models of angiogenesis. These often consider formation of individual capillary vessels, modeled at the level of individual cells and thus provide more insights into the details of capillary formation [112, 131, 8]. Recently, Anderson and Chaplain [4] introduced a hybrid model

for tumor angiogenesis through the discretization of a continuous model using the concept of probabilistic branching. A good review of various mathematical modeling approaches to angiogenesis and capillary formation can be found in the review paper of Mantzaris *et al.* [68].

## 3.4 Modeling Tumor Hypoxia

The importance of tumor hypoxia in determining patient response to various therapeutic strategies, especially towards radiation therapy, indicates the necessity for its accurate quantification. As explained in the previous chapter, tissue hypoxia is usually measured either with the help of hypoxic markers (where a biopsy is needed) or using needle electrode techniques. One of the main disadvantages of both of these assays is that these measurement techniques are invasive and the tumor must be accessible in order to get satisfactory measurements of the oxygenation status. Some other less-invasive techniques such as MRI or PET scans exist, however the resolution currently available is so poor that it may not be possible to obtain detailed quantification of tumor hypoxia.

On the other hand, one can use theoretical simulations based on available parameters to obtain, non-invasively, quantitative as well as qualitative predictions about the tumor oxygenation status. Mathematical modeling of oxygen transport generally depends on the distribution of vasculature within the tumor. Consequently, to model tumor hypoxia, one can either use a reaction diffusion equation that accounts for the production, consumption and diffusion of oxygen within the tumor tissue, or various other discrete models which analyze the oxygen transport at cellular levels.

Among many, one of the most important factors affecting the temporal and spa-

tial distribution of tumor hypoxia is the network of tumor vasculature. Theoretical investigations have shown that microvascular heterogeneity can substantially affect the distribution of hypoxia [104]. Early theoretical studies [123, 51, 119] that describe the tissue oxygenation process did not consider the effects of irregular tumor vasculature. Dasu *et al.* [33] introduced a coarse grained model for vascular networks in developing a theoretical model of tumor oxygenation; the authors analyzed different oxygenation dynamics based on a log-normal distribution of intervascular distances and studied their relationships to chronic and acute hypoxic conditions with the help of a diffusion model. Based on experimentally derived data and numerical simulations, Dewhirst *et al.* [38] showed that $O_2$ consumption is the most important factor influencing the local $pO_2$ distribution within the tumor. Kohandel *et al.* [59] developed a mathematical model that incorporates tumor cells and the vascular network, as well as oxygen concentration, and used it to study the optimal combination of anti-angiogenic and radiotherapy treatments. To obtain the vasculature, and subsequently the oxygen distribution, a random initial condition for the blood vessels was used. However, it may be of greater clinical relevance if patient-specific microvascular distributions, which can be obtained through novel non-invasive imaging techniques, are incorporated in a model for tumor hypoxia- the details of such a procedure will be discussed in Chapter 6.

## 3.5 Interstitial Fluid Pressure (IFP)

Most solid tumors show an increased interstitial fluid pressure which acts as a barrier to the intercapillary transport of therapeutic drugs, affecting the treatment response of cancer patients. Consequently, lowering high IFP within a tumor through the application of various novel anti-cancer therapies might be a useful

approach to improve drug delivery within the tumor. As previously explained, the interstitial fluid pressure can be measured using invasive techniques such as the wick-in-needle technique [39]. However, as in the case of hypoxia estimation, one of the main disadvantages is that the tumor must be in an accessible location. Recently, there have been several attempts to estimate tumor IFP using a mathematical model that is supplemented by various parameter values obtained through current imaging techniques (M. Milosevic, personal communication).

Most of the mathematical models in the literature that describe tumor IFP are largely based on Baxter and Jain's pressure model [9] given (under steady state conditions) by:

$$\nabla^2 P = -\frac{\alpha^2}{R^2}(P - P_e), \tag{3.6}$$

where

$$P_e = P_v - \sigma(\pi_v - \pi_i) \quad \text{and} \quad \alpha = R\sqrt{\frac{L_p S}{KV}}.$$

Here, $L_p$ is the hydraulic conductivity of the microvascular wall, K is the hydraulic conductivity of interstitium, $\frac{S}{V}$ is the surface area of vessel wall per volume of tumor, $P_v$ is vascular pressure, $\sigma$ is the average osmotic reflection coefficient for plasma proteins, $\pi_v$ is osmotic pressure for plasma and $\pi_i$ is osmotic pressure for interstitial fluid. One can easily derive the above equation for IFP by considering the tumor to be a porous medium and applying Darcy's and Starling's Laws for fluid transport within this porous medium [9] (derivation and further details will be discussed in Chapter 7). This model has been used widely in the literature, especially to study the effect of abnormal tumor vasculature and to analyze the results of various therapeutic strategies (including anti-angiogenic therapy) on the tumor IFP [54]. However, in its present form this model ignores the changes within

the tumor microenvironment (unless its parameters are changed manually). In Chapter 7, we will see a modified version of this pressure model which considers the dynamical changes in vascular networks due to the balance/imbalance in pro- and anti-angiogenic growth factors.

## 3.6 Treatment Strategies

In most cases of cancer, patients receive standard medical therapies as soon as possible after the initial diagnosis. The choice of cancer treatment is often influenced by several factors, including the type, grade and location of the cancer and the patient's overall condition. The most common treatment modalities are surgery, chemotherapy, gene therapy and radiotherapy. Generally, more than one of these treatments are used to achieve an effective survival rate. In the case of brain tumors, surgery followed by radiotherapy and/or chemotherapy is often used, as will be discussed in Chapter 5.

### 3.6.1 Surgery

Surgery is the oldest form of effective cancer therapy in treating benign and malignant tumors. It may be used alone or in combination with other modalities. The goal of surgery is to remove all of the visible tumor cells present in a given location, thereby increasing the survival time of the patient. The expected success rate of surgery depends on many factors, including size and location of the tumor, specific tumor type, and type and extent of the surgical procedure. Surgery is generally considered a primary treatment modality, especially in the case of solid tumors such as brain tumors.

Mathematically, the instantaneous effect of surgery can be incorporated into the model (Equation 3.1) by assuming that it kills a fixed fraction ($\exp(-k_s)$) of the tumor cells [60]. Here $k_s$ is the fraction of the removed tumor cells and its value reflects the resection area. For instance smaller values of $k_s$ denote that the resectional area is limited either due to a lack of accessibility or undetected tumor cells. The surgery can be included in the simple temporal model as follows [60]:

$$\frac{dN}{dt} = f(N) - k_s I(t = t_{\text{surgery}}), \tag{3.7}$$

where $I(t = t_{\text{surgery}})$ is the indicator function which takes the value one if $t = t_{\text{surgery}}$ and zero otherwise.

### 3.6.2 Chemotherapy

Chemotherapy plays an important role in most of the mutimodality treatment protocols that are used to treat many tumor types. There are several chemotherapeutic agents that target the tumor cells in various ways, and these include alkylating agents like Carmustine and Cisplatin, anti-metabolic inhibitors like Cytosine and Arabinoside and mitotic inhibitors like taxoids and Teniposide. Most of these chemotherapeutic drugs destroy cancer cells by targeting their DNA and preventing the cells from growing and dividing rapidly; unfortunately, these drugs may also affect normal cells. Standard combination chemotherapy consists of drugs that contain platinum agents such as cisplatin and carboplatin, and taxane compounds such as paclitaxel and cyclophosphamide. For decades, investigators have examined the role of chemotherapy in the treatment of brain tumors; however, numerous clinical trials of various chemotherapeutic agents administered in a variety of ways have shown very different outcomes (see [66], for a review on major clinical trials

and their conclusions). The choice of chemotherapies, dosage, and timing are determined by many factors including patient response and the stage of the glioma. Chemotherapy can be included into the mathematical model using several cell kill hypotheses as discussed in the following section.

### 3.6.3 Modeling Chemotherapy

There have been several mathematical models that study the effects of chemotherapy on tumor growth (see [60] and the references therein); however only a few investigations have been carried out related to brain tumors. Cruywagen *et al.* [31] and Tracqui *et al.* [128] studied the effects of chemotherapy on glioma growth assuming a reaction-diffusion model for growth and invasion and a log-kill hypothesis for cell death due to chemotherapy. Since the single cell model was unsuccessful in fitting the experimental data, they extended the model to a two-cell population model. Swanson *et al.* [117] generalized the model to reconsider the effects of chemotherapy in the case of heterogeneous brain tissue. Since there are a number of factors (such as the pharmacokinetic and pharmacodynamics of the drugs, patient response and the grade of glioma) that affect the chemotherapeutic induced cell death, it may be wise to choose a cell-kill model that accurately describes the effect of a particular drug.

In the log-kill model, cell kill is assumed to be proportional to the tumor population which means that a given dose of chemotherapeutic drug kills a fixed fraction of surviving tumor cells. Another hypothesis, known as the Norton Simon (NS) model, [84, 85] considers that the cell kill is proportional to the growth rate of the tumor. A third hypothesis called the $E_{max}$ model assumes that the cell kill is proportional to a saturable function of the mass. This means certain chemotherapeutic drugs

need to be metabolized by enzymes before being activated and since the amount of these enzymes are fixed, they are assumed to follow Michaelis-Menton kinetics [49]. These effects of chemotherapeutic drug induced cell death can be included into the mathematical model (Equation 3.1) by defining a cell kill term $G(N,t)$ and thus, the model can be written as

$$\frac{dN}{dt} = f(N) - G(N,t), \tag{3.8}$$

with

$$G(N,t) = \begin{cases} k_{c1}(t)N : & \log - \text{kill} \\ k_{c2}(t)N/(N+\delta) : & \text{E}_{max} \\ k_{c3}(t)f(N) : & \text{NSmodel.} \end{cases} \tag{3.9}$$

The function $k_{ci}$ gives the temporal drug profile and it is proportional to the drug concentration, $k_{ci} = 0$ denotes the absence of drug effect and $k_{ci} > 0$ gives the amount or strength of the available drug.

### 3.6.4 Radiotherapy

Radiotherapy is one of the main treatment strategies that is used to treat most common tumor types. It can be either used as a primary therapy or in combination with other therapeutic protocols. Radiotherapy is usually carried out using a linear accelerator (LINAC) that produces high energy X-ray radiation. This radiation deposits increasing doses with depth up to a few centimeters, and is absorbed by tissues in an exponential manner. The radiation dosage is delivered in a combination of several beams at various angles, so that it overlaps inside the tumor volume (or gross tumor volume, GTV) with a maximum dose, sparing the normal tissues. This GTV is determined through different diagnostic and planning protocols mainly using various imaging techniques like magnetic resonance imaging

(MRI) or computed tomography (CT). After irradiation, cells are killed mainly due to damage to DNA, leading to reproductive apoptosis. When high energy X-rays are absorbed within target tissue, many fast high-energy electrons are produced and some of these electrons interact directly with the DNA. This direct interaction may be of either ionizing (Compton effect) or exciting (photoelectric) type, eventually damaging the DNA double strand ('double strand breaks' or DSB). On the other hand, some of these electrons interact with other molecules in the tissue (for example, water) producing hydroxyl radicals which in turn damage DNA, causing an indirect effect. These radicals have a very short life time (several milliseconds) and hence they cannot migrate distances longer than tens of angstroms along the DNA. The indirect radiation damage caused by these free radicals can be increased in the presence of oxygen or other radiosensitizers. This is because the oxygen reacts with the free radical making it more stable and thus fixing the radiation lesion ("oxygen fixation hypothesis"). This is one of the reasons why hypoxic cells are more radioresistant.

Several other biological processes such as repair of cellular damage, reoxygenation of the tissue, redistribution within the cell cycle and repopulation of cells ("the 4 R's of radiation biology" [47]) also affect the number of surviving tumor cells after the radiation. Hence the effect of the irradiation strongly depends on the time course and the various methods of delivery. However, it is also important to reduce normal tissue damage due to the radiation, although normal cells have better repair mechanisms and their division rates are much slower than tumor cells. This makes it necessary to use various fractionation protocols for delivering a biologically effective dose over treatment period of longer duration. Fractionation spares normal tissues because of repair and cellular repopulation and increases tumor damage because of reoxygenation and redistribution. In the following sections, we will discuss various

fractionation schemes, and different methods through which they are delivered to the tumor volume.

### External Beam Radiation Therapy

External beam radiation therapy (EBRT) is one of the most common and conventional ways of delivering the radiation dosage. In EBRT, an external source of radiation (high energy X-ray beams, cobalt irradiation or particle beams such as protons and ions) is used to direct the radiation beams from outside the body to the organ of interest. These beams are usually given in a 360 degree fashion so that they are directed at the target for the entire treatment time but pass through other parts of the brain only momentarily, thus making it possible to deliver a maximum dose to the area of interest while sparing the normal tissues from the risk of high radiation exposure. Figure 3.1(a) shows a schematic representation of EBRT. There are mainly two types of EBRT available: 3D conformal radiation therapy and intensity modulated radiotherapy; their details are given below.

### 3D Conformal Radiation Therapy

In conformal radiotherapy, the radiotherapy machine shapes the radiation beams to fit the size and shape of the tumor area with the help of advanced imaging techniques (Figure 3.1(b)). Usually, radiation-impermeable metal blocks are used to change the shape of the beam so that the irradiated area looks similar to the shape of the tumor. This results in a better radiation induced cell death by delivering a higher dose of radiation straight to the tumor area; hence, less healthy tissue is included in the radiotherapy field resulting in fewer long term side effects.

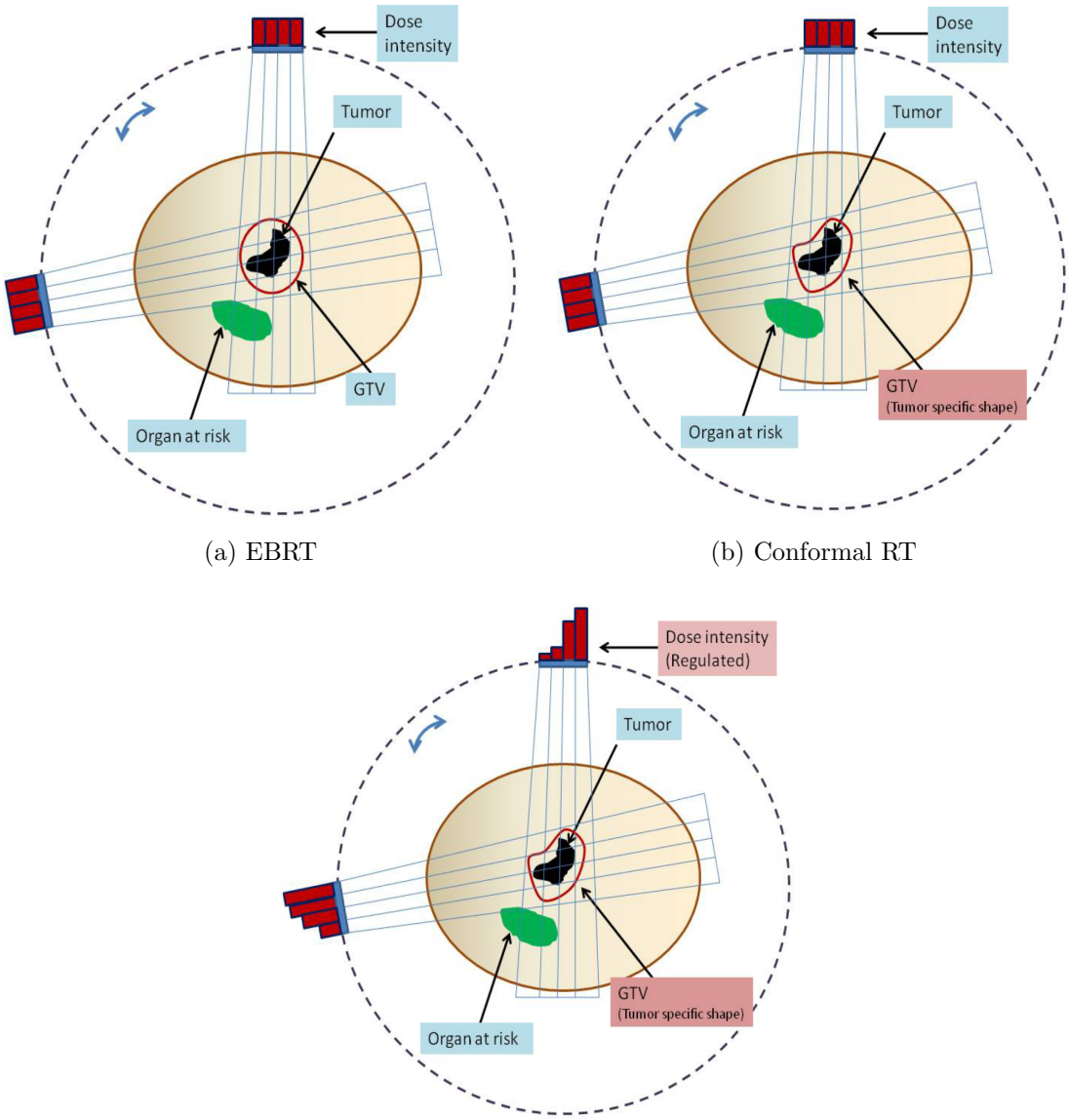


(a) EBRT

(b) Conformal RT

(c) IMRT

Figure 3.1: Schematic representation of various radiation delivery methods

### Intensity Modulated Radiation Therapy (IMRT)

Intensity modulated radiation therapy or IMRT, is an advanced radiation delivery method that utilizes computer-controlled x-ray accelerators to deliver precise radiation doses to a malignant tumor or specific areas within the tumor. It works in a similar fashion to that of conformal radiotherapy by delivering the radiation dose more precisely to the three-dimensional (3-D) shape of the tumor by modulating/controlling the intensity of the radiation beam. In addition to the precise shape of delivery, IMRT also allows one to change the intensity of the radiation focusing within the tumor while minimizing the dose to surrounding normal critical structures (Figure 3.1(c)). Typically, combinations of several intensity-modulated fields coming from different beam directions produce a custom tailored radiation dose that maximizes tumor dose.

### Stereotactic Radiosurgery/Radiation Therapy

Stereotactic radiosurgery is a highly accurate form of radiotherapy with a precise delivery of a single, high dose of radiation to a small intracranial target while minimizing the absorbed dose in the surrounding tissue. It is sometimes considered as an alternative to invasive surgery, especially when a tumor is inaccessible due to its location or other complications. Although stereotactic radiosurgery is often completed in a single day, sometimes it is given in a fractionated dose (often termed a "stereotactic radiotherapy").

### Brachytherapy

The surgical implantation of radioactive isotopes into a tumor is known as brachytherapy. It is mostly used in the case of solid tumors such as brain tumors since the

implanted isotope can deliver high doses of radiation to a well-defined area causing minimal damage to the surrounding normal tissue. Brachytherapy is divided into two main categories: interstitial brachytherapy and intracavity brachytherapy. In interstitial brachytherapy, either low dose rate or high dose rate radioactive sources are placed in catheters spaced evenly within the tumor or in the center of the tumor. On the other hand, intracavity brachytherapy involves placing radioactive isotopes into a body cavity close to a tumor. While brachytherapy gives an advantage over hypoxic tumors due to its continuous effect, it can be useful only when the target tumor is accessible invasively. A number of novel radioactive isotopes such as Iodine-125 and Iridium-192 are being considered for brachytherapy. Most of these isotopes emit low-energy photons, which reduce the risk of radiation damage to normal tissues [47].

### 3.6.5 Fractionation and Dosage

The ideal goal of radiotherapy is to maximize the radiation induced damage of tumor cells while minimizing the injury to normal cells and this is mainly achieved through the use of fractionation of the total dose. In simple terms, fractionation means breaking down the total radiotherapy dose into small doses which are given according to an appropriate schedule for a certain duration.

Tumor cells are often termed "early responding" since they have a low repair rate and accelerated repopulation which makes them very sensitive to damage causing reproductive cell death. Normal cells, on the other hand, are termed "late responding" since their repair time is broader than their tumor counterparts. It has also been observed that cells are more sensitive to radiation while they are in the $G_2$ or M phases of their cell cycle as compared to other phases. The percentage of the

population at each of these phases is often determined by their cell growth kinetics (tumor cells have a faster growth rate). Following radiation, these percentages are redistributed within 1-2 cell cycles, thus improving the chances of radiation-induced cell death in the next fractionation. Another important factor that determines the extent of radiation damage is the oxygenation status of the tumor tissue, due to the so called "oxygen fixation hypothesis". While normal tissues are well oxygenated due to well-distributed normal healthy vasculature, their tumor counterparts are often hypoxic (except near vessels) due to the presence of abnormal vasculature and rapid proliferation (as discussed in previous sections). Radiation exposure usually kills the oxygenated tumor cells while sparing most of the hypoxic cells. However, if sufficient time is allowed before the next radiation dose, the process of reoxygenation will restore some proportion of hypoxic cells to a state of sensitivity to subsequent radiation fractions.

In the fractional delivery of radiotherapy, fraction size and total dosage also play key roles in sparing the normal tissue while increasing damage to the tumor. While fraction size is a dominant factor affecting late-responding tissues like normal tissue, the overall treatment duration has less effect. On the other hand, early-responding tissues like tumor cells are more sensitive towards both fraction size and total treatment time. Various common fractionation schemes used in clinical practice are listed below.

### Conventional Fractionation

Conventional radiotherapy is usually delivered with a fraction size of 1.8 to 2 Gy (1 Gy = 1 Joule/kg = 1 $m^2s^{-2}$) daily 5 days a week up to a total dose of 60 Gy to 70 Gy.

#### Hyperfractionation

Hyperfractionation is often used to further reduce the late effects (damage to normal tissue) while slightly increasing the radiation damage to early responding tumor tissue and thus achieving a better tumor control. In hyperfractionation, the overall treatment time remains the same as conventional but instead of one fraction, two or more fractions are given per day. The increase in the number of fraction and the decrease in the dose per fraction allow the delivery of higher total dosage of radiation to the tumor tissue. Generally a fractional dose of 1 to 1.2 Gy twice a day, 5 days a week and up to a total dose of 65 to 80 Gy is used in most of the clinical trials.

#### Accelerated Fractionation

Accelerated fractionation is used to reduce overall treatment time in order to reduce the repopulation in rapidly-proliferating tumors. It involves approximately the same fraction size and total dosage as that of conventional fractionation but is given twice a day to reduce the total treatment time. The usual delivery protocol for accelerated fractionation is 1.5 to 2 Gy twice a day, 5 days a week and up to a total dose of 50 to 70 Gy.

### 3.6.6 Modeling Radiation Therapy

There are numerous mathematical models describing the effects of radiotherapy on tumor cells [122]. As we discussed in the previous sections, the main radiation damage to cells is assumed to be through DNA double strand breaks. Most damage of this nature is repaired, but some DSBs are incorrectly repaired leading to mitotic

cell death [67]. The most commonly used model for studying the survival response to radiotherapy is the linear quadratic (LQ) model [122, 40, 106, 101, 103]. The LQ model considers the effects of both irreparable damage and repairable damage susceptible to misrepair. Several studies have extended the model to include other effects such as cellular proliferation, cell cycle redistribution and reoxygenation during fractionated radiotherapy [12, 88, 136]. The LQ model and its extension, the incomplete repair (IR) model are common tools for studying fractionation and dose-rate effects in radiotherapy [121, 80].

One of the basic assumptions of the LQ model is that the cell is damaged through double strand breaks of its DNA, leading to reproductive cell death. This damage to DNA can happen in two different ways, which are captured in the LQ model through its linear and quadratic terms (Figure 3.2). The linear term accounts for the DSBs due to one single hit of radiation whereas the quadratic term represents the effects of two separate ionizing events that eventually cause DNA DSBs [47]. Assuming that the probability of one interaction causing a DSB is linearly proportional to the dose $D$, the survival fraction in the LQ model can be written as

$$S = N = \exp\left(-\alpha D - \beta D^2\right), \tag{3.10}$$

where $\alpha$ and $\beta$ are radiation sensitivity parameters.

This simple LQ model can be further generalized to include the effects of fractionation protocols as well as the late and early effects (through the choice of various $\alpha/\beta$). Considering the generalized version of the LQ model; given by,

$$\frac{1}{N(t)}\frac{dN(t)}{dt} = -\alpha d(t) - 2\beta d(t)\int_0^t d(t')e^{-\mu(t-t')}dt', \tag{3.11}$$

the survival fraction $S(T)$ at time $T$ can be rewritten as,

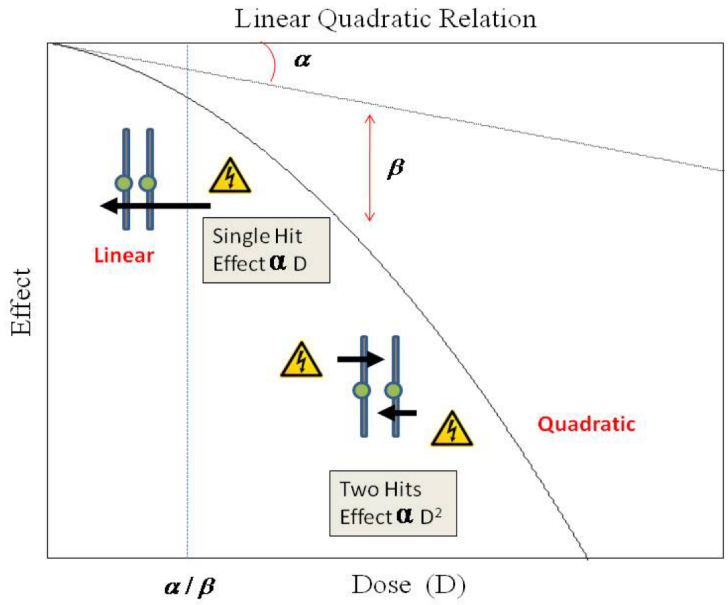


Figure 3.2: Linear quadratic model: Relationship between chromosome aberrations and cell survival

$$S(T) = \exp\left[-\alpha \int_0^T d(t)dt - 2\beta \int_0^T d(t)\left(\int_0^t d(t')e^{-\mu(t-t')}dt'\right)dt\right]. \qquad (3.12)$$

Here, $d(t)$ is the dose fraction at time $t$, $N(t)$ is the total number of tumor cells at time $t$ and $\mu$ is the repair half rate. Other simplifications of this generalized model are the incomplete repair model of continuous fractionation and incomplete repair mode for acute fractionation. A detailed analysis of this model under various fractionation schedules is given in Chapter 5.

### 3.6.7 Antiangiogenic therapy

It is a well known fact that a solid tumor cannot grow more than a few millimeters unless it forms new vascular networks, through the process of angiogenesis. These vessels, formed as a result of the tumor's response to its own need for oxygen and other nutrients, are structurally and functionally abnormal [52]. Hence, tumor vessels which are abnormal, leaky, tortuous and less perfused often result in poor delivery of both oxygen as well as therapeutic drugs to the tumor. The rationale behind the use of a novel anti-cancer therapeutic strategy called anti-angiogenic therapy is that it should destroy tumor vasculature, thereby depriving tumors of oxygen and nutrients. It was recently hypothesized by Jain [52] that judicious application of these anti-angiogenic drugs can also transiently "normalize" the abnormal structure and function of tumor vasculature, resulting in a more efficient pathway for delivery of drugs and oxygen to the targeted tumor cells.

Recently there has been major advances in the development of antiangiogenic therapeutic strategies due to the identification of several molecular mediators and inhibitors of angiogenesis. Many anti-angiogenic drugs are now undergoing various stages of clinical trials and these include endothelial cell inhibitors like TNP-470, Thalidomide and Endostatin, and angiogenic factor inhibitors like SU5416, Sorafinib and Imatinib. Although these antiangiogenic treatments have the potential to complement conventional treatments, several clinical and pre-clinical trials have suggested that currently available anti-angiogenic strategies are unlikely to produce significant results unless they are combined with conventional therapies. Alternatively, effects of these combination therapies are often determined by various factors such as fractional dosage of the maximum tolerated dose, schedules and sequencing of various modalities. One of the most cost-effective ways through which optimal

treatment might be achieved is through a carefully devised, patient-specific mathematical model that is supplemented with clinically-relevant parameters.

There have been several mathematical models of tumor angiogenesis, mainly focusing on capillary formation in response to several molecular signals [22, 20, 24, 18, 64, 44]. But much more recently, researchers have started to look into blood-flow modeling in a tumor-induced micro-capillary network in order to study the application of anti-angiogenic and chemotherapeutic effects within the tumor [72, 111]. Kohandel *et al.* [59] considered a continuum- based approach to generate vasculature and to study optimal treatment strategies for cytotoxic and anti-angiogenic treatments. Although these mathematical models might be useful in studying the qualitative effects of anti-angiogenic drug therapy, it may be useful to develop more quantitative models by incorporating the pharmacokinetic and pharmacodynamic details of the specific drug into the model. It may also be helpful to compare various drug delivery mechanisms such as liposome delivery and nano-particle delivery in seeking to optimize the treatment effects of combination modalities.

## 3.7 Short Summary

Mathematical modeling of tumorigenesis, including the tumor microenvironment, is a fast- growing area of research. This chapter reviews common mathematical approaches used to model various aspects of cancer growth including growth dynamics, microenvironmental factors such as hypoxia and interstitial fluid pressure, angiogenesis and different treatment modalities. Following chapters will illustrate each of these characteristics of tumorigenesis in detail.

# Chapter 4

# Glioma Growth and Invasion: Mathematical Model

## 4.1 Introduction

Mathematical models usually serve as a tool for the prediction and development of experimental or clinical strategies, wherein it helps to understand the important parameters that can guide accurate analysis. For the past several years mathematical models have been used to understand glioma growth and invasion from a theoretical point-of-view [77, 117, 28]. In the following sections, we discuss the framework of different models used to study glioma growth and invasion.

## 4.2 Spatially-Homogenous Models

Gliomas, the most common primary brain tumors, are highly diffusive and invasive [35, 63, 11, 10, 66, 36]. Simple temporal mathematical models of tumor growth

involve only the total number of tumor cells subject to either exponential or Gompertzian growth laws [62, 86, 83]. However, gliomas consist of motile cells that can migrate as well as proliferate, and thus spatial aspects seem to be crucial in their theoretical modeling. Recent mathematical models formulated the problem of brain tumor growth as a reaction-diffusion process (for a review see [77]), in which the rate of change of tumor cells is given in terms of the net proliferation and diffusion of tumor cells. The proliferation component usually corresponds to the active part of the tumor and is mainly represented using one of the suitable growth laws while the diffusion component is generally associated with external factors associated with the tumor and is represented using a diffusion law. Cruywagen et al. [31], and later Cook et al. [30], Woodward et al. [144], and Burgess et al. [16], considered a simple reaction-diffusion equation to study diffusive tumors and the effects of surgical resection and chemotherapy. If $c(x,t)$ denotes the cell density at position $x$ and time $t$, then the model can be expressed in mathematical form as

$$\underbrace{\frac{\partial c(x,t)}{\partial t}}_{\text{Rate of change of tumor cell density}} = \underbrace{D\nabla^2 c(x,t)}_{\text{Diffusion of cells}} + \underbrace{f(c)}_{\text{Cell proliferation}}, \tag{4.1}$$

where $D$ is the diffusion coefficient and $f(c)$ describes the growth dynamics of the tumor. Here, the diffusion coefficient is considered to be a constant since we assume that the brain is spatially homogenous (an assumption which is not necessarily accurate and will be relaxed in the following section). Tumor growth kinetics can be mathematically described through a number of previously-proposed models (discussed in Chapter 3). The commonly-used models are based on exponential, logistic and Gompertzian growth laws and each of these approaches can be justified under various growth conditions. In the time frame of interest, i.e. before the tumor becomes fatal, exponential growth could be used; however the more general

case of logistic growth is assumed in this thesis.

## 4.3 Spatially-Heterogenous Model

Although gliomas can be modeled using a simple spatially-homogenous model, it is clinically useful to include more detail in the model. As discussed in Chapter 2 (Section 2.3), the human brain is composed of different types of tissues and hence the infiltration capabilities of different types of tumors are not uniform or symmetric along these tissues. In the homogenous model discussed above, we have ignored this asymmetric nature of brain tissues.

Keeping this in mind, Swanson *et al.* [116] introduced an improved model for glioma growth with spatial heterogeneity considering two different diffusion coefficients for grey and white matter tissues. This mathematical model can be written as

$$\frac{\partial c(x,t)}{\partial t} = \nabla.\left(D(x)\nabla c(x,t)\right) + f(c). \tag{4.2}$$

Here, $f(c)$ is again the growth dynamics (assumed to be a logistic growth model) and $D(x)$ is the diffusion coefficient with two different values for grey and white matter, given by

$$D(x) = \begin{cases} D_G, & x \in \text{Grey matter} \\ D_W, & x \in \text{White matter,} \end{cases} \tag{4.3}$$

and $D_W > D_G$, since experimental studies show that glioma invasion in white matter is much faster than in grey matter. In order to ensure that the growth rate of the population decays as the cell numbers approach a maximum capacity,

all the simulations herein are done using a logistic growth model. The model formulation is completed by the initial condition $c(x,0) = c_0(x)$, where $c_0(x)$defines the initial spatial cell distribution, and no-flux boundary conditions which impose no migration beyond the brain boundary denoted by

$$\nabla c.\mathbf{n} = 0 \text{ for } x \text{ on } \partial B, \tag{4.4}$$

where $\mathbf{n}$ is the unit normal vector to the brain boundary $\partial B$ of B. The implementation details of the model on a realistic domain are given in the following sections.

This spatially-heterogeneous model can be further modified by incorporating various other information such as the anisotropic diffusion along white fibers or by coupling it to the mechanistic equations to study the properties of the tissue [27]. However, herein we use the above simple heterogenous model to study brain tumor growth and its response to various therapies.

## 4.4 Parameter Estimation

Clearly, the estimation of realistic parameter values is very important if the model is to be useful in understanding the behavior of real gliomas. The parameter values related to tumor growth are mainly chosen from previous mathematical models ([77], and the references therein). For cell proliferation, the parameter $\rho$ is assumed to be 0.012 (1/day), which corresponds to a volume doubling time of 2 months (for exponential growth). It is observed that the margin of a detectable tumor grows about 1.5 cm in 180 days [128, 144]. One should note that if we replace logistic growth with the exponential term and integrate both sides of Equation 4.1 with respect to $x$ (assuming a constant diffusion coefficient), we obtain a simple

exponential growth model for the total number of cells given by $N(t) = N_0 \exp(\rho t)$.

$$\left[\int_B \frac{\partial c(x,t)}{\partial t} dA = \int_B \nabla.\left(D(x)\nabla c(x,t)\right) dA + \int_B \rho c(x,t) dx\right] \tag{4.5}$$

Now by assuming that the total number of tumor cells is proportional to the tumor volume and assuming a simple spherical geometry, we can obtain similar kinetics for the detectable margin expansion as illustrated below.

$$\begin{aligned} &\pi r_1^2 - \pi r_2^2 = e^{\rho t_1} - e^{\rho t_2} \qquad (4.6)\\ &\pi(1.5)^2 - \pi(0)^2 = e^{\rho t_1} - 1 \\ &t_1 = \frac{ln(1+\pi(1.5)^2)}{\rho}. \end{aligned}$$

Assuming $\rho = 0.012$ (see Table 4.1), this leads to $t_1 = 174$ days. Finally, the aforementioned kinetics and Fisher's approximation $D = v^2/4\rho$ [77], can be used to give an average diffusion coefficient of approximately $D = 0.0013$ cm$^2$/day. Note that, the proliferation and diffusion constants may be varied depending on the type and grade of the brain tumor and its values are assumed to be in the range of 0.0012 to 0.012 and 0.00013 to 0.0013, respectively [116].

Following Swanson *et al.* [116] the obtained value for $D$ is defined to be the diffusion coefficient for the gray matter, and we assume a five-fold difference in the diffusion coefficients for gray and white matters (i.e. $D_W = 5D_G$). A typical section of the brain image [61, 1, 29] is used for the computational domain and to describe the gray and white matter distributions. It is assumed that tumor cells first proliferate in the initial phase without any diffusion, and that in the second phase, diffusion starts when the number of cells is approximately $10^5$ [77]. A tumor is detectable in CT scans only if the cell density is above a threshold level, and hence, only a portion of the entire tumor is visible in a medical image. This threshold value

is taken to be 400 cells/mm$^2$ [116]. The radius of the tumor at the time of detection is usually about 1.5 cm, thus tumor visibility is another criterion (in addition to the minimum threshold). Finally, it is assumed that $c_{lim} \approx N_0\rho/D_w \approx 10^5$ cells/cm$^2$. Note that the value of $N_0$, and consequently $c_{lim}$, is chosen such that tumor growth is compatible with clinical observations.

## 4.5 Implementation of Mathematical Model

Once we choose an appropriate mathematical model to study the growth and invasion of gliomas, the next step is to implement the model using analytical and/or numerical methods. In this section, we discuss the implementation of the spatially-heterogeneous model formulated above using a numerical approach.

### 4.5.1 Non-dimensionalization and Numerical Scheme

Non-dimensionalization is useful at many stages in model implementation. It increases insight about the key parameters by scaling them into appropriate magnitudes and at the same time helps in decreasing the number of free parameters. Here, we seek to non-dimensionalize the governing Equation 4.2 (tumor growth is assumed to be logistic with a limiting cell density $c_{lim}$), with the diffusion coefficient given by Equation 4.3, boundary condition (Equation 4.4) and the initial condition $c_0(x)$.

Introducing the dimensionless variables $(\tilde{x}, \tilde{t}, \tilde{c}(\tilde{x}, \tilde{t}))$ for distance $x$, time $t$ and cells $c(x,t)$ defined by

$$\tilde{x} = \sqrt{\frac{\rho}{D}}x \qquad \tilde{t} = \rho t \qquad \tilde{c}(\tilde{x}, \tilde{t}) = \frac{c(x,t)}{c_{lim}},$$

the above heterogeneous mathematical model can be written in the following dimensionless form (substituting these into Equations 4.2, 4.3, and 4.4 and dropping the tildes for $x, t$ and $c$ for notational convenience):

$$\frac{\partial c(x,t)}{\partial t} = \nabla.\left(D(x)\nabla c(x,t)\right) + c(1-c), \tag{4.7}$$

where

$$D(x) = \begin{cases} 1 & x \in \text{White matter} \\ \frac{D_G}{D_w} & x \in \text{White matter}, \end{cases} \tag{4.8}$$

with the boundary condition

$$\nabla c.\mathbf{n} = 0 \text{ for } x \text{ on } \partial B, \tag{4.9}$$

and initial condition (assumed to be Gaussian with a maximum cell density $a$ at the centre of the tumor $x_0$)

$$c_0(x) = a\exp\left(\frac{-|x-x_0|^2}{b}\right), \tag{4.10}$$

where $a = \frac{1}{\sqrt{2\pi\sigma^2}}$ and $b = 2\pi\sigma^2$ (for a two dimensional model).

The above dimensionless mathematical model (Equations 4.7 and 4.8), with the estimated parameters (Table 4.1), no-flux boundary condition 4.9 and a Gaussian initial distribution for tumor cells (4.10), is then implemented in MATLAB (as well as in C) using a finite difference method [109] as explained below.

Here, for simplicity, we use an explicit numerical scheme (forward Euler) with conditional stability although implicit schemes are unconditionally stable. For illustrative purposes, consider a one dimensional version of the above Equation 4.7 given by

Table 4.1: A list of parameter values

| Parameters | Symbol | Value | Reference |
|---|---|---|---|
| Growth rate | $\rho$ | 0.012 (1/day) | [30] |
| Diffusion Coefficient (Gray matter) | $D_G$ | 0.0013 ($cm^2$/day) | [128] |
| Diffusion Coefficient (White matter) | $D_W$ | $5D_G$ ($cm^2$/day) | [116] |
| Initial number of tumor cells | $N_0$ | $10^5$ (cells) | [77, 144] |
| CT threshold density | | 400 (cells/$mm^2$) | [116] |
| CT threshold radius | | 1.5 (cm) | [30, 128] |
| Gaussian variance | $\sigma$ | 0.35 | [93] |

$$\frac{\partial c(x,t)}{\partial t} = \frac{\partial}{\partial x}\left(D(x)\frac{\partial}{\partial x}c(x,t)\right) + c(1-c). \tag{4.11}$$

In order to solve this numerically, one should discretize the system in time and space. Thus, the domain will become a grid of size $N$ (with a space step size $\Delta x$ and temporal time step size $\Delta t$). Redefining $c(x,t)$ on this grid, we obtain,

$$c(x,t) \leftarrow c_i^k, \qquad 0 < i < N, \tag{4.12}$$

where $i$ and $k$ are integer indices and $N$ is the dimension of the grid.

Using the difference schemes, Equation 4.11 can be discretized as

$$\begin{aligned}\frac{c_i^{k+1}-c_i^k}{\Delta t} &= \frac{\partial}{\partial x}\left(D_i^k\left[\frac{c_{i+1/2}^k - c_{i-1/2}^k}{\Delta x}\right]\right) + c_i^k(1-c_i^k) + O(\Delta t) + O(\Delta x) \\ &= \frac{1}{\Delta x}\left(D_{i-1/2}^k\left[\frac{c_{i+1}^k - c_i^k}{\Delta x}\right] + D_{i+1/2}^k\left[\frac{c_{i-1}^k - c_i^k}{\Delta x}\right]\right) + c_i^k(1-c_i^k) \\ &\quad + O(\Delta t) + O((\Delta x)^2). \end{aligned} \tag{4.13}$$

Note that if we treat the diffusion coefficient as a constant (homogenous case), the right-hand-side of Equation 4.13 simply represents a central difference approximation whereas the left-hand-side follows a forward difference approximation. By rearranging Equation 4.13, we obtain

$$\begin{aligned}c_i^{k+1} = c_i^k + \frac{\Delta t}{(\Delta x)^2}\left(D_{i-1/2}^k\left[c_{i+1}^k - c_i^k\right] + D_{i+1/2}^k\left[c_{i+1}^k - c_i^k\right]\right) + c_i^k(1-c_i^k) \\ + O(\Delta t) + O((\Delta x)^2), \end{aligned} \tag{4.14}$$

where the right-hand side of the equation is fully known (starting from the initial condition) to compute the value of $c$ at subsequent time steps. Following similar steps, the boundary condition 4.9 also can be discretized as given below

$$c_{i-1}^k = c_i^k, \qquad \text{when} \qquad i = 0, \tag{4.15}$$

and

$$c_{i+1}^k = c_i^k, \qquad \text{when} \qquad i = N. \tag{4.16}$$

It can be shown that this finite difference scheme is stable and convergent as long as $\frac{\Delta t}{(\Delta x)^2} \leq \frac{1}{2}$ [109].

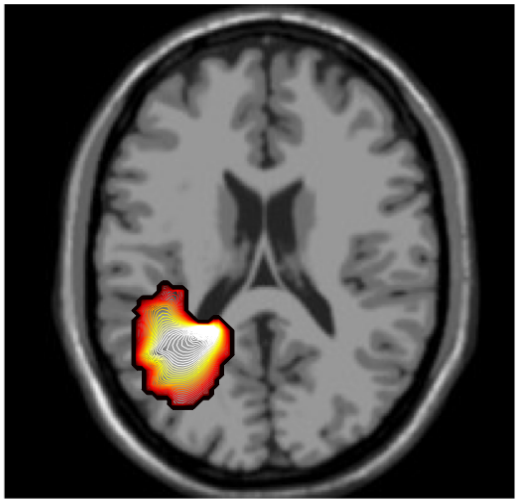

(a) At the time of diagnosis

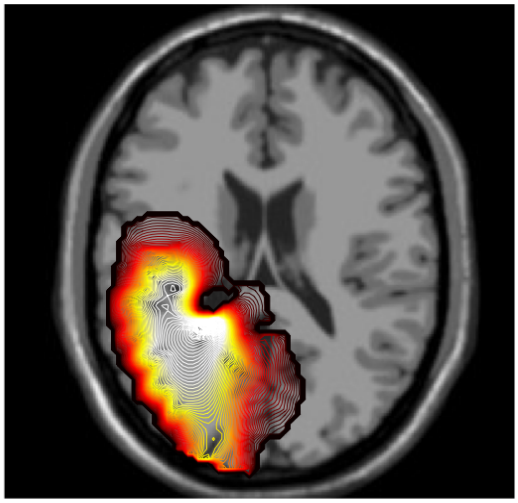

(b) At the time of death

Figure 4.1: The simulation of high grade glioma growth at diagnosis and patient death (Position 1). The colors indicate the gradient of malignant cell density

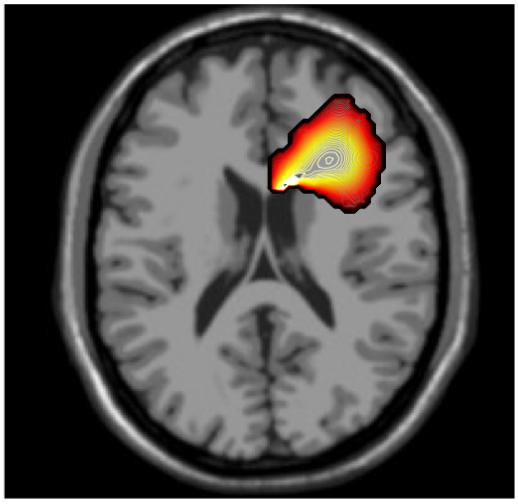

(a) At the time of diagnosis

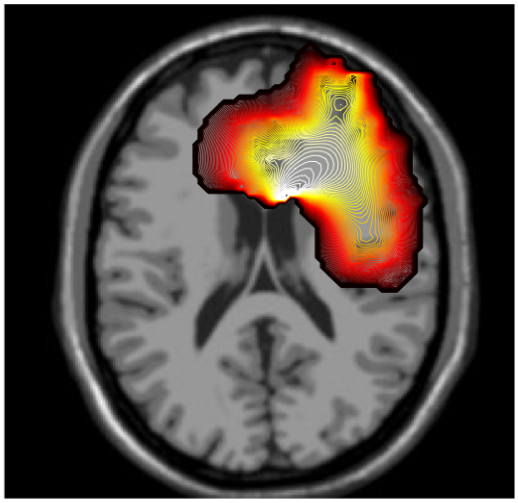

(b) At the time of death

Figure 4.2: The simulation of high grade glioma growth at diagnosis and patient death (Position 2)

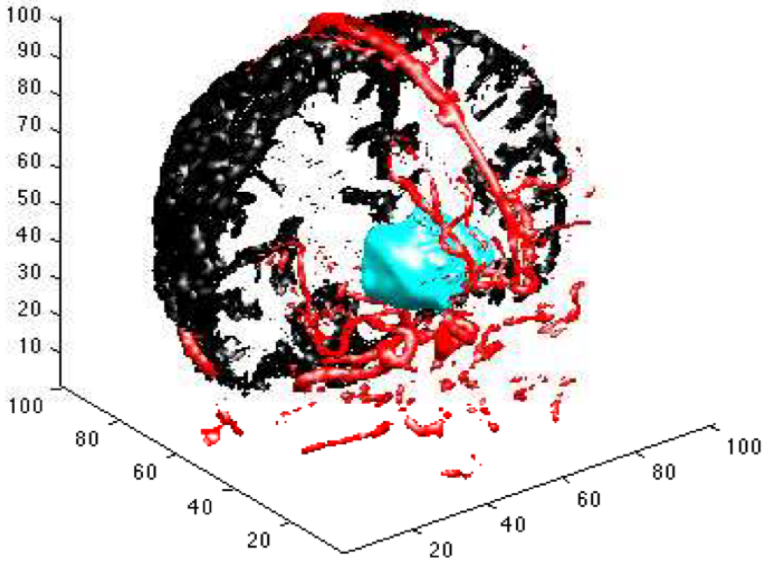


(a) Coronal view

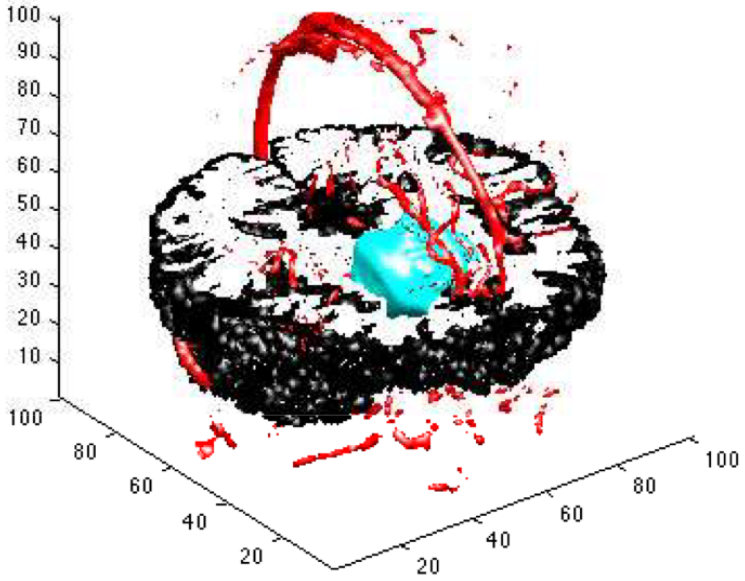


(b) Transaxial view

Figure 4.3: The simulation of high grade glioma growth in a three dimensional domain (axis corresponds to the non-dimensional grid points). The vessels shown are taken from the brain web [1]

### 4.5.2 Simulation Results

The following figures show simple two dimensional (Figures 4.1, 4.2) as well as a three dimensional (Figure 4.3) simulations of high-grade glioma in different locations in the human brain. The simulations are carried by considering real tumor boundaries as well as the properties of grey and white matter discussed in previous sections. It is assumed that the tumor is visible in CT scans when it reaches an area corresponding to 1.5 cm radius with a specific threshold density. At position 1 (Figure 4.1), the tumor is diagnosed around the $215^{\text{th}}$ day after initiation whereas at position 2 (Figure 4.2), this happens around the $205^{\text{th}}$ day. Death is assumed to occur when the radius of the detectable tumor reaches 3 cm; at position 1, this happens on the $474^{\text{th}}$ day after the initiation of the tumor, with a survival period of 37 weeks after diagnosis (consistent with survival rates seen in clinical situations). At position 2, this survival period is around 31 weeks since the tumor becomes lethal within 424 days after initiation. This indicates the significance of tumor location in the total survival time of the patient. Figure 4.3 shows a similar three-dimensional simulation of the tumor growth. Blood vessels are shown for illustrative purposes to indicate the possibility of extending the model further to include vasculature.

## 4.6 Short Summary

This chapter discusses the mathematical framework of glioma growth and invasion by considering the effects of various anatomical structures within the human brain. The details of numerical schemes and implementation methods are also explained. This heterogenous mathematical model for glioma growth and invasion is further used in the following chapters to study various treatment protocols and their effects

on patient survival.

# Chapter 5

# Brain Tumor: Modeling Treatment Strategies

## 5.1 Introduction

Surgery and radiotherapy constitute the initial treatments for malignant gliomas. Numerous studies have also attempted to demonstrate a better outcome with the addition of chemotherapy [37, 66, 36, 115, 114, 70]. Even with aggressive surgical resection and radiotherapy and/or chemotherapy, gliomas almost always recur, with fatal consequences. The median survival for patients diagnosed with glioblastoma multiforme (the highest grade glioma) has remained almost unchanged over the last few decades, at 6 to 12 months [66, 36]. Thus, due to their highly invasive and recurrent behavior, effective therapeutic strategies for gliomas are extremely important for improving survival time.

Several factors play important roles in the effectiveness of these treatments, such as the radius of resection, optimum dosing and scheduling of radiotherapy and

chemotherapy as well as their sequencing (concurrent, adjuvant or neo-adjuvant). Although more clinical trials are necessary to determine optimal treatment strategies, the development of mathematical models to address these questions is appropriate and timely. Carefully-devised and validated mathematical models may be useful for developing hypotheses to be tested in future clinical trials, and for optimizing the design of future trials.

There are a large number of mathematical models to study the effects of various treatment strategies; however, only a few of them have discussed the issues related to the optimal scheduling and sequencing of combination treatments (see for example, [60], and the references therein). In this chapter, we discuss the application of a spatio-temporal, reaction-diffusion model to study brain tumor growth and the effects of various treatments scenarios [93].

## 5.2 Surgery

Most patients will first undergo a surgical procedure for diagnostic and treatment purposes. Because gliomas are known to be infiltrating brain tumors and typically recur in spite of surgical resection, more extensive surgical resections may lead to an improved rate of survival [143, 11].

The surgical resection of a tumor can be mathematically incorporated into the simulations by removing all tumor cells within a definite location or above a certain threshold of detection (above which the tumor is visible in the CT/MRI scan) [144, 30]. We assume that the tumor is fatal when the total number of tumor cells reaches a specific critical number obtained through the analysis of clinical data [135] (details are discussed in the following sections). The survival status of various different grades of gliomas also can be modeled by changing the invasion (diffusion

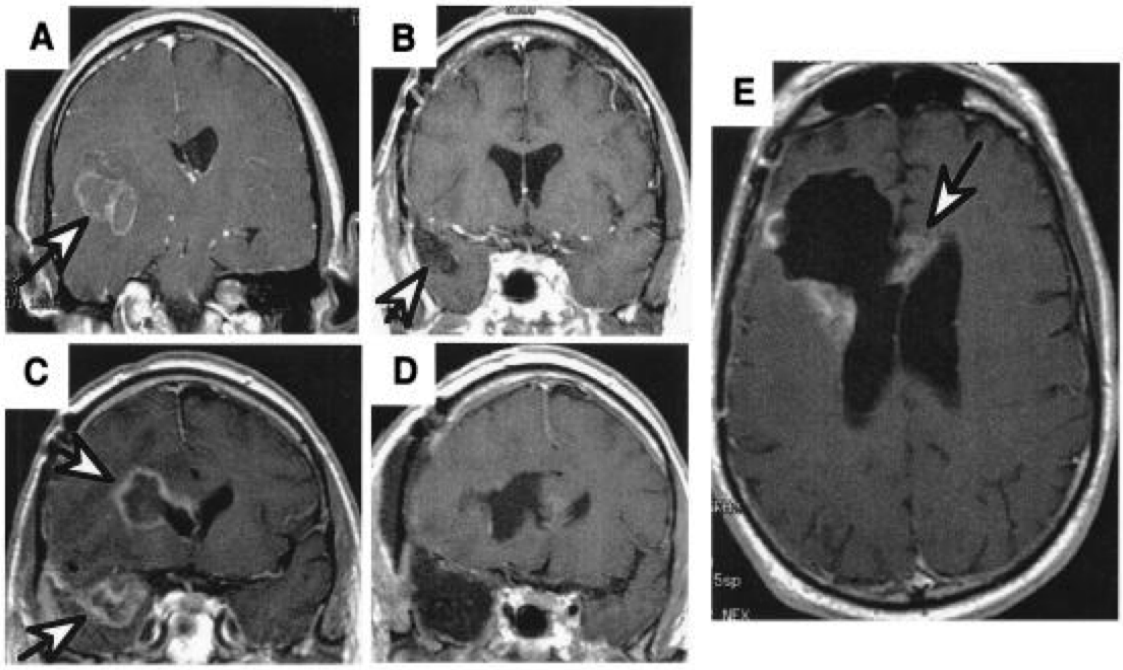


Figure 5.1: MRI scans of a patient with a right temporal GBM illustrating the spread of the disease (A) Presurgical scan, GBM (arrow) is surrounded with edema (B) Scan after surgery and radiation therapy showing gross total resection and clear resection cavity, and (C) six months later, showing recurrence not only at the resection margin (arrow) but a second focus of GBM across the Sylvian fissure in the frontal lobe (arrow) (D) Postresection scans of both recurrent tumors (E) Scan 3 months later, showing the tumor recurring at the resection margin and crossing the corpus callosum to the other hemisphere (arrow) [50] (Courtesy of PNAS)

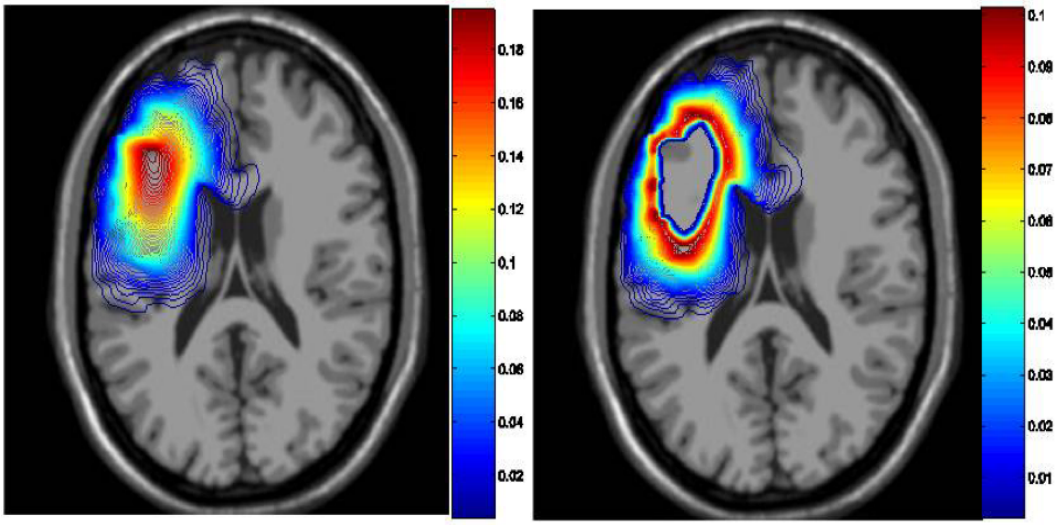


(a) Before surgery

(b) One day after surgery

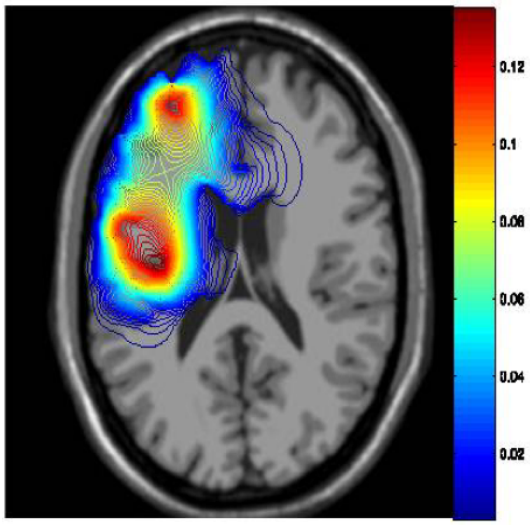


(c) 100 days after surgery

Figure 5.2: Numerical simulation of tumor growth and surgical resection

constant) and proliferation (growth rate) parameters [144]. Previous works [144, 30] also showed that by increasing the resectional radius (up to a maximum of 2.5-3 cm) patient survival times may increase, although the tumor will eventually reappear with fatal consequences.

Figure 5.2 shows the numerical simulation of tumor growth before, one day after and 100 days after the surgery (Figure 5.1 shows the MRIs of brain tumor before and after surgery). It can be seen from the figures that even after gross resection, the tumor reappeared in multiple positions as often observed in clinical scenarios. The recurrence of the tumor makes postoperative therapeutic strategies such as radiotherapy and chemotherapy a necessity to reduce tumor progression, which we discuss in the following sections.

## 5.3 Modeling Chemotherapy

In addition to surgery and radiation therapy (which will be discussed in Section 5.4), chemotherapy may also be beneficial for some patients with high-grade gliomas. Chemotherapy can be administered before (neo-adjuvant), during (concurrent) or after radiotherapy (adjuvant) [66]. The chemotherapeutic effects can be included into the mathematical model using various cell kill hypotheses, which are discussed in detail in Chapter 3. With the aim of understanding how these cell-kill models behave in the case of gliomas, here we first compare the effects of chemotherapy using a log-kill and $\mathrm{E}_{\max}$ model for drug induced cell death. As explained previously, this effect of chemotherapy is included in the mathematical model (Equation 4.2) by the cell-kill term $G(c,t)$,

$$\frac{\partial c(x,t)}{\partial t} = \nabla.\left(D(x)\nabla c(x,t)\right) + f(c) - G(c,t), \tag{5.1}$$

together with the previously formulated initial and boundary conditions. Here,

$$G(c,t) = \begin{cases} k_1(t)c(x,t): & \log - \text{kill} \\ k_2(t)c(x,t)/(c(x,t)+\delta): & \mathrm{E}_{max} \end{cases} \tag{5.2}$$

where $k_i(t)$ is proportional to the drug concentration, $k_i(t) = 0$ implies no drug effect is present and $k_i(t) = k_i$ means the chemotherapy is on (note that $k_1$ and $k_2$ have different units). Following Tracqui *et al.* [128], $k_1$ is taken as 0.0552 (1/day). For the $\mathrm{E_{max}}$ model, two parameters $k_2$ and $\delta$ are fixed so that, both log-kill and $\mathrm{E_{max}}$ models kill the same number of cells at the end of chemotherapy: $k_2 = 1.275 \times 10^5$ (cells/day cm$^2$) and $\delta = 1.936 \times 10^6$ (cells/cm$^2$).

Figure 5.3 shows the results of numerical simulations, for both the total number of cells and the detectable area of tumor cells, obtained from log-kill and $\mathrm{E_{max}}$ models. We assumed that chemotherapy is applied in six courses of length 15 days with an interval of 42 days [128]. In the log-kill model, cell-kill is proportional to the tumor cell density (or the total number of tumor cells). Thus chemotherapy is more effective on larger tumors. In the $\mathrm{E_{max}}$ model, more drug is required to have the same effect on the total number of tumor cells as the log-kill model. Although the total number of tumor cells after treatment remains the same (note that the parameters for the $\mathrm{E_{max}}$ model are estimated by assuming similar effects as the log-kill model), the $\mathrm{E_{max}}$ model gives a better result in reducing the visible tumor area.

### 5.3.1 Temozolomide - An Effective Chemotherapeutic Agent

In the case of gliomas, conventional drugs often result in poor survival response; this poor response has been attributed in part to low brain vascular permeability (the "blood-brain barrier") and limited penetration of drugs into the tumor and adjacent

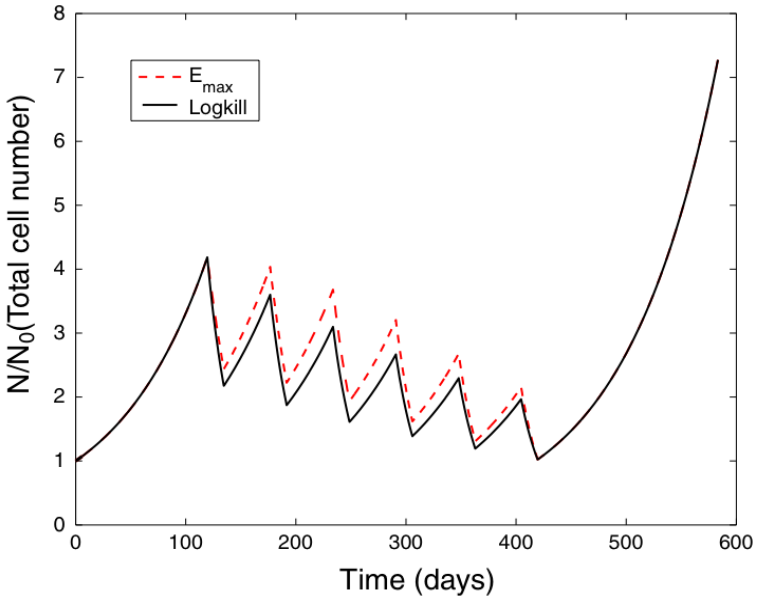


(a) Total number of cells

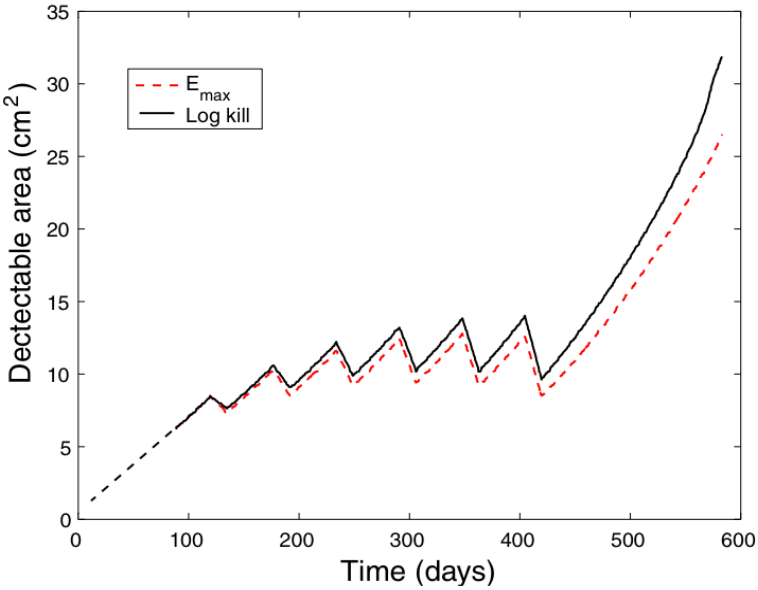


(b) Detectable area

Figure 5.3: The effect of chemotherapy on the total number of tumor cells and visible area of tumor

brain tissue [108]. However, recent phase III clinical trials [36, 115, 113, 70] have identified a survival advantage associated with the combination of postoperative radiotherapy and the cytotoxic agent temozolomide relative to radiotherapy alone (Figure 5.4).

Temozolomide is an orally-ingested alkylating agent that acts by causing lethal DNA damage in cancer cells. It is rapidly absorbed after oral dosing and easily crosses the blood-brain barrier [113]. Temozolomide shows a complete and rapid gastrointestinal absorption, although it varies between individuals [113]. Temozolomide is usually given in a daily dose of 200 mg/m$^2$ for 5 days a week over 4 weeks and several other dosing schedules are also undergoing clinical trials. Table 5.1 shows various schedules which are being investigated in clinical trials.

Table 5.1: Schedule and dosing of temozolomide (adapted from [113])

| Schedule | Dose (mg/m$^2$) | Dose intensity (mg/m$^2$/week) |
|---|---|---|
| Daily $\times$ 5 days, every 28 days | 200 | 250 |
| Daily $\times$ 7 days, every 14 days | 150 | 525 |
| Daily $\times$ 21 days, every 28 days | 100 | 250 |
| Daily $\times$ 42 days, every 70 days | 75 | 315 |

It has been also observed that temozolomide shows linear pharmacokinetics, with the area under the plasma concentration time curve (AUC) increasing in proportion to the dose. Hence, the temozolomide-induced cell kill can be studied mathematically by using a simple log-kill hypothesis (discussed in the previous section) in our previously-developed mathematical model (Equation 5.1). The clinical data of Stupp *et al.* [114] were used to estimate the parameter $k$, which represents the cell

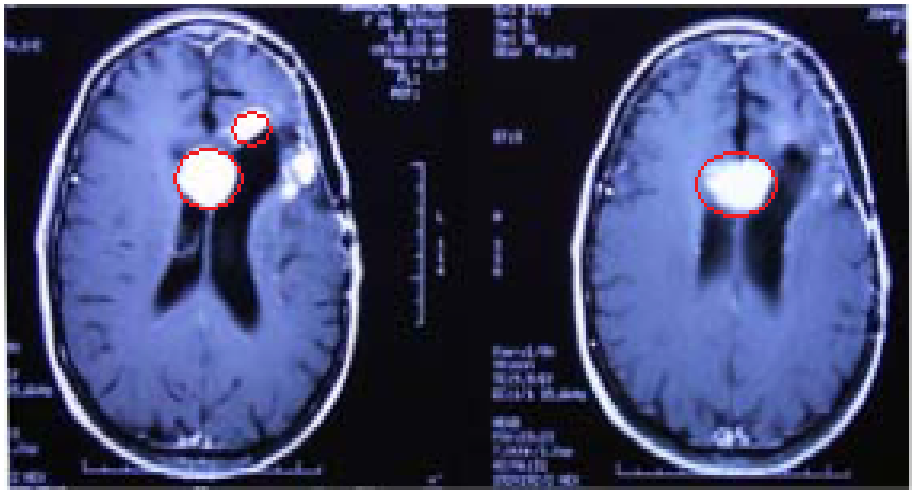

(a) Pre-treatment MRI

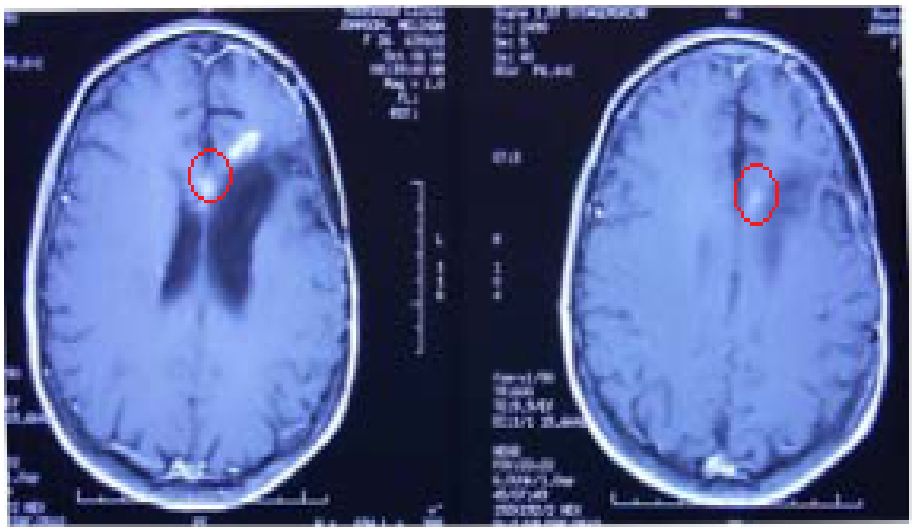

(b) Response following 2 five-day cycles of Temozolomide

Figure 5.4: The effect of temozolomide on brain tumor growth. GBM is shown within red circles (Courtesy of Dr. Susan Chang, Department of Neurological Surgery, UCSF)

death rate caused by chemotherapy (temozolomide); we take $k = 0.0196(1/\text{day})$. The details of the parameter estimation techniques are given in Section 5.6

## 5.4 Modeling Radiation Therapy

Radiation therapy is known to be an effective postoperative treatment for malignant gliomas, as it increases the survival time for patients compared to surgery alone [63, 10]. Most commonly, a radiation dose of 60 Gy in 2 Gy daily fractions is delivered using external high energy beams to a volume that encompasses the primary tumor (or resection cavity) and a margin of adjacent normal brain deemed at high risk of harboring subclinical disease [66]. Alternate schemes, including hyperfractionated radiation and accelerated-hyperfractionated radiotherapy have also been explored [135, 32, 139, 107, 78].

Similar to chemotherapy, the effect of radiotherapy is included in the spatio-temporal glioma model (Equation 4.7) using another cell kill term, $R(c,t)$, in the following fashion:

$$\frac{\partial c(x,t)}{\partial t} = \nabla.\left(D(x)\nabla c(x,t)\right) + f(c) - R(c,t). \tag{5.3}$$

Here, the radiation induced cell kill term $R(c,t)$ can be expressed using a number of mathematical models that are explained in detail in Chapter 3. However, to our knowledge none of these mathematical models has compared the effects of different fractionation protocols, especially when more than one fraction is used per day. Most of the theoretical studies in the literature have been using a simple linear quadratic model (Equation 3.10) [100], which cannot distinguish between the effects of a single fraction and multiple fractions per day, in particular if the total dosage remains the same.

Recognizing this gap in the literature, one of the main aims of this study is to compare the survival results of various fractionation schemes that are used in current clinical practice. Here, for low-dose-rate and fractionated radiotherapy (Equation 5.5), in which there is incomplete repair between fractions and significant repair during fractions, the cell kill term $R(c,t)$ can be expressed as

$$R(c,t) = R_{eff} k_R(t) c(x,t), \tag{5.4}$$

where $R_{eff}$ [80] is the effect of $n$ fractions per day given by (derivation follows in the next section),

$$R_{eff} = \alpha(nd) + \beta n d^2 \left[ g(\mu\tau) + 2\left( \frac{\cosh(\mu\tau) - 1}{(\mu\tau)^2} \right) h_n(\phi) \right], \tag{5.5}$$

and $k_R(t)$ represents the temporal profile of the radiation schedule. Here, $\alpha$ and $\beta$ are the sensitivity parameters, $d_t$ is the dose rate at time $t$, and $\mu$ is the half time for repair of radiation-induced DNA damage ($\mu = \ln 2/T_h$, where $T_h$ is the repair half time). Since Equation 5.5 incorporates the effect of $n$ fractions per day, we can simply use a time step of one day in the simulations. Thus $k_R$ is simply one on the day of radiotherapy application and zero otherwise. In Equation 5.5, as mentioned, $n$ is the number of fractions per day, $\tau$ is the irradiation duration, the function $\phi = \exp\left(-\mu(\tau + \Delta\tau)\right)$, where $\Delta\tau$ is the time interval between fractions, and $g(\mu\tau)$ and $h_n(\phi)$ are defined as

$$g(\mu\tau) = 2\left( \frac{\mu\tau - 1 + exp(-\mu\tau)}{(\mu\tau)^2} \right), \tag{5.6}$$

and

$$h_n(\phi) = 2\left( \frac{n\phi - n\phi^2 - \phi + \phi^{n+1}}{n(1-\phi)^2} \right). \tag{5.7}$$

Table 5.2: A list of parameter values - treatment scenarios

| Parameters | Symbol | Value | Reference |
|---|---|---|---|
| Cell death rate (Chemotherapy) | $k$ | 0.0196 (1/day) | Fitting to data[115] |
| Number of fractions/ day | $n$ | 1 - conventional<br>2- hyperfractionated | [135][139] |
| Time interval | $\Delta\tau$ | 1 day -conventional<br>6 h - hyperfractionated | [107][78] |
| Sensitivity ratio | $\alpha/\beta$ | 10 (Gy) | [94] |
| Sensitivity parameter | $\alpha$ | 0.027 ($Gy^{-1}$) | Fitting to data from [135, 139, 107, 78] |
| Repair half rate | $\mu$ | 0.46 ($1\ h^{-1}$) | Fitting to data from [135, 139, 107, 78] |

To estimate the radiobiologic parameters $\alpha$, $\alpha/\beta$ and $\mu$, as well as other radiotherapy parameters, we use published clinical data for malignant brain tumors involving different schedules of radiation therapy (see Section 5.5). The number of fractions per day, $n$, is one for conventional fractionation and usually two for hyperfractionated treatment. The time interval between fractions $\Delta\tau$ is therefore one day for the former and 6 hours for the latter. The duration of irradiation per fraction is usually very small, and we assume a value of 0.2 hours. The dose-rate (or total dose) and total treatment period vary for different clinical studies (see Section 5.5 and Table 5.2). The ratio of the sensitivity parameters $\alpha/\beta$ is characteristic of different types of tissues [122] and, for glioma, we consider $\alpha/\beta = 10\ Gy$ [94]. The parameters $\alpha$ and $\mu$ are derived in the following sections by comparing the model

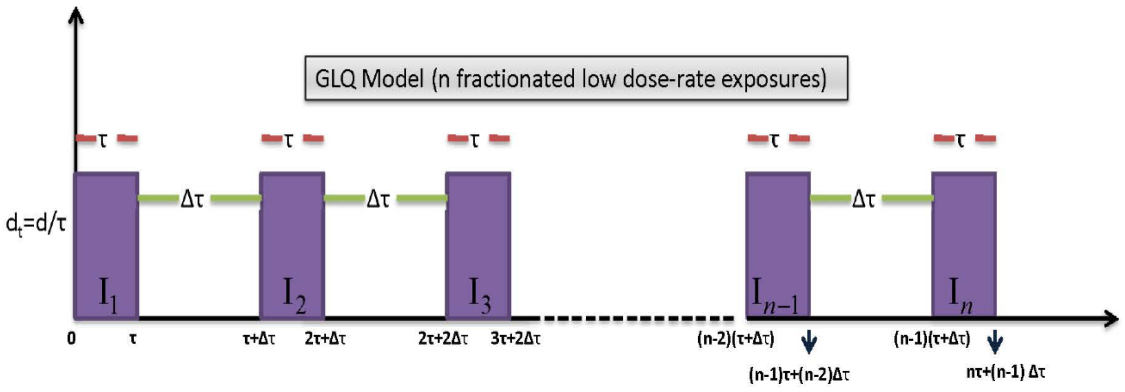


Figure 5.5: Schematic diagram of the treatment schedule for the generalized LQ model

predictions for median survival to published clinical data.

### 5.4.1 Derivation of $R_{eff}$ (radiation effect for n fractions per day)

Considering a generalized linear-quadratic model (GLQ) (Equation 3.11, the final survival fraction ($s.f.$) of irradiated tumor cells after the completion of one day's therapy is given by,

$$\ln(s.f.) = \int_0^{t_f} \left[ -\alpha d_t - 2\beta d_t \left( \int_0^t d_t' e^{-\mu(t-t')} dt' \right) \right] dt, \tag{5.8}$$

where the parameters are as explained in the previous section and $t_f$ is the final treatment time. In low-dose fractionated radiotherapy, since each fraction of size $d$ is delivered with a duration of $\tau$ time, the dose rate $d_t$ of each fraction is given by $d_t = d/\tau$. Following the fractionation schedule in Figure 5.5, the dose rate can be

written as

$$d_t = \begin{cases} \frac{d}{\tau} & t \in I_{k+1} = \left[(k(\tau + \Delta\tau), k\tau + (k-1)\Delta\tau\right], k = 0...n-1 \\ 0 & t \notin I_{k+1}. \end{cases} \tag{5.9}$$

Following Thames *et al.* [122], we assume that the level of underlying biological effect after the irradiation is uniquely determined by the surviving fraction of the irradiated tissue and this level of radiation effect ($R_{eff}$) is related to the survival fraction by [122]

$$R_{eff} = -ln(s.f.), \tag{5.10}$$

or

$$\begin{aligned} R_{eff} &= -ln(s.f) \\ &= \int_0^{t_f} \left[\alpha d_t + 2\beta d_t \left(\int_0^t d_t' e^{-\mu(t-t')} dt'\right)\right] dt \\ &= \int_0^{t_f} \left[\alpha \frac{d}{\tau} + 2\beta \frac{d}{\tau} D_{eff}\right] dt, \end{aligned} \tag{5.11}$$

where

$$D_{eff} = \frac{d}{\tau} \int_0^t e^{-\mu(t-t')} dt' \tag{5.12}$$

gives the secondary effects of fractionation due to incomplete repair during $n$ fractions of size $d$ (per day) and is calculated for each irradiation fraction. For an interval of $I_{k+1}$, this $D_{eff}$ can be calculated as follows:

$$
\begin{aligned}
D^k_{eff}(t) &= \frac{d}{\tau}\int_0^t e^{-\mu(t-t')}dt' \\
&= \frac{d}{\tau}\left[\int_0^{\tau} + \int_{\tau+\Delta\tau}^{2\tau+\Delta\tau} + \cdots + \int_{(k-1)(\tau+\Delta\tau)}^{k\tau+(k-1)\Delta\tau} + \int_{(k-1)(\tau+\Delta\tau)}^{t}\right] e^{-\mu(t-t')}dt' \\
&= \frac{d}{\tau}\left[\sum_{i=0}^{k-1}\int_{i(\tau+\Delta\tau)}^{(i+1)\tau+i\Delta\tau} e^{-\mu(t-t')}dt' + \int_{(k-1)(\tau+\Delta\tau)}^{t} e^{-\mu(t-t')}dt'\right] \\
&= \frac{d}{\tau\mu}\left[\sum_{i=0}^{k-1}\left(e^{-\mu(t-(i+1)\tau-i\Delta\tau)} - e^{-\mu(t-i\tau-i\Delta\tau)}\right) + \left(1 - e^{-\mu(t-k\tau-k\Delta\tau)}\right)\right].
\end{aligned}
\tag{5.13}
$$

Consequently, the resulting biological effect $R_{eff}$ after $n$ number of doses is given by

$$
\begin{aligned}
R_{eff} &= \int_0^{t_f}\left(\alpha\frac{d}{\tau} + \frac{2\beta d}{\tau}D_{eff}\right)dt \\
&= \left[\int_0^{\tau} + \int_{\tau+\Delta\tau}^{2\tau+\Delta\tau} + \cdots + \int_{(n-1)(\tau+\Delta\tau)}^{n\tau+(n-1)\Delta\tau}\right]\left(\alpha\frac{d}{\tau} + \frac{2\beta d}{\tau}D_{eff}(t)\right)dt \\
&= \alpha n d + \frac{2\beta d}{\tau}\left[\int_0^{\tau} + \int_{\tau+\Delta\tau}^{2\tau+\Delta\tau} + \cdots + \int_{(n-1)(\tau+\Delta\tau)}^{n\tau+(n-1)\Delta\tau}\right]D_{eff}(t)dt \\
&= \alpha n d + \frac{2\beta d}{\tau}\sum_{k=0}^{n-1}\int_{(k)(\tau+\Delta\tau)}^{(k+1)\tau+k\Delta\tau} D^k_{eff}dt.
\end{aligned}
\tag{5.14}
$$

Now substituting Equation 5.13 in to Equation 5.14, we get

$$
\begin{aligned}
R_{eff} = \alpha n d + \frac{2\beta d^2}{\mu\tau^2}\Bigg\{&\sum_{k=0}^{n-1}\int_{(k)(\tau+\Delta\tau)}^{(k+1)\tau+k\Delta\tau}\left(1 - e^{-\mu(t-k\tau-k\Delta\tau)}\right)dt \\
&+ \sum_{k=0}^{n-1}\sum_{i=0}^{k-1}\int_{(k)(\tau+\Delta\tau)}^{(k+1)\tau+k\Delta\tau}\left(e^{-\mu(t-(i+1)\tau-i\Delta\tau)} - e^{-\mu(t-i\tau-i\Delta\tau)}\right)dt\Bigg\}
\end{aligned}
\tag{5.15}
$$

which gives

$$R_{eff} = \alpha nd + \frac{2\beta d^2}{(\mu\tau)^2}\left\{\sum_{k=0}^{n-1}\left(\mu\tau + e^{-\mu\tau} - 1\right) + \sum_{k=0}^{n-1}\sum_{i=0}^{k-1}(-e^{-\mu(k-i)(\tau+\Delta\tau)} + e^{-\mu(k-i)(\tau+\Delta\tau)}e^{-\mu\tau} + e^{-\mu(k-i)(\tau+\Delta\tau)}e^{\mu\tau} - e^{-\mu(k-i)(\tau+\Delta\tau)})\right\}, \tag{5.16}$$

or

$$R_{eff} = \alpha nd + 2\beta d^2\left\{n\left(\frac{\mu\tau + e^{-\mu\tau} - 1}{(\mu\tau)^2}\right) + \frac{1}{(\mu\tau)^2}\sum_{k=0}^{n-1}\sum_{i=0}^{k-1}(e^{\mu\tau} + e^{-\mu\tau} - 2)e^{-\mu(k-i)(\tau+\Delta\tau)}\right\}. \tag{5.17}$$

Define $\phi$, $g(\mu\tau)$ and $h_n(\phi)$ as follows (these definitions are given in Section 5.4 as well; however, for the sake of clarity it is repeated here):

$$\begin{aligned} \phi &= e^{-\mu(\tau+\Delta\tau)} \\ g(\mu\tau) &= 2\left(\frac{\mu\tau - 1 + e^{-\mu\tau}}{(\mu\tau)^2}\right) \\ h_n(\phi) &= \frac{2}{n}\left(\frac{\phi}{1-\phi}\right)\left(n - \frac{1-\phi^n}{1-\phi}\right). \end{aligned} \tag{5.18}$$

Using these definitions, Equation 5.17 can be rewritten as,

$$\begin{aligned} R_{eff} &= \alpha nd + 2\beta d^2\left\{\frac{n}{2}g(\mu\tau) + \frac{1}{(\mu\tau)^2}\sum_{k=0}^{n-1}\sum_{i=0}^{k-1}(2\cosh(\mu\tau) - 2)\phi^{(k-i)}\right\} \\ &= \alpha nd + 2\beta d^2\left\{\frac{n}{2}g(\mu\tau) + 2\left(\frac{\cosh(\mu\tau) - 1)}{(\mu\tau)^2}\right)\sum_{k=0}^{n-1}\sum_{i=0}^{k-1}\phi^{(k-i)}\right\}. \end{aligned} \tag{5.19}$$

Using the following simplification,

$$\begin{aligned}\sum_{k=0}^{n-1}\sum_{i=0}^{k-1}\phi^{(k-i)} &= \sum_{k=0}^{n-1}\sum_{j=1}^{k}\phi^{j} \\ &= \sum_{k=0}^{n-1}\sum_{l=0}^{k-1}\phi^{l}\phi \\ &= \phi\sum_{k=0}^{n-1}\left(\frac{1-\phi^{k}}{1-\phi}\right) \\ &= \frac{\phi}{1-\phi}\left(n-\frac{1-\phi^{n}}{1-\phi}\right) \\ &= \frac{n}{2}h_n(\phi). \end{aligned} \tag{5.20}$$

Equation 5.19 can be expressed as

$$R_{eff} = \alpha nd + 2\beta d^2\left\{\frac{n}{2}g(\mu\tau) + 2\left(\frac{\cosh(\mu\tau)-1}{(\mu\tau)^2}\right)\frac{n}{2}h_n(\phi)\right\}. \tag{5.21}$$

By rearranging Equation 5.21, we obtain the following required simplified form of $R_{eff}$ as given in the main radiation induced cell-kill model Equation 5.11:

$$R_{eff} = \alpha nd + \beta nd^2\left\{g(\mu\tau) + 2\left(\frac{\cosh(\mu\tau)-1}{(\mu\tau)^2}\right)h_n(\phi)\right\}. \tag{5.22}$$

Although a few similar derivations can be found in the literature [122, 80], none of them have used this in the context of hyperfractionated/accelerated fractionated radiotherapy. Some of the limiting cases of this GLQ model are given below.

### Limiting Cases of GLQ Model

1. ***Incomplete repair (IR) model for acute fractionated exposure***

   Consider the case of $n$ number of acute fractions of dose $d$, where the frac-

tionation time $\tau$ approaches zero, i.e. as $\tau \to 0$

$$\begin{aligned}\lim_{\tau\to 0} g(\mu\tau) &= \lim_{\tau\to 0} 2\left(\frac{\mu\tau - 1 + e^{-\mu\tau}}{(\mu\tau)^2}\right) \\ &= 1 \end{aligned} \tag{5.23}$$

and

$$\lim_{\tau\to 0} 2\left(\frac{\cosh(\mu\tau) - 1}{(\mu\tau)^2}\right) = 1. \tag{5.24}$$

Using these approximations, the GLQ model (Equation 5.22) can be reduced to,

$$R_{eff} = \alpha nd + \beta nd^2 \left\{1 + h_n(\phi)\right\}, \tag{5.25}$$

which has the form of the incomplete repair model for acute fractionations.

2. ***Incomplete repair (IR) model for continuous exposure***

   As opposed to the above limiting case, now consider a continuous exposure to radiation beams for a duration of $\tau$ where the interval between the fractions $\Delta\tau$, approaches zero.

   Consider the Equation 5.21,

$$\begin{aligned} R_{eff} &= \alpha nd + 2\beta d^2 \left\{\frac{n}{2} g(\mu\tau) + 2\left(\frac{\cosh(\mu\tau) - 1}{(\mu\tau)^2}\right)\frac{n}{2} h_n(\phi)\right\} \\ &= \alpha nd + 2\beta d^2 \left\{\frac{n}{2} 2\left(\frac{\mu\tau - 1 + e^{-\mu\tau}}{(\mu\tau)^2}\right)\right. \\ &\qquad \left. +2\left(\frac{\cosh(\mu\tau) - 1}{(\mu\tau)^2}\right)\frac{n}{2}\frac{2}{n}\left(\frac{e^{-\mu(\tau+\Delta\tau)}}{1 - e^{-\mu(\tau+\Delta\tau)}}\right)\left(n - \frac{1 - e^{-\mu n(\tau+\Delta\tau)}}{1 - e^{-\mu(\tau+\Delta\tau)}}\right)\right\}. \end{aligned}$$

   Notice

$$\begin{aligned}
&\lim_{\tau\to 0}\left\{\frac{n}{2}2\left(\frac{\mu\tau-1+e^{-\mu\tau}}{(\mu\tau)^2}\right)\right.\\
&\qquad\left.+2\left(\frac{\cosh(\mu\tau)-1}{(\mu\tau)^2}\right)\frac{n}{2}\frac{2}{n}\left(\frac{e^{-\mu(\tau+\Delta\tau)}}{1-e^{-\mu(\tau+\Delta\tau)}}\right)\left(n-\frac{1-e^{-\mu n(\tau+\Delta\tau)}}{1-e^{-\mu(\tau+\Delta\tau)}}\right)\right\}\\
&=\left(\frac{n\mu\tau-n+ne^{-\mu\tau}}{(\mu\tau)^2}\right)+\left(\frac{e^{\mu\tau}+e^{-\mu\tau}-2}{(\mu\tau)^2}\right)\left(\frac{e^{-\mu\tau}}{1-e^{-\mu\tau}}\right)\left(n-\frac{1-e^{-\mu n\tau}}{1-e^{-\mu\tau}}\right)\\
&=\left(\frac{n\mu\tau-n+ne^{-\mu\tau}}{(\mu\tau)^2}\right)+\left(\frac{(1-e^{-\mu\tau})^2}{(\mu\tau)^2}\right)\left(\frac{1}{1-e^{-\mu\tau}}\right)\left(\frac{n-ne^{-\mu\tau}-1+e^{-\mu n\tau}}{1-e^{-\mu\tau}}\right)\\
&=n^2\left(\frac{n\mu\tau-1+e^{-\mu n\tau}}{(n\mu\tau)^2}\right)\\
&=\frac{n^2}{2}g(\mu n\tau). \qquad (5.26)
\end{aligned}$$

Thus,

$$R_{eff}=\alpha nd+\beta(nd)^2g(\mu n\tau), \qquad (5.27)$$

which has the form of an IR model for continuous exposure of a total dose of $nd$ given in a duration of $n\tau$ time.

3. ***Simple linear quadratic model***

The above two cases of IR models can be further simplified to obtain a simple form of the commonly used linear quadratic model.

(a) From the IR model of acute exposure

Consider the Equation 5.25

$$R_{eff}=\alpha nd+\beta nd^2\left\{1+h_n(\phi)\right\},$$

when n=1, i.e., when a radiation of dose $d$ is given in a single fraction, the term $h_1=0$ (this term accounts for the repair between the fractions) and hence, the above equation is reduced to a simple LQ model,

$$R_{eff}=\alpha d+\beta d^2, \qquad (5.28)$$

(b) From the IR model for continuous exposure

The term $g(\mu n\tau)$, denotes the repair of radiation damage within each fractionation period and if we assume that this repair rate is very small or $\mu\tau < 1$, the function $g(n\mu\tau)$ becomes,

$$g(n\mu\tau) = 2\left(\frac{n\mu\tau - 1 + e^{-\mu n\tau}}{(n\mu\tau)^2}\right)$$
$$= 1 + O(n\mu\tau)^3. \tag{5.29}$$

Using this approximation, Equation 5.27 can be written as,

$$R_{eff} = \alpha(nd) + \beta(nd)^2, \tag{5.30}$$

which is again the simple LQ model for a total radiation dose of $nd$.

## 5.5 Estimation of Radiobiologic Parameters and Survival Results

The effects of radiation therapy and resulting survival status are studied here with the help of Equations 5.3-5.7 using a number of simulations (simulation details are given in chapter 4).

The treatment of brain tumors with radiation therapy has been an area of intense research activity over the past several decades. Several clinical trials have been performed to study different radiotherapy strategies on patients with gliomas (for a review see [10]). Walker *et al.* [135], analyzed the radiation dose-response relationship among patients with malignant glioma participating in three successive Brain Tumor Study Group trials. Radiation doses between 45 and 62 Gy were administered in 1.7-2 Gy daily fractions, 5 days per week. They reported the survival curve of patients, demonstrating strong dose dependence. Werner-Waslik *et*

*al.* [139] reported the results of hyperfractionated and accelerated hyperfractionated radiation therapy for patients with malignant gliomas. Radiation therapy was delivered in two daily fractions, separated by 4-8 hours, 5 days per week. Patients received either 81.6 Gy in 1.2 Gy fractions, or 54.4 Gy in 1.6 Gy fractions, although the best survival was obtained for 72 Gy in 2 Gy fractions. Shibamoto *et al.* [107] and Nieder *et al.* [78] also compared hyperfractionated (1.3 or 1.5 Gy, twice a day) and conventional (1.8 or 2 Gy, daily dose) radiotherapy. The survival results for these clinical trials are given in Table 5.3. The clinical data from these studies was used to estimate the radiobiological parameters $\alpha$ and $\mu$ and validate the model predictions.

Using the clinical data of Walker *et al.* [135], the model is used to simulate treatment of a malignant glioma with conventionally fractionated radiotherapy up to a total dose of 60 Gy in 2 Gy daily fractions administered 5 days per week. Firstly the upper limit of the total number of tumor cells (beyond which the tumor is fatal) was fixed so that the treatment-free survival was 18 weeks without radiotherapy [135]. Radiotherapy was assumed to extend survival by 24 weeks [135]. Other aforementioned clinical data, as well as the details of their radiotherapy schedule were then used to repeat the same procedure (the upper limit of $N_{tot}$ is fixed from Walker *et al.* [135] data). The numerical simulations are performed to obtain the best fitted values for the parameters $\alpha$ and $\mu$ ($\alpha$= 0.027 Gy and $\mu$ = 0.46 $h^{-1}$). The estimated values for $\alpha$ and $\mu$ are of the same order as previous estimates ($\alpha = 0.06 \pm 0.05$ $Gy^{-1}$ and $\mu = 0.5$ $h^{-1}$)[94]. However, one should note that this model is based on the spatio-temporal evolution of tumor cells and, in addition, incorporates a radiotherapy contribution that has a more general form, applicable to both conventional and hyperfractionated treatment. As an example, following the clinical data of Walker *et al.* [135], the effect of radiotherapy on the total number

| No | Paper | Fractionation | Survival in months (Clinical) | Survival months (Model) | No of patients (median age) |
|---|---|---|---|---|---|
| 1 | Werner-Wasik 1996 [139] | Hyperfractionated (HF) 1.2 Gy/fr, 2 fr/day, to | | | |
| | | A : 64.8 Gy (54 fr) | 11.4 | 10.42 | 78(53.2) |
| | | B: 72.0 Gy (60 fr) | 12.7 | 11.13 | 158(21.2) |
| | | C: 76.8 Gy (64 fr) | 12.0 | 11.15 | 86(51.7) |
| | | D: 81.6 Gy (68 fr) | 11.7 | 12.03 | 120(51.1) |
| | | Accelerated HF 1.6 Gy/fr, 2 fr/day, to | | | |
| | | A: 48.0 Gy (30 fr) | 11.9 | 9.03 | 168(53.2) |
| | | B: 54.4 Gy (34 fr) | 10.8 | 9.68 | 137(53.1) |
| 2 | Nieder *et al.* 1999 [78] | Conventional fraction A: 2.0 Gy/fr, 5 fr/w to 60 Gy | 8.0 | 10.20 | 32(57) |
| | | Hyperfractionation A: 1.3 Gy/fr,2rac/d, 5day/w to 78 Gy (60 fr) | 7.0 | 11.77 | 34(57) |
| | | Accelerated HF A:1.5 Gy/fr, 2 fr/d, 5d/w to 60 Gy (40 fr) | 10.0 | 10.16 | 92(59) |
| 3 | Shibamoto 1997 [107] | Conventional fraction A: 1.8 Gy/fr to 64.8 Gy (36 fr) | 13.0 | 10.77 | 34(53) |
| | | Accelerated HF A: 1.5 Gy/fr, 2 fr/d to 9 Gy (46 fr) | 12.5 | 10.97 | 33(52) |
| 4 | Walker 1979 [135] | Conventional fraction A : 2 Gy/fr 5d/w to 60 Gy | 9.50 | 10.20 | 270(54) |

Table 5.3: Clinical results and model predictions for survival time

of cells and the tumor detectable area were simulated and given in the Figure 5.6. This figure shows that with the administration of radiotherapy it takes about 45.2 weeks for tumor cells to reach the upper limit. On the other hand, since there is a threshold for detecting the tumor, the visible area reaches fatality in about 22.85 weeks (compared to 24.5 weeks, when the total number of cells is monitored). The comparison of clinical data and the model predictions is summarized in Table 5.3. Clearly, there is reasonable agreement between the survival time from clinical data and numerical simulations.

In agreement with the clinical data, the model predicts that there is no difference in patient survival between conventional and hyperfractionated radiotherapy techniques, if the same total dose is administrated (see Tables 5.3 and 5.4). However, as mentioned in chapter 2, an advantage of hyperfractionated radiotherapy may be less (late) normal tissue toxicity, thereby allowing higher total doses to be safely administered. Recent clinical studies have shown that dose escalation up to 81.6 in 1.2 Gy fractions is feasible; however, no statistically significant improvement was observed, compared to the conventional radiotherapy schedule [139, 79]. The given model predicts that administration of a total dose of 81.6 Gy in 1.2 Gy fractions twice per day (see Table 5.3) should produce the best median survival of about 12 months (a median survival of 11.7 was observed in the clinical data of Werner-Wasik [139]). However, the conventional strategy is still the main radiotherapy schedule used in the treatment of most patients with brain gliomas. More randomized clinical studies are required to confirm if the use of hyperfractionated radiotherapy leads to longer survival times for patients with high-grade malignant gliomas.

Another useful concept in modeling radiation effect, that briefly we discussed in Chapter 3 is the concept of biological effective dose ($BED$). This allows an easy

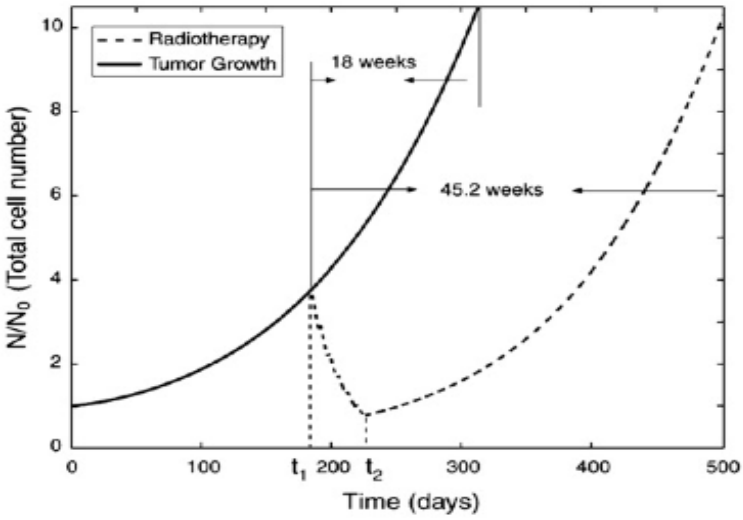


(a) Total number of tumor cells

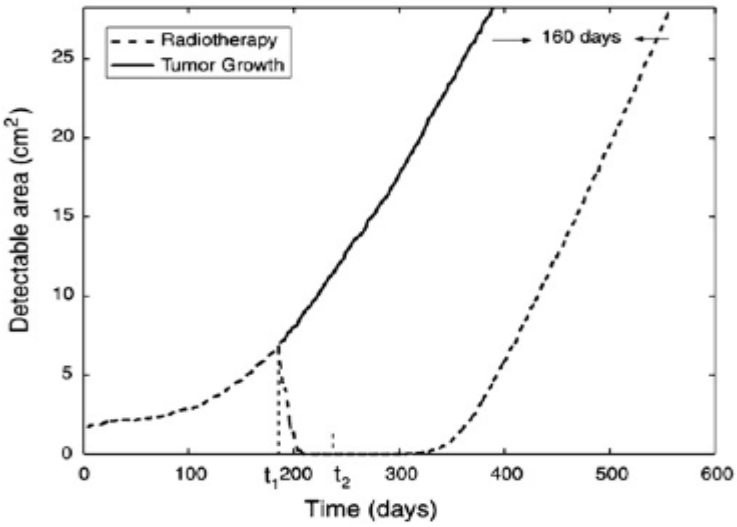


(b) Visible area

Figure 5.6: The effect of radiotherapy on the total number of tumor cells and the visible area of tumor, compared to the control tumor growth (no treatment); t1 and t2 are beginning and ending time of the radiotherapy, respectively

| No | Fractionation | Dose rate | D | BED | $BED_G$ |
|---|---|---|---|---|---|
| 1 | Conventional | A. 2.0Gy/30 frac | 60.0 Gy | 72.0 Gy | 71.64 Gy |
| | | B. 1.8Gy/36 frac | 64.8 Gy | 76.5 Gy | 76.11 Gy |
| 2 | Hyperfraction | A. 1.2Gy/54 frac | 64.8 Gy | 72.6 Gy | 72.79 Gy |
| | | B. 1.2Gy/60 frac | 72.0 Gy | 80.6 Gy | 80.87 Gy |
| | | C. 1.2Gy/64 frac | 76.8 Gy | 86.0 Gy | 86.26 Gy |
| | | D. 1.2Gy/68 frac | 81.6 Gy | 91.4 Gy | 91.66 Gy |
| | | E. 1.3Gy/60 frac | 78.0 Gy | 88.1 Gy | 88.41 Gy |
| 3 | Accelerated HF | A. 1.6Gy/30 frac | 48.0 Gy | 55.7 Gy | 55.89 Gy |
| | | B. 1.6Gy/34 frac | 54.4 Gy | 63.1 Gy | 63.34 Gy |
| | | C. 1.5Gy/40 frac | 60.0 Gy | 69.0 Gy | 69.24 Gy |
| | | D. 1.5Gy/46 frac | 69.0 Gy | 79.4 Gy | 79.63 Gy |

Table 5.4: Calculated values for BED and $BED_G$

comparison of different radiation schedules. If we hypothesize that the biological effect in tissues is determined by the survival fraction ($s.f.$) of target tumor cells, then $BED = -ln(s.f.)/\alpha = D(1 + d/(\alpha/\beta))$ for the simple LQ model [40]. A generalization of $BED$ for the fractionated low-dose-rate radiotherapy, also called "extrapolated tolerance dose", is then given by [80],

$$BED_G = D\left\{1 + \frac{d}{(\alpha/\beta)}\left[g(\mu\tau) + 2\left(\frac{\cosh(\mu\tau) - 1}{(\mu\tau)^2}\right)h_n(\phi)\right]\right\}. \tag{5.31}$$

An equivalent formulation is also given in Thames and Hendry [122]. For easier comparison of different radiotherapy schedules, the values of $BED_G$ are summarized

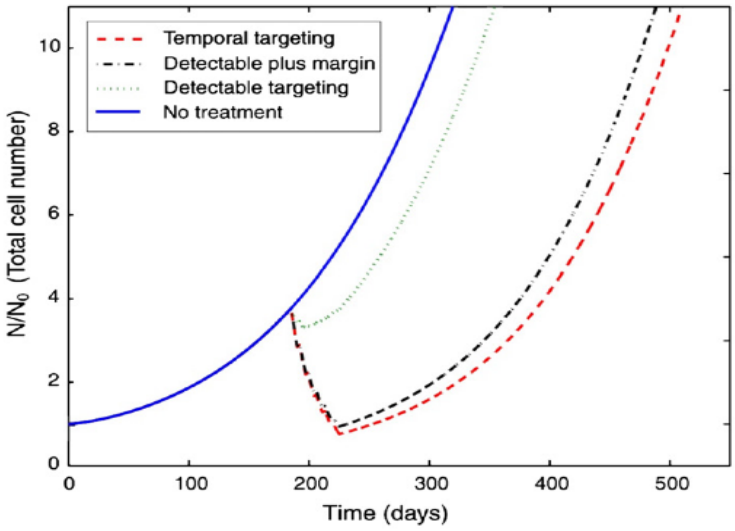


Figure 5.7: Comparison of the results for the total number of cells for no-treatment, temporal targeting, and spatial (GTV and CTV) irradiation

in Table 5.4. The difference between $BED$ and $BED_G$ depends on $n$ and $\mu$. The estimated value of $\mu$, corresponds to a repair half-time of 1.5 h, the difference, and hence the effect of fractionated radiotherapy, becomes more significant for higher $n$. The use of hyperfractionated radiotherapy without any change in overall treatment time (for the same total dose) can produce equivalent tumor control but a lower risk of late toxicity.

In radiotherapy treatments, magnetic resonance imaging is often used to produce high quality images and locate the gross tumor volume (GTV), or visible tumor region. In conformal radiotherapy, the radiation is used to kill the cells within usually a 1-2 cm margin around this GTV. In practice, this clinical target volume (CTV) usually includes the gross tumor (GTV) plus the surrounding edema, which is felt to be the region of highest subclinical clonogen density. To analyze this, the model is used to compare the effects of radiotherapy when applied

in three different cases: (a) only to the detectable portion of the tumor, (b) an extended detectable portion (with an extra 2 cm margin), and (c) as temporal (i.e. no-spatial dependence, where radiotherapy kills all the cells inside or outside the GTV) targeting. As shown in Figure 5.7, there is a significant difference between temporal targeting and irradiating only the visible tumor. However, the difference significantly reduces if radiotherapy is applied to the extended detectable portion (obtained from numerical simulations by increasing the detectable threshold, see the section on parameter estimation). This indicates the importance of an adequate consideration of spatial distribution in order to achieve efficient radiotherapy treatment. This also helps to reduce damage to healthy tissue due to irradiation.

## 5.6 Combination Therapy

Many of the commonly used chemotherapy drugs have limited activity in malignant gliomas. However, recent clinical trials indicate that the combination of radiotherapy and temozolomide have better survival outcomes compared to radiotherapy alone [115, 114]. Mathematically, the effects of this combination therapy can be studied by incorporating the radiation induced cell death, $R(c,t)$ and chemotherapeutic drug, Temozolomide induced cell death, $G(c,t)$ into the heterogenous growth and invasion model (Equations 4.7-4.10) and hence the model becomes,

$$\frac{\partial c(x,t)}{\partial t} = \nabla.\left(D(x)\nabla c(x,t)\right) + f(c) - G(c,t) - R(c,t) \tag{5.32}$$

with previously defined parameters, initial and boundary conditions.

In one of the clinical trials, Stupp *et al.* [115] compared patients who received standard focal radiotherapy alone or standard radiotherapy plus concomitant daily

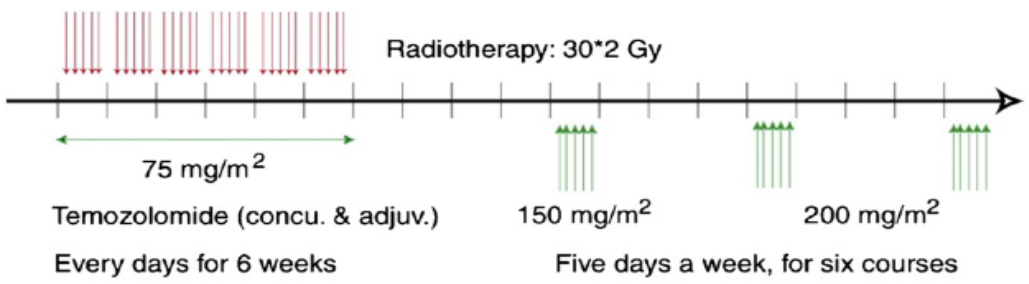


Figure 5.8: The clinical (and model) schedule for combination of radiotherapy and (concurrent and adjuvant) chemotherapy

temozolomide, followed by adjuvant temozolomide. Radiotherapy was given at a dose of 2 Gy per fraction per day, five days per week over a period of six weeks (total dose of 60 Gy). In their study, radiotherapy was delivered to the gross tumor volume with a 2-3 cm margin for the clinical target volume. Concurrent chemotherapy consisted of temozolomide, given 7 days per week (75 mg/m$^2$ per day) from the first day to the last day of radiotherapy. Patients then received up to six cycles of adjuvant temozolomide 5 days a week every 28 days (the dose was 150 mg/m$^2$ for the first cycle and was increased to 200 mg/m$^2$), see Figure 5.8 . They observed that the addition of temozolomide significantly prolongs the median survival from 12.1 months (for radiotherapy alone) to 14.6 months.

In the clinical study of Stupp *et al.* [115] radiotherapy was delivered to the detectable tumor with a 2-3 cm margin, resulting in a median survival time of 12.1 months for patients who received radiotherapy alone. The reported median survival time is better than the results of previous clinical trials (for example 9.5 months in Walker *et al.* [135]) with the same radiotherapy schedule and better than our model predictions. This could be because of different densities of tumor cells (for example in most studies surgery is carried out first, and there may be differences in

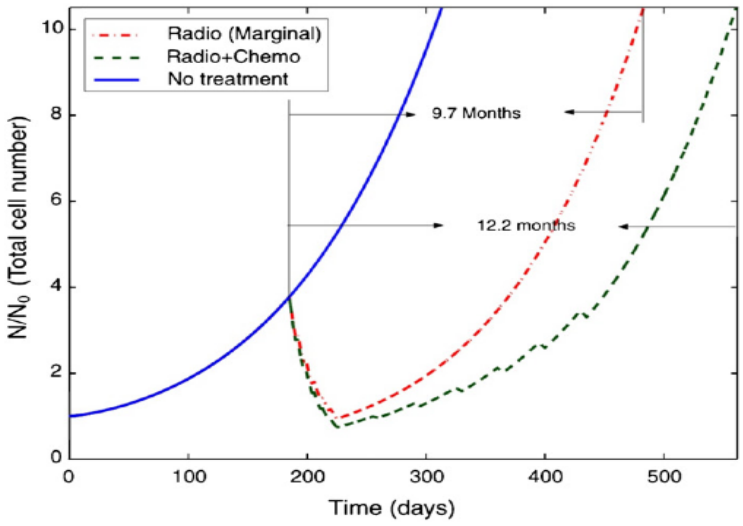


Figure 5.9: The effect of radiotherapy and its combination with (concurrent and adjuvant) chemotherapy on the total number of tumor cells

the time gap between surgery and postoperative treatments). The difference could also be due to selection of more favorable patients for inclusion in this study of combined treatment with radiotherapy and temozolomide. Nevertheless, for simulation proposes, the previously estimated parameters were used and the radiation therapy was considered to be given conventionally (2×30 Gy), where irradiation is now only applied to the clinical target volume (detectable tumor with a margin of about 2 cm, corresponding to a threshold of 30 cells/mm$^2$).

As explained in Section 5.3.1, Temozolomide shows linear pharmacokinetics with the area under the concentration time curve (AUC) increasing in proportion to the dose. Hence, a simple log-kill model is used here to model the the effect of temozolomide on cancer cells and the parameter $k$ is fixed in such a way that the addition of chemotherapy (given in exactly the same schedule as Stupp et al. [115], see Figure 5.8) produces a benefit of a 2.5 months increase in the median survival

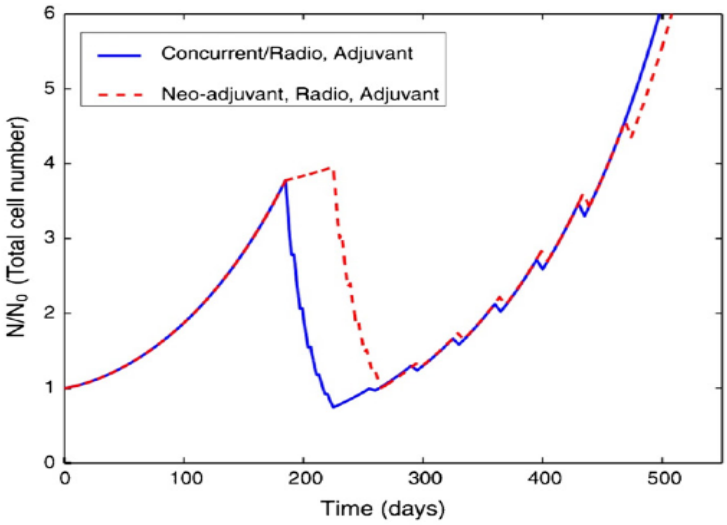


Figure 5.10: Comparing combination of radiotherapy and the concurrent/adjuvant chemotherapy with combination of radiotherapy and neo-adjuvant/adjuvan chemotherapy

time. Since the dosages are not the same for concurrent and adjuvant chemotherapy in the clinical study, we assume that the killing rate k is proportional to 200 mg/m$^2$ dosage, then the other dosages are the appropriate fractions of k. The result of simulations for the total number of cells is given in Figure 5.9. A single course of fractionated radiotherapy produced a delay of 9.7 months (this is different from the model prediction reported in Table 5.3, because irradiation was applied temporally, i.e. no-spatial dependence for the irradiation, compared to the current case where irradiation is only applied to the CTV). The addition of temozolomide increases the median survival to 12.2 months, i.e. a benefit of 2.5 months as observed in the clinical study.

The results of recent clinical trials have proposed the combination of radiotherapy and chemotherapy (temozolomide) as the new standard postoperative treat-

ment for most patients with brain tumor [36, 115, 114, 70]. However, the optimal sequencings of these treatments is not yet clear. Thus, in the next stage, the model is used to study the results for different sequencing of treatments. To compare the results, the same doses of radiotherapy and chemotherapy are applied by changing their order of applications.

The simulations were then performed for combinations of radiotherapy and neo-adjuvant plus adjuvant chemotherapy and these results were compared against the previous case of concurrent plus adjuvant chemotherapy. As shown in Figure 5.10, the model predicts that sequencing neo-adjuvant chemotherapy, and radiotherapy followed by adjuvant chemotherapy is a better strategy than the case when the first course of chemotherapy is given concurrently. A possible reason is that radiotherapy kills most of the cells in the target tumor volume, and hence, concurrent chemotherapy mainly affects invasive cells. On the other hand, neo-adjuvant chemotherapy affects (temporally) all the cells and then radiotherapy can kill the remaining cells in the target area. Although the model prediction does not show a significant difference, the combination of radiotherapy with neo-adjuvant and adjuvant chemotherapy produces less toxicity than the combination of radiotherapy with concurrent and adjuvant chemotherapy. More clinical studies are required to validate this prediction.

## 5.7 Short Summary

In this chapter, we used a spatio-temporal mathematical model, based on reaction-diffusion processes, and used the logistic growth function for the tumor growth kinetics. Radiotherapy was included as a generalized linear quadratic model, and the log-kill hypothesis was used to study the effects of chemotherapy [93]. The model

is then used to study fractionated and hyperfractionated radiotherapy schedules. The results of numerical simulation were compared to available clinical data to estimate radiobiologic parameters and to validate model predictions. The spatio-temporal nature of the model is used to study the effects of radiotherapy when applied to a tumor site with different margins. The results showed that there is a significant difference between irradiation of the detectable portion and the extended portion, where the effect of the latter is comparable with temporal targeting (giving radiation to the whole tumor). Finally, the combination of radiotherapy and (neo-adjuvant, concurrent, and adjuvant chemotherapy) were also analyzed using the mathematical model. The results of numerical simulations showed that neo-adjuvant chemotherapy, then radiotherapy followed by adjuvant chemotherapy could be a better strategy (producing less toxicity) than the concurrent application of radiotherapy and chemotherapy followed by adjuvant chemotherapy. More clinical studies are required to compare different schedules of combined therapy and to validate the model predictions.

Although this spatio-temporal model gives satisfactory agreement with respect to the clinical data, one of the main drawback of this model is that it ignores the details of the tumor microenvironment. In the literature, there is much experimental evidence that shows the importance of tumor microenvironmental factors in the successful application of various therapeutic strategies, especially radiation therapy. Among many, the most prominent aspects of the tumor microenvironment that influence the treatment and hence, the survival rates of patients are: hypoxia and high interstitial fluid pressure. In the following chapters, we will consider these microenvironmental factors and study how they affect therapeutic response.

# Chapter 6

# Hypoxia: Modeling, Estimation and its Effects on Cancer Treatments

## 6.1 Introduction

Tumor hypoxia is considered to be an important factor in tumor progression, which may affect the aggressiveness of tumors as well as metastatic and invasive potential of cancer cells [120, 132, 13]. It is also well-documented that the oxygenation dynamics in tumors strongly influences the response of cancer cells to treatments, particularly radiation therapy, to which hypoxic cells are more resistant than their normoxic counterparts [120]. A proper assessment of the distribution of hypoxia within a particular tumor before beginning therapy can highly affect the treatment outcome. Although there are several clinical protocols in practice to estimate the oxygenation status of tumors, most of these methods are invasive and their accuracy

might be limited by a number of factors such as location, stage, tumor heterogeneity, sampling strategy etc. An alternative approach to estimate tumor hypoxia is through theoretical simulations that incorporate knowledge of various measurable parameters supplemented by data obtained from other non-invasive clinical protocols. The formulation of one such theoretical method, with possible clinical applications, to quantify the hypoxia within a tumor and to study its influence on the response of radiotherapy is the main aim of this chapter [92].

In particular, this chapter has the following objectives. 1) to model tumor hypoxic conditions using a simple mathematical model which takes into account known spatial distributions of tumor vasculature (to this end, we use two-dimensional images of eight human glioma xenograft cross sections, which have been stained for the markers of perfusion, hypoxia and vasculature [99]); 2) to quantify hypoxia using simulated needle electrode measurements and compare results to the hypoxic fraction of cells as determined by calculating the hypoxic area; 3) to study the effects of needle electrode probe positions and probe directions using three different approaches (uniform, random, and radial); 4) to define the optimum number of needle measurement tracks in order to effectively quantify hypoxia in tumor tissues and 5) to evaluate the effects of hypoxia on radiation response.

## 6.2 Modeling Hypoxia

In the literature, there have been numerous theoretical approaches to model hypoxia and its effects on growth and control of tumors. A detailed discussion about these previous models are given in Section 3.3. Most of these approaches have modeled hypoxia by ignoring significant information, hence making it difficult, if not impossible to apply these models in clinical scenarios. Among many, one of

the more important factors that has been neglected to date in many models in determining the oxygenation status is the application of patient (tissue)-specific vascular distributions, which might be obtainable non-invasively through various current imaging techniques.

### 6.2.1 Computational Domain and Initial Distributions

To illustrate the usefulness of imaging techniques in the quest to satisfactorily model tumor hypoxia, we have used eight, two dimensional binary images of human glioma xenograft cross sections as computational domains on which a system of partial differential equations governing tumor growth and oxygen distribution are solved. These images, capturing perfusion, vascular structures and hypoxic regions (see Figures 6.1 - 6.2), serve as typical examples of tumor microenvironments. Rijken *et al.* [99] processed (details, as well as similar images, are presented in [99]) each of the eight cross sections through multiple staining and functional microscopic imaging techniques; sequential scanning of these processed tumor sections was then used to obtain the binary images on perfusion, vascular structures and hypoxic regions. They used these images to quantify and study the spatial relationship between perfused vessels and hypoxia [99].

Tumor hypoxia is often characterized by the existence of an abnormally structured and malfunctioning vascular distribution within the tumor [133]. There is experimental as well as theoretical evidence which supports the idea of this interdependence between the spatial distribution of the vasculature, perfused vasculature and tumor hypoxia [99, 104]. In the present model, the perfused vascular network is assumed to be correlated with the heterogenous distribution of hypoxia. Hence, the perfused vasculature is considered to be the source of oxygen supply and thus

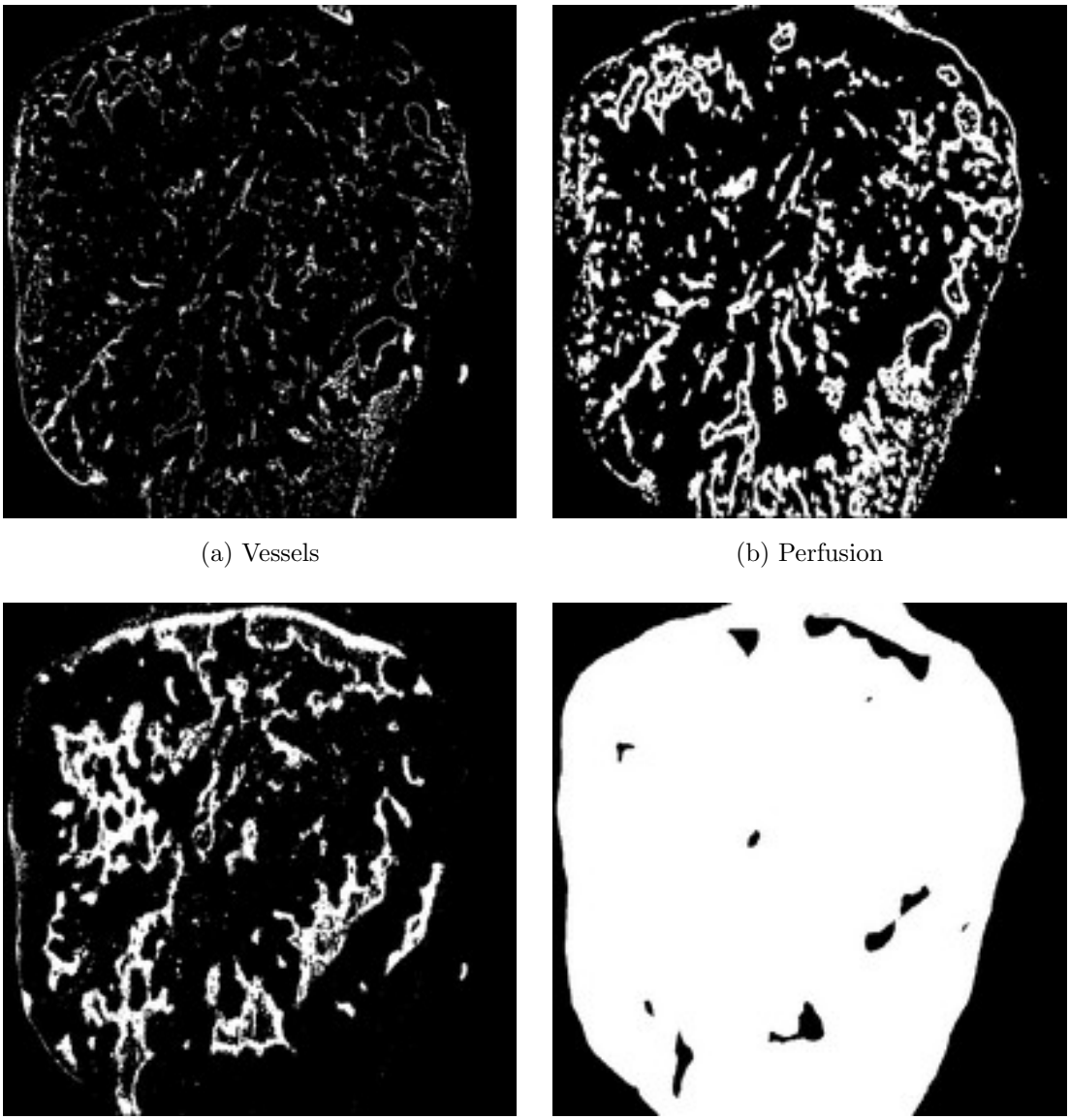

(a) Vessels

(b) Perfusion

(c) Hypoxia

(d) Tumor mask

Figure 6.1: Binary images of a glioma xenographt cross section, illustrating tumor blood vessels, perfused vessels, hypoxic area and total tumor area respectively (set 1)

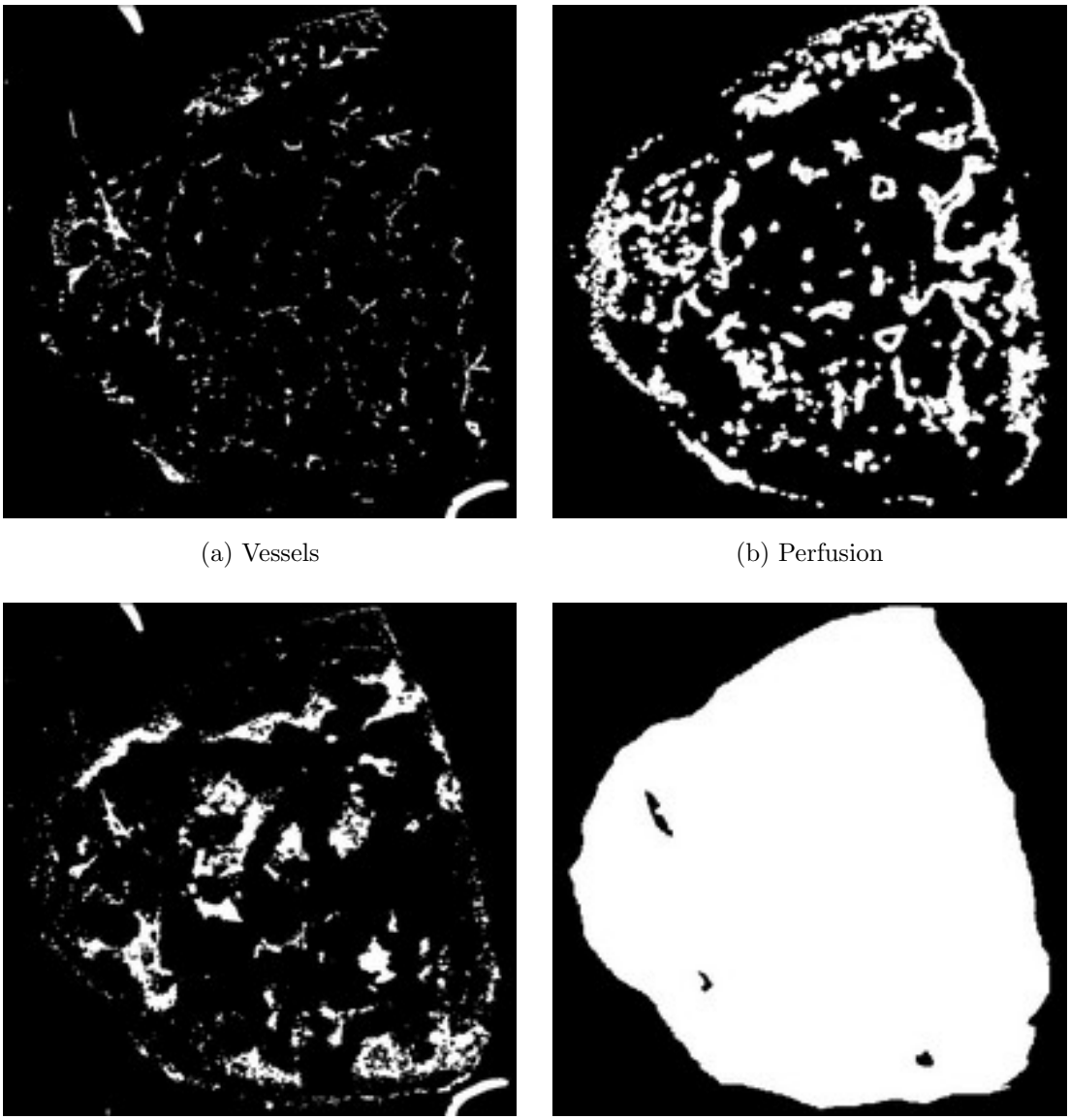

(a) Vessels

(b) Perfusion

(c) Hypoxia

(d) Tumor mask

Figure 6.2: Binary images of a glioma xenographt cross section, illustrating tumor blood vessels, perfused vessels, hypoxic area and total tumor area respectively (set 2)

gives the initial spatial distribution of oxygen concentration. Along this perfused vasculature, the initial oxygen distribution is also varied to analyze its effects on intra-vascular hypoxia. This perfused vascular network (at a fixed point in time) is obtained by combining the images of perfused areas (Figure 6.1b) and vascular structures (Figure 6.1a) using the logical "AND" operation [99] (Figure 6.3). The images of hypoxic regions (Figure 6.1c) are later used to compare the simulated hypoxic area and thus to validate the mathematical model. The total tumor area is estimated from the binary image representing the tumor mask (Figure 6.1d).

### 6.2.2 Mathematical Model for Hypoxia

Mathematically, most of the attempts to simulate hypoxia were mainly done by using a simple reaction-diffusion equation for oxygen distribution that represent the temporal and spatial changes in the oxygen and tumor cell concentrations [59, 33, 104]. If $K(x,t)$ denotes the oxygen concentration at $x$ position and time $t$, then its rate of change can be expressed as [59],

$$\frac{\partial K(x,t)}{\partial t} = \nabla.\left(D_k(x)\nabla K(x,t)\right) + rm_p(x,t) - \eta K(x,t) - \phi c(x,t), \tag{6.1}$$

where $D_k(x)$ is the diffusion coefficient (for simplicity as well as due to the lack of information from the biopsies, the tissue is considered to be homogenous in terms of its tendency to permit diffusion and thus we take $D_k(x)$ as constant), $\phi$ is the rate of oxygen consumption by cells and $\eta$ denote the rate of decay (assumed to be zero in the numerical simulations). Here, $m_p(x,t)$ stands for the density of the perfused vessels (in simulations, after the discretization of Equation 6.1, $m_p$ considered to be equal to 1 where the perfused vessels are present and zero otherwise); thus the term $rm_p(x,t)$ describes the production or supply of oxygen, where $r$ gives the supply rate. The formulation of the model is completed by prescribing boundary conditions

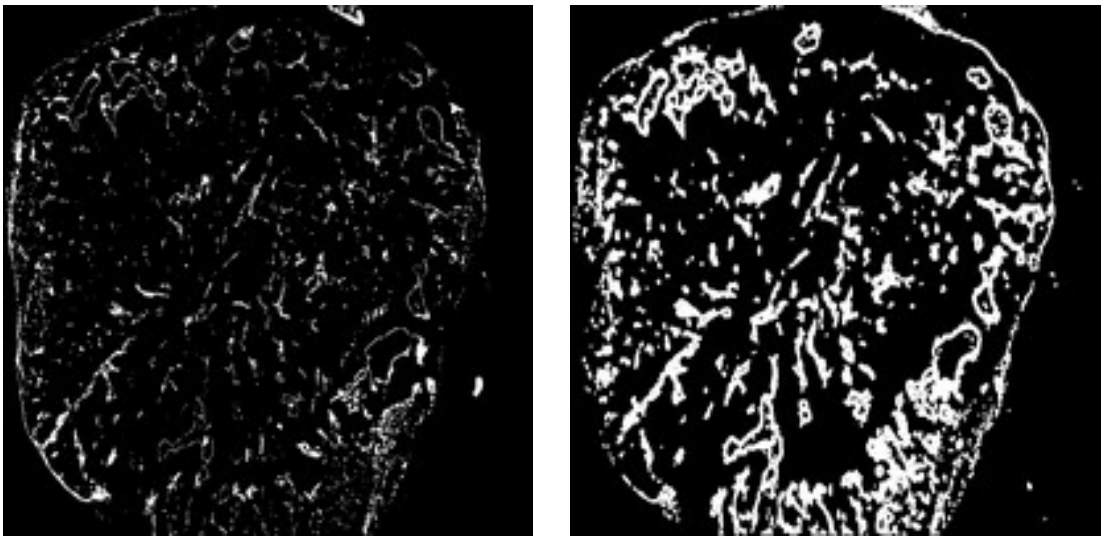

(a) Vessels



(b) Perfusion

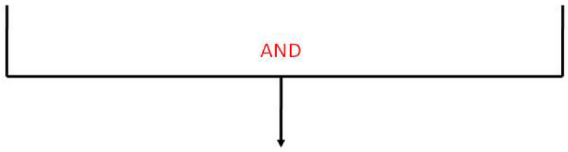


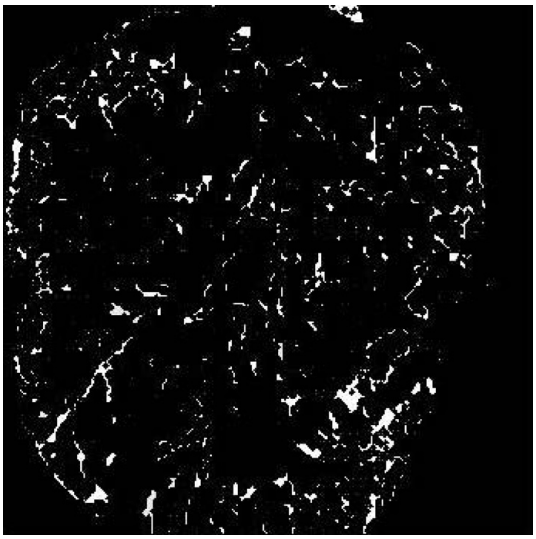

(c) Perfused vessels

Figure 6.3: Combining the images of vessels and perfusion to obtain perfused vasculature

and an initial condition (the initial spatial distribution of oxygen as determined from the image of perfused vasculature where the assumed intravascular oxygen distribution was prescribed only within this perfused vascular network). Here, since the focus is on simulating an instantaneous oxygen distribution map for a given vascular distribution, the real time evolution of the equations is not considered but rather a computational time that allows one to reach a steady state-like condition for oxygen distribution is used (details are give in following sections).

Similarly the temporal and spatial rate of change of cell concentration is considered to be the a net result of diffusion and proliferation. If $c(x,t)$ denotes the the density of the cells at position $x$ at time $t$ then,

$$\frac{\partial c(x,t)}{\partial t} = \nabla.\left(D_c(x)\nabla c(x,t)\right) + f(c) + \gamma m_p(x,t)c(x,t). \tag{6.2}$$

Here, $D_c(x,t)$ is the diffusion coefficient of tumor cells and $f(c)$ describes their growth given by the more general case of logistic growth, i.e. $f(c) = \rho c(x,t)(1 - c(x,t)/c_{lim})$, with $c_{lim}$ denoting the carrying capacity. The third term denotes the effect of the vascular network on the growth of the cells. As above, a no-flux boundary condition and an initial condition which defines the initial spatial distribution of tumor cells (assumed to be a Gaussian distribution) are used to complete the model formulation. The parameters are given in Table 6.1.

To generate the tissue-specific oxygen distribution, numerical simulations for each cross section are performed in MATLAB, using explicit finite difference methods (details are given in Section 4.5). Firstly, the simulation is carried out using Equation 6.2 over the image of the tumor cross section (tumor mask) (Figure 1d). This is done without the oxygen profile in order to obtain a distribution of tumor cells across the entire boundary. Once the tissue is generated, simulations are

| Parameters | Symbol | Value | Reference |
|---|---|---|---|
| Diffusion constant for oxygen | $D_k$ | $2.5 \times 10^{-5}$ ($cm^2s^{-1}$) | [71] |
| Rate of oxygen supply | $r$ | $8.2 \times 10^{-3}$ ($O_2s^{-1}$) | [71] |
| Cellular oxygen consumption* | $\phi$ | $3.8 \times 10^{-13}$ ($cm^2$ $O_2s^{-1}(cells)^{-1}$) | [105] |
| Diffusion constant for cells | $D_c$ | $4.05 \times 10^{-9}$ ($cm^2s^{-1}$) | [59] |
| Proliferation rate | $\rho$ | $1.85 \times 10^{-6}$ ($s^{-1}$) | [59] |
| Carrying capacity | $c_{lim}$ | $2.1 \times 10^{11}$ (cells $s^{-1}$) | [92] |
| Cellular growth rate (effect of vasculature) | $\gamma$ | $2.96 \times 10^{-6}$ ($s^{-1}$) | [59] |

Table 6.1: Numerical values of the parameters used in hypoxia model (* Assuming mass of 1 cell = $10^{-9}$ grams)

again carried out after coupling it with the model for oxygen concentration (Equation 6.1) to obtain the spatial map of oxygen concentration. One can then estimate the tissue hypoxia using this spatial distribution of oxygen concentration. The following sections in this chapter will illustrate various ways by which the hypoxia is quantified.

## 6.3 Estimation of Hypoxia

The oxygenation status of a heterogeneous tumor is often quantified using polarographic electrode measurements or through nitroimidazole binding and biopsies. These invasive techniques often have varying accuracy due to the restricted sampling space as well as limited accessibility. Here, hypoxia is quantified from the simulated model using two different methods: by calculating the percentage of

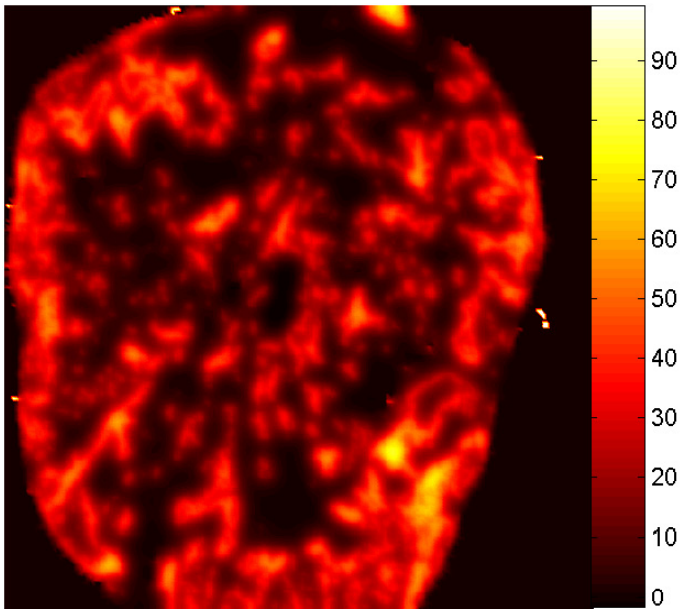


(a) Oxygen distribution (Color bar indicates the percentage of oxygen )

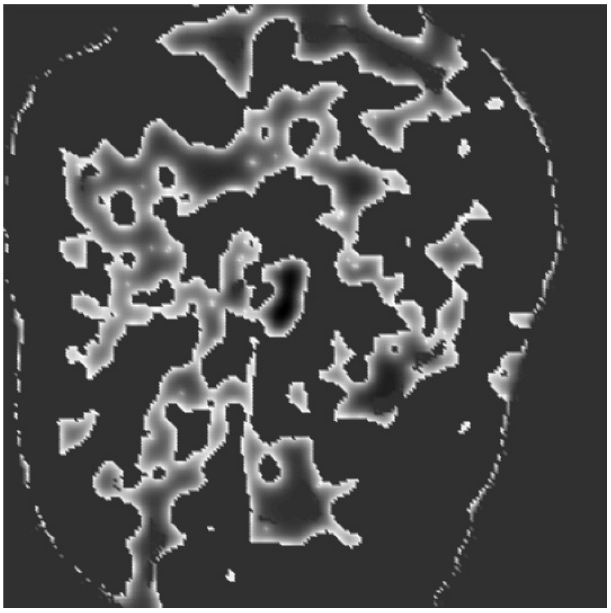

(b) Hypoxia distribution

Figure 6.4: Model simulated oxygen distribution as well as hypoxia

the total tumor section area that is hypoxic, and through needle electrode measurements (both simulated). These results are then compared to the measured percentage of hypoxic area as determined by pimonidazole staining (see Figure 6.1c for an example) – it should be noted that such data are used for the purposes of comparison and validation only and are not required by the model.

### 6.3.1 Percentage of Hypoxic Area

Standard clinical definitions used in quantifying hypoxia involve measuring the percentage of total biopsy area that falls below some specific staining threshold. This staining threshold usually depends on a number of different factors such as the binding properties of the hypoxia marker, intensity of staining detection, image capturing and processing techniques, and image noise [57]. However, for comparison purposes, it is assumed that these staining thresholds correspond to that of 10 mm Hg, 5 mm Hg and 2.5 mm Hg.

$$\text{Percentage of hypoxic area} = \frac{\text{Hypoxic area (area} \leq \text{threshold)}}{\text{Total area}} 100.$$

Our interest lies in finding the spatial distribution of hypoxia at a snapshot in time that will result from a particular distribution of perfused vessels and intravascular $O_2$ concentrations, rather than tracking the time-evolution of hypoxia. Yet it takes some computational (dimensionless) 'time' to arrive at this snapshot from our initial domain (recall that we begin the computation on a domain in which only the vasculature has non-zero oxygen concentration). As computational time proceeds (that is, as the number of iterations increases), the local oxygen concentrations increase and thus, in order to avoid dependence of our hypoxia quantification on computational time, we require a definition of hypoxia that considers relative, rather than absolute, quantities.

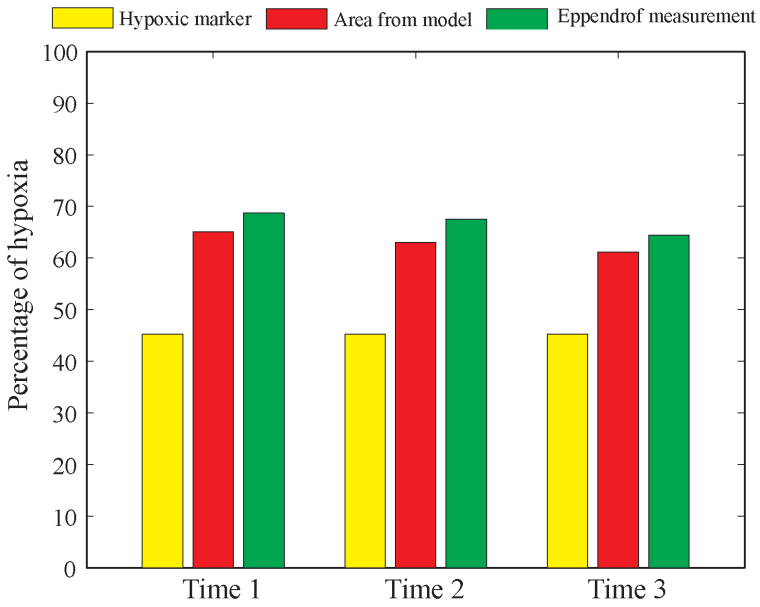


Figure 6.5: Comparison of hypoxic proportions (HP10) at three different time levels

Since the blood vessels act as the source of oxygen, it is assumed that (for computational convenience), at any time $t$, the maximum oxygen concentration value among all grid points represents the hundred-percent oxic condition in that tumor microenvironment. A square grid area is defined as hypoxic with a threshold level of 10 mm Hg (HP10), if its average oxygen content is below 10 percent of the maximum oxygen concentration value, i.e;

$$\text{Threshold level of HP10} = \max_{x}(K(x,t))\frac{10}{100}. \tag{6.3}$$

This definition yields a consistent hypoxic fraction at any computational time once the oxygen concentration in the model is reasonably diffused. In other words, this quantity achieves a steady state condition for oxygen concentration, which is what we require since we are estimating hypoxia according to a fixed spatial distribution of vasculature. Similar definitions hold for the remaining two threshold levels. The

sensitivity of this hypoxic criterion is analyzed by comparing the values of HP10 at different computational times (non-dimensional) and it is found that, for both theoretical measurement approaches, the hypoxic proportions estimated are similar for each time (Figure 6.5). This supports the validity of our hypoxic definition, since a given tumor microenvironment with a fixed vascular network (fixed in the sense that we consider timescales too small to permit changes in perfused vascular geometry) should yield an approximately fixed hypoxic proportion over these small time intervals.

### 6.3.2 Simulated Needle Electrode Readings

In clinical settings, a polarographic needle electrode is often used to measure the oxygen partial pressure. To estimate oxygen tension, the electrode needle is moved through the tissue to take a series of measurements along linear tracks 2-3 cm in length. Usually, 2-6 tracks of 20-30 measurements are performed to sample the oxygenation status of the entire tumor [142]. Due to the relatively large diameter of the needle, the values collected by such measurements usually account for the collective oxygen concentration of a certain volume of tumor cells around the tip of the electrode rather than a single cell. Taking this into consideration, Toma-Dasu *et al.* [125] developed a mathematical model that describes the response function of the electrode due to this measuring volume which is approximately 6 cell layers in radius. However, in the present model, the average diameter of the tumor cross sections is 6 mm, which is larger than the domain considered by Toma-Dasu *et al.* [125] to illustrate the response function. Therefore, for simplicity it is assumed that (i) each electrode measuring point in the computational domain represents a group of cells (5 to 6 cells with a diameter of 10- 12 $\mu$m, each) rather than a single cell and (ii) the value of oxygen concentration at the point of measurement represents

the average oxygenation status of the group of cells constituting that point.

In practice, the oxygen partial pressure measurements are taken using a needle electrode by moving it 1 mm forwards followed by 0.3 mm backwards to relieve the tissue pressure on the sensor membrane that might falsely indicate hypoxia. However, here, the needle electrode measurements are made by reading the simulated oxygen concentration value at 0.2 mm intervals along the track since our domain of simulations is a square grid of the size 6 mm. Six tracks of 20-30 measurements each are performed and the percentage of readings less than the threshold levels HP10, HP5 and HP2.5 (with the thresholds described in the previous section) are calculated for each of these six tracks,

$$\text{Percentage of hypoxia (for electrode)} = \frac{\text{No. of readings less than the threshold}}{\text{Total number of readings}} 100.$$

In order to study the spatial variation of oxygen readings within each tumor, these measurements are repeated by choosing the needle track uniformly (needle tracks are equidistant and parallel to each other), randomly or radially (tracks are selected in a clockwise manner but only between 10 o'clock and 2 o'clock), based on the assumption that the tumor is accessible only from one side (Figure 6.6). The results of simulated needle electrode measurements as well as previously explained percentage of hypoxic area are analyzed and compared in detail in the following sections.

### 6.3.3 Comparison of Simulated Hypoxia Estimates

Herein, the discussions are made by considering definitions of hypoxia corresponding to three different commonly considered threshold levels, i.e. mild (HP10), moderate

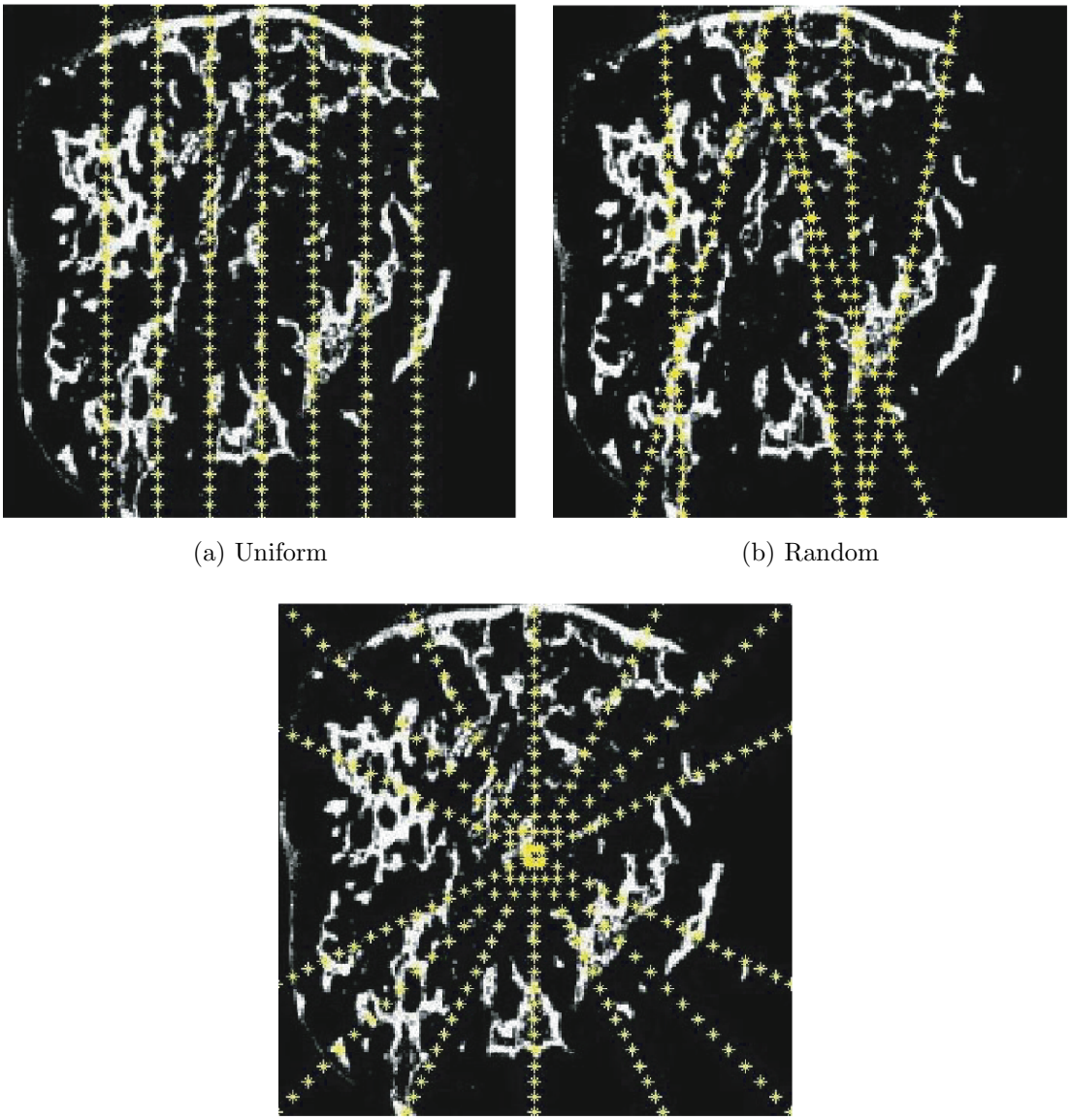

(a) Uniform

(b) Random

(c) Radial

Figure 6.6: Different needle electrode reading methods (for random approach, only one realization is shown)

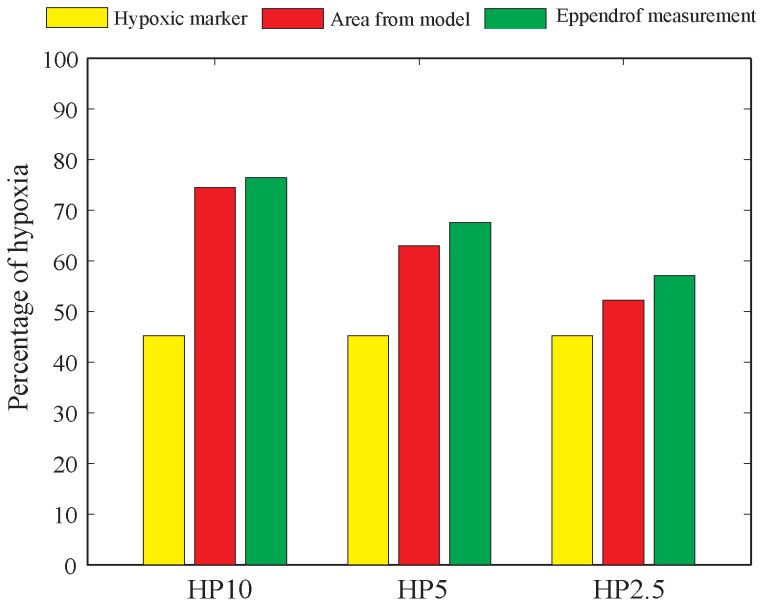


Figure 6.7: Comparison of hypoxic proportions at mild (HP10), moderate (HP5) and severe (HP 2.5) hypoxic levels

(HP5) and severe (HP2.5) hypoxic conditions. The percentage of total area that is hypoxic and the percentage of hypoxic readings (as determined by simulated needle electrode measurement) are then calculated with respect to these hypoxic thresholds and are compared against the known hypoxic proportions to study the accuracy of both the mathematical model and the probing techniques. The HP10, HP5 and HP2.5 hypoxic fractions for one tumor cross section are shown as box plots in Figure 6.7.

The hypoxic proportion as estimated from the original image is shown in yellow; note that it is same for all the three threshold values (since the data is available only as binary images). The red and green boxes represent hypoxia simulated by the computational model, which is quantified by estimating the percentage of the total area that is hypoxic and through simulated needle electrode measurements, respec-

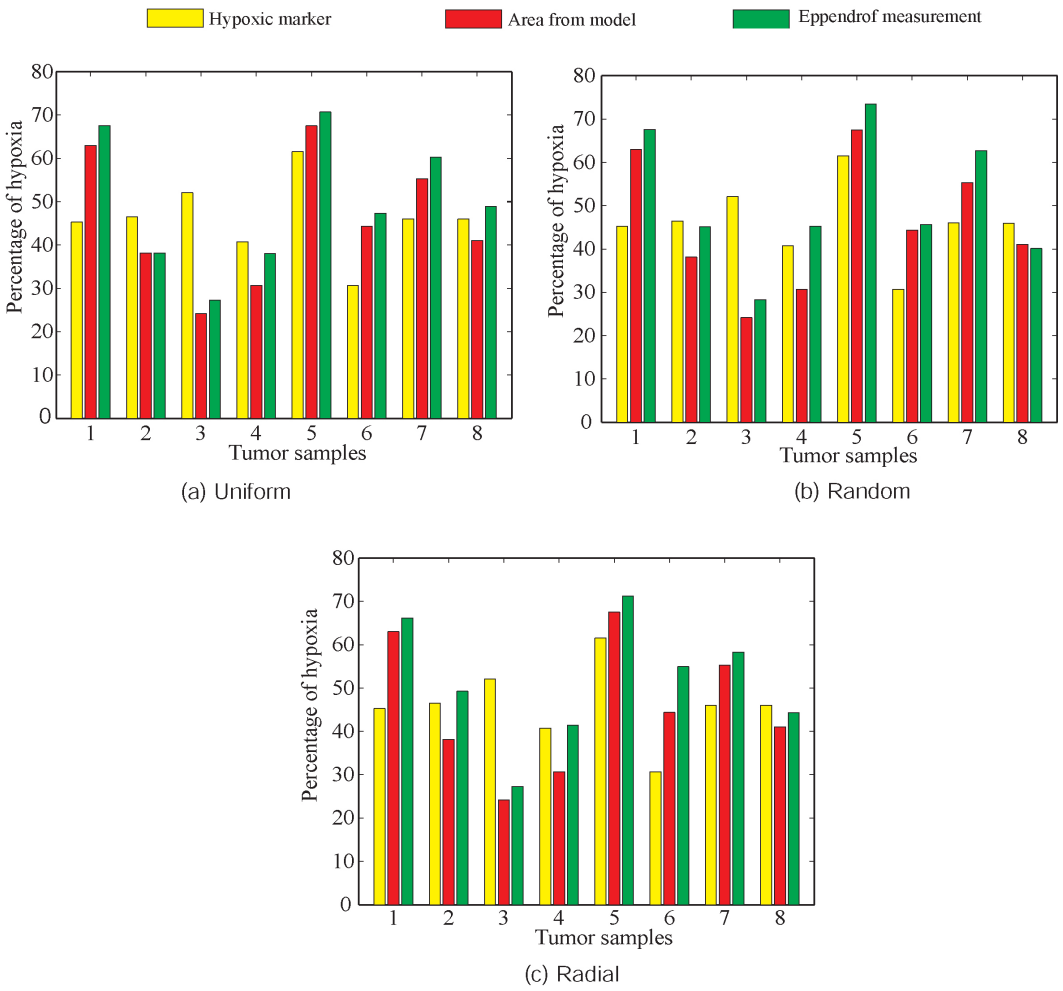


Figure 6.8: The graph shows HP5 estimations for eight tumor cross sections using three different needle measurement approaches. (Yellow - percentage of hypoxic area from the original image, red- percentage of hypoxic area from model and green - HP5 estimation using needle electrode)

| Sample | Vessel area (%) | Hypoxic area (%) | Threshold | Simulated area (%) | Polarographic electrode | | |
|---|---|---|---|---|---|---|---|
| | | | | | Uniform | Radial | Random |
| 1 | 8.1581 | 45.2698 | 10 mm Hg | 74.4811 | 76.4479 | 77.0833 | 82.9545 |
| | | | 5 mm Hg | 62.9988 | 67.5676 | 66.1458 | 67.6136 |
| | | | 2.5 mm Hg | 52.2262 | 57.1429 | 56.7708 | 57.3864 |
| 2 | 15.4913 | 46.4672 | 10 mm Hg | 52.747 | 55.4217 | 60 | 57.8035 |
| | | | 5 mm Hg | 38.1339 | 38.1526 | 49.2308 | 45.0867 |
| | | | 2.5 mm Hg | 27.6017 | 25.3012 | 42.0513 | 29.4798 |
| 3 | 20.1725 | 52.0705 | 10 mm Hg | 37.9127 | 42.5197 | 44.4444 | 43.9759 |
| | | | 5 mm Hg | 24.1618 | 27.9528 | 27.2727 | 28.3133 |
| | | | 2.5 mm Hg | 15.1108 | 18.5039 | 17.6768 | 19.8795 |
| 4 | 15.6967 | 40.7278 | 10 mm Hg | 49.531 | 53.4188 | 59.6685 | 61.6352 |
| | | | 5 mm Hg | 30.6814 | 38.0342 | 41.4365 | 45.283 |
| | | | 2.5 mm Hg | 18.8948 | 27.3504 | 26.5193 | 28.9308 |
| 5 | 7.4916 | 61.5296 | 10 mm Hg | 78.0461 | 79.7414 | 82.0652 | 81.6456 |
| | | | 5 mm Hg | 67.4953 | 70.6897 | 71.1957 | 73.4177 |
| | | | 2.5 mm Hg | 58.236 | 61.6379 | 61.413 | 65.8228 |
| 6 | 12.3227 | 30.6596 | 10 mm Hg | 58.5982 | 61.4108 | 67.3575 | 57.8035 |
| | | | 5 mm Hg | 44.3564 | 47.3029 | 54.9223 | 45.6647 |
| | | | 2.5 mm Hg | 33.3875 | 34.8548 | 44.0415 | 35.2601 |
| 7 | 10.0978 | 46.0116 | 10 mm Hg | 67.8908 | 72.6496 | 70.5882 | 74.0506 |
| | | | 5 mm Hg | 55.286 | 60.2564 | 58.2888 | 62.6582 |
| | | | 2.5 mm Hg | 45.0228 | 48.7179 | 49.7326 | 49.3671 |
| 8 | 13.3327 | 45.9818 | 10 mm Hg | 57.7553 | 63.7405 | 61.6915 | 62.7119 |
| | | | 5 mm Hg | 41.0636 | 48.855 | 44.2786 | 40.113 |
| | | | 2.5 mm Hg | 28.7652 | 33.2061 | 28.8557 | 28.8136 |

Table 6.2: Simulated and experimental hypoxic estimations

tively. It can be seen from figure (Figure 6.7) that, in the case of HP2.5, the proportion of model-generated hypoxia is in reasonable agreement with the proportion determined from the original images (a result that is consistent across the remaining samples of tumor cross sections). It should be noted that the available binary image of hypoxic area (Figure 6.1c) corresponding to our computational domain (obtained through biomarker staining and sequential scanning) allows us to estimate hypoxia (for comparison purposes) only at a single threshold level and hence we do not expect to see agreement across all three threshold levels in Figure 6.7. As mentioned earlier, these binary images of the hypoxic area reflect a number of factors relating to tissue preparation, staining absorption, staining threshold, image acquisition and image brightness, and in many experimental studies [57, 95, 56, 65] it has been observed that the intensity of hypoxic marker binding increases with increasing levels of hypoxia. According to Raleigh *et al.* [95], pimonidazole bindings usually occur at levels less than 10 mm Hg, and the half-maximal pimonidazole binding occurs around 2 mm Hg. Raleigh *et al.* [95] also showed that HP10 measurements with $pO_2$ needle electrodes correlate with pimonidazole binding surface area with a systematic offset of 36%, and this offset is smallest for HP2.5 (18%), which is consistent with this vasculature specific model predictions.

Table 6.2 shows the comparison between simulated and experimental hypoxic estimations at three different threshold levels. Overall, the best agreement between the simulated and measured values is for a simulation threshold of 5 mm Hg. However, a 5 mm Hg threshold significantly over-estimated hypoxia in some samples and under-estimates it in others. On the other hand, a threshold of 2.5 mm Hg provides very good correlation with measured values in four of the eight tumors samples and underestimates hypoxia in the other four. This difference between the simulated and higher measured values may be either due to 1) a component of

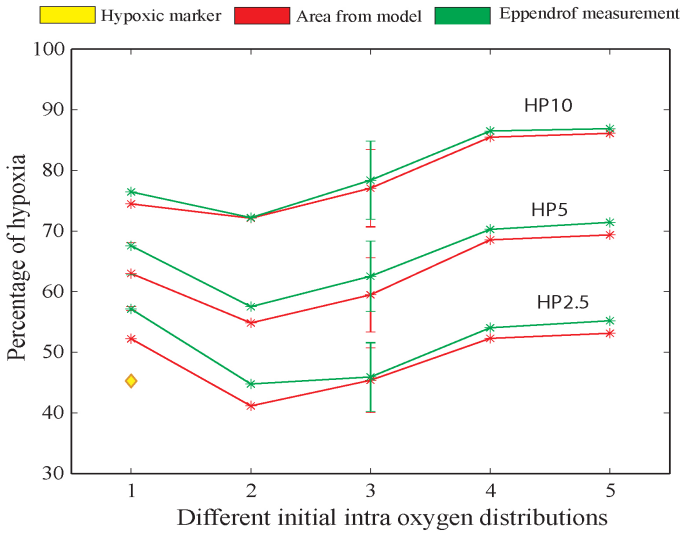


Figure 6.9: Changes in hypoxic proportions due to the variations in initial intra oxygen distributions (Here, the X- axis represents the initial oxygen distribution: 1) zero everywhere, 2) uniformly distributed along the perfused vessels (100 mm Hg), 3) random perfusion with $O_2$=100 mm Hg along perfused vessels 4) randomly distributed (ranges from 0 to 100 mm Hg) along the perfused vessels and 5) random perfusion with random distribution of $O_2$ along the perfused vessels, see Table 6.3)

superimposed acute hypoxia, and/or 2) higher oxygen consumption than used in the simulations. Moreover, the samples (Sample 2, 3, 4 and 8) that underestimate hypoxic area have a relatively higher vascular area, as compared to the other four samples. This indicates the presence of acute hypoxia, which we might not be able to quantify using this present model.

### Intra-vascular Hypoxia

To study intra-vascular hypoxia, five different initial oxygen configurations are used to simulate the tumor hypoxia. They are; (a) zero everywhere, (b) uniformly high

Table 6.3: Initial $O_2$ along perfused vasculature

| Cases (X axis) | Initial $O_2$ along perfused vasculature | |
|---|---|---|
| | Initial Value | Spatial distribution |
| 1 | 0 mm Hg | Uniformly distributed |
| 2 | 100 mm Hg | Uniformly distributed |
| 3 | 0 or 100 mm Hg | Randomly distributed |
| 4 | 0 mm Hg$<O_2\leq$100 mm Hg | Randomly distributed |
| 5 | 0 mm Hg$\leq O_2\leq$100 mm Hg | Randomly distributed |

$pO_2$ along the perfused vessels (100 mm Hg), (c) randomly distributed (ranges from 0 to 100 mm Hg) along the perfused vessels. The effects of random perfusion is also included in estimating hypoxia by randomly closing the vessels in the cases (b) and (c) (see Table 6.3).

The change in hypoxic proportions (HP10, HP5 and HP2.5) due to the variations in oxygen concentration and intra-vascular distribution is shown in Figure 6.9. The results (Figure 6.9) show that these changes in the hypoxic proportions are within a comparable range with an overall error of 6.5 % . Thus, the model is (to some extent) robust, in that it does not produce large variations in the final distribution of hypoxia by varying the initial intra-vascular oxygen distribution. However, a sensitivity analysis of the parameters that denote the production or supply ($r$ ) and consumption ($\phi$ ) of oxygen concentration showed that the consumption as well as perfusion of oxygen plays a vital role in defining local tissue oxygenation as compared to the oxygen supply (thus justifying the invariant results of intra-vascular hypoxia), which is consistent with the results of Dewhirst *et al.* [38] (see Figures 6.10, 6.11 and 6.12). Furthermore, this is an inherent feature of the present

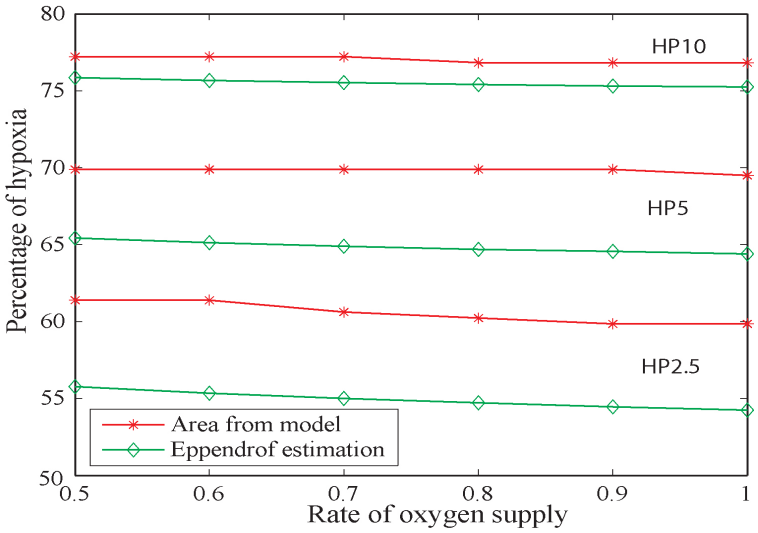


Figure 6.10: Change in hypoxia as a function of supply rates of oxygen

model which can be easily deduced mathematically through a steady state analysis of the equation governing oxygen concentration (Equation 6.1).

Under steady state conditions, oxygen concentration $K(x,t)$ can be written as,

$$\begin{aligned} & rm_p(x,t) - \eta K(x,t) - \phi c(x,t) = 0 \\ \implies \qquad & K(x,t) = \frac{rm_p(x,t) - \phi c(x,t)}{\eta} \end{aligned} \tag{6.4}$$

$$K(x,t) = \frac{\overbrace{rm_p(x,t)}^{\text{Delivery}} - \overbrace{\phi c(x,t)}^{\text{Consumption}}}{\eta} \tag{6.5}$$

Here, the consumption of oxygen is a function of the density of tumor cells while the delivery is a function of the density of perfused vasculature. Since the concentration and distribution of tumor cells is much higher than that of vascu-

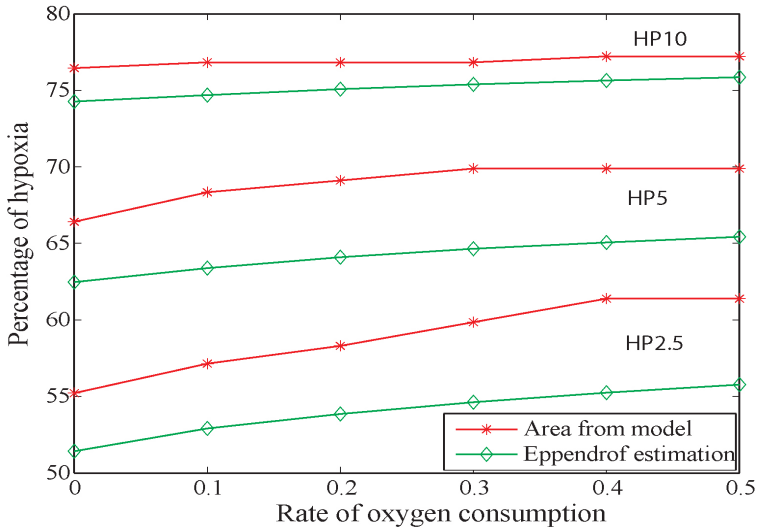


Figure 6.11: Change in hypoxia as a function of consumption rates of oxygen

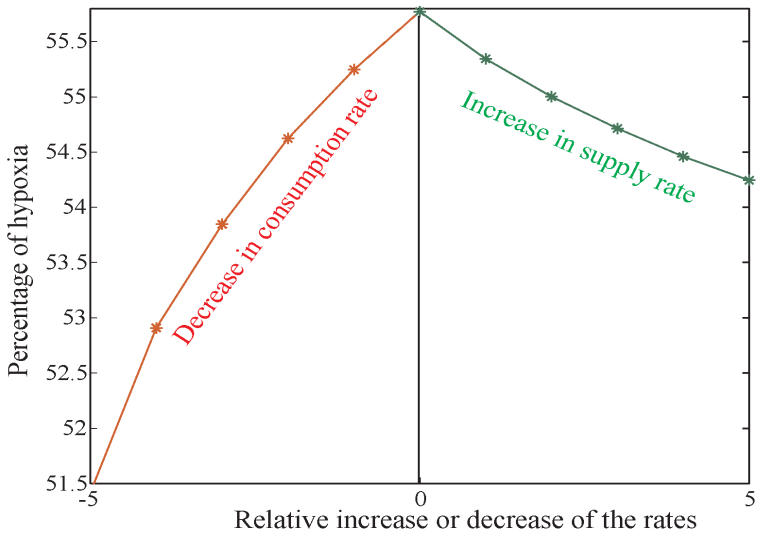


Figure 6.12: Change in hypoxia as a function of consumption and production rates of oxygen

lar distribution, the consumption rate plays a vital role in determining the tissue oxygenation status, as shown in Figure 6.12.

### Spatial Correlation of Hypoxic Area

The accuracy of the simulated hypoxic distribution is analyzed by calculating its spatial correlation with respect to the biomarker estimated hypoxia. Here, the spatial correlations are obtained by comparing the pixel by pixel values of the original binary images of hypoxia with the binary images of simulated hypoxic area (see Figure 6.13). The results given in Table 6.4 show that the model gives a satisfactory prediction of the spatial distribution of hypoxia since the correlation factor lies within the rage of 75 to 85 %.

Figure 6.8 illustrates model-obtained hypoxia estimates with the HP5 threshold for eight different tumor cross sections, using three different methods of simulated needle electrode tracking (namely, the uniform, radial, and random methods, depicted in Figure 6.6). As can be seen from the graph, these three methods of needle tracking give similar results and all are in good agreement with the simulated estimates of hypoxia found by calculating the percentage of the total area that is hypoxic. This supports the general opinion that polarographic electrodes give reasonable estimates of tumor oxygen status, and in fact, many researchers consider this to be the "gold standard" method for characterizing hypoxia in human tumors [75, 89]. However, it should be noted that these simulated needle electrode measurements are not subject to instrumental error, which is inherent in practice.

Table 6.4: Spatial correlations of hypoxic area

| Sample | HP 2.5 | HP 5 | HP 10 |
|---|---|---|---|
| Sample 1 | 77.6738 | 73.8076 | 68.3374 |
| Sample 2 | 81.1242 | 79.7579 | 74.8348 |
| Sample 3 | 80.701 | 83.1489 | 81.847 |
| Sample 4 | 87.6884 | 85.6093 | 78.3471 |
| Sample 5 | 73.3323 | 71.2458 | 68.0627 |
| Sample 6 | 80.498 | 74.8546 | 66.3771 |
| Sample 7 | 75.8521 | 71.6368 | 65.637 |
| Sample 8 | 76.2209 | 73.0056 | 66.1667 |

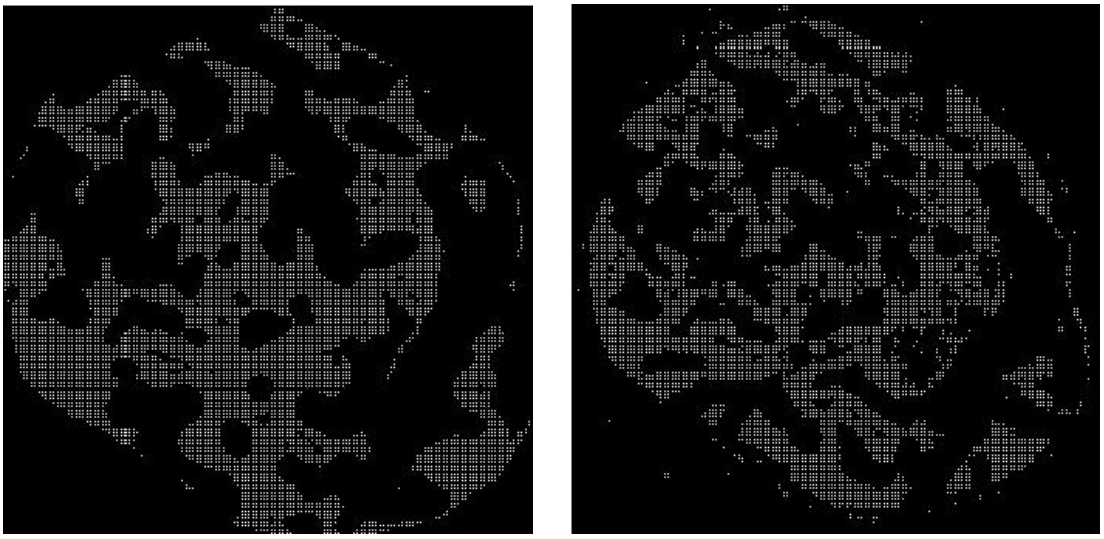

(a) Simulated hypoxia

(b) Original hypoxia

Figure 6.13: Spatial correlation of hypoxic area at HP 2.5 level

## 6.4 Statistical Analysis - Analysis of Variance

The total variance in sampling the oxygenation status is the combined effect of within tumor variance and between tumor variance. While the difference in the tumor samples (patients) contributes to the between tumor variance (a more heterogenous sample may result in more variation in group means), the difference in the location of the probe and hence, the measurements determine the variations within each tumor sample. Measurement of tumor $pO_2$ is considered to be a predictive outcome assay only when the within-tumor $pO_2$ variability is smaller than the variability among different tumors [15]. This variability is usually analyzed using a statistical method known as "analysis of variance (ANOVA)" (or variance components analysis) and this can be studied with respect to the number of needle tracks or various hypoxia estimation techniques. Since the differences between three different needle tracking approaches are not clearly evident from the above results (Figure 6.8), a variance components analysis (ANOVA) is performed here to compute the within- and between- tumor variability of needle electrode measurements.

Similar analysis comparing the variability of different oxygen measurements have been carried out in numerous experimental studies [14, 15, 142, 81]. One may use this kind of analysis when the assumption that the error terms are normally distributed holds; hence, before using this method to estimate the variances, the simulated data was analyzed to confirm that the errors approximately follow a normal distribution (Figure 6.14). The variances were then calculated using statistical software (MATLAB/SAS), and variability expressed in terms of percentage of total variance.

Here, this statistical analysis is used with two purposes in mind. Firstly, to

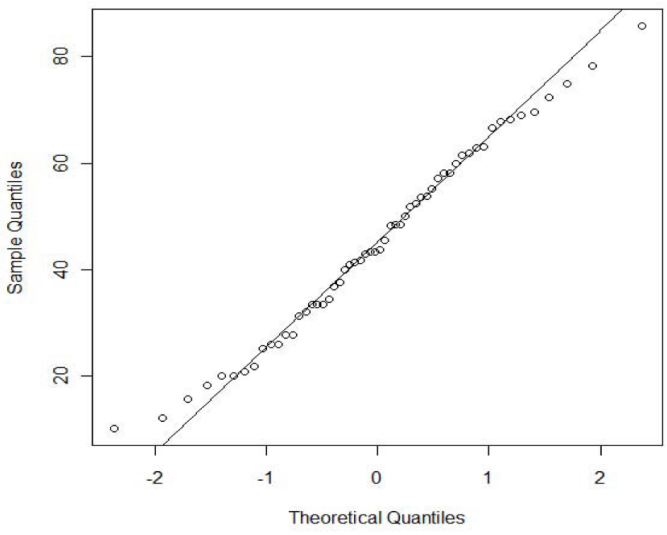


Figure 6.14: An example of QQ plot through which the normality of the data is analyzed

consider the fraction of within-tumor variance (relative to total variance) associated with each additional needle needle tracks in an effort to predict the optimum number of tracks required for satisfactory estimation. This is done by computing the ratio of within tumor variance over the total variance for each reading method (uniform, random and radial) [142] and is repeated for each additional track to compare the effects of the number of tracks on simulated $pO_2$ estimates. Secondly, to determine the best tracking pattern by considering the fraction of variability between two different estimation methods of hypoxia (simulated percentage hypoxic area and needle electrode measurements) among the tumor samples (relative to total variance). Note that, here, the simulated hypoxic area estimate is assumed to give an accurate description of hypoxic status since it gives an exact area under a certain threshold.

$$\underset{\text{Needle measurements}}{\text{Percentage of total variance}} = \frac{\text{Var(Within tumor)}}{\text{Var(Between tumor) +Var (Within tumor)}} 100$$

$$\underset{\text{Estimation methods}}{\text{Percentage of total variance}} = \frac{\text{Var(Between methods)}}{\text{Var(Between tumor) +Var (Between methods)}} 100$$

### 6.4.1 Needle Electrode Measurements -An Optimum Strategy

The variance analysis (Figure 6.15a) shows that the percentage of total variance due to the variance within a tumor is small for the random approach compared to radial and uniform approaches, whereas the uniform method of tracking has the maximum contribution of within variance to the total variance. However, this analysis may not necessarily permit one to conclude that the random approach is better than the other methods for estimating hypoxia, but rather may just be representative of the fact that this tracking method produces less spatial variation among electrode tracks. Moreover, this minimal variation in the case of the random approach is mainly due to the fact that the readings represent the average of a large number of realizations. The differences among the three different needle tracking approaches are further studied with variance analysis by calculating the percentage of total variance (between estimation methods plus between tumor sections) due to the variations between two different estimation methods (i.e. by finding the hypoxic area and through the needle electrode method). This is repeated for all three sample electrode tracking approaches and the results are shown in Figure 6.15b.

It is clear from Figure 6.15b that the contribution of variations between two different methods of quantifying hypoxia (specifically, the area approach and electrode

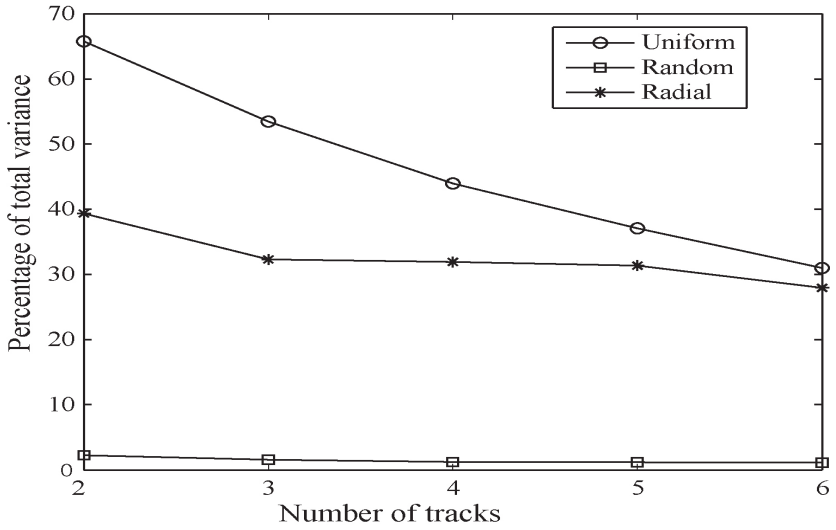


(a) The percentage of total variance due to within tumor variance, as a function of number of tracks

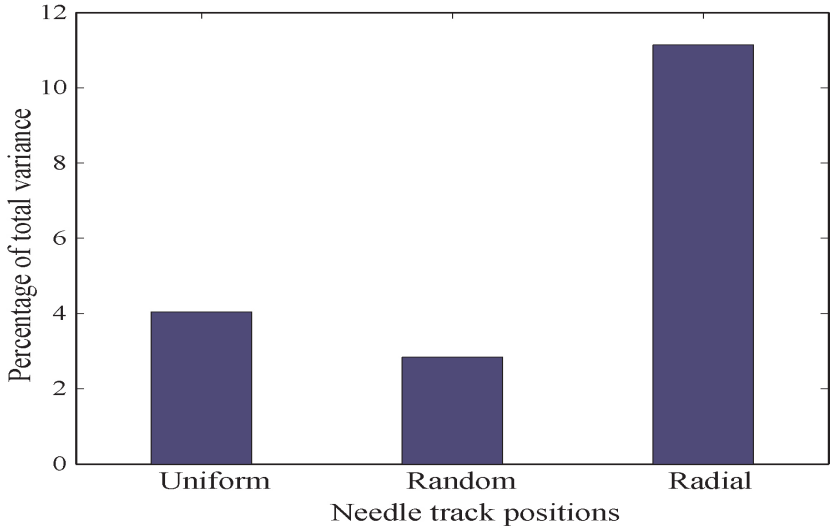


(b) The percentage of total variance due to the variance between two methods of hypoxia estimation for three different electrode measurements approaches

Figure 6.15: The variance analysis of electrode measurements

sampling method) to the total percentage of variations is much higher in the case of the radial method than for other tracking strategies. This implies that the radial method of electrode sampling is less accurate in sampling hypoxia than the other two approaches even though it has only small variations in within-tumor measurements (Figure 6.15b). This may be due to the manner in which the needle tracks are selected in the radial position: here, it is assumed that the tumor is accessible only from one side of the sample (as would likely be the case *in situ*), reaching the whole tumor (Figure 6.6c), and so all six tracks are situated between the 10 o'clock and 2 o'clock positions. This dictates that the needle tracks be close to each other, resulting in a smaller effective sampling area which in turn makes the variations within the tumor smaller and variation between the estimation methods higher. To verify this inference, another theoretical tracking approach has been introduced, for which it is assumed that the tumor is accessible from all the o'clock directions (Figure 6.6d), from 9 to 3 o'clock positions, which is named as radial (full circle), and compared this against the above results of the radial approach (Figure 6.16). It can be seen from the figure that when the sampling area is increased by spreading the tracks across a greater proportion of the 'circle', the percentage of total variance due to the variance of within-tumor measurements is also increased while the contribution of between-methods variance to the percentage of total variance decreased - although it did not decrease to a value as low as that for the uniform approach. Hence, it might be reasonable to conclude that a uniform spacing of electrode tracks gives a good sampling of the hypoxic proportion of the tumor cross-section compared to the other methods considered.

The variance analysis of needle electrode measurements (Figure 6.15a) also shows that the percentage of total variance due to within-tumor variance is decreased with an increase in the number of needle tracks and that this decrease is

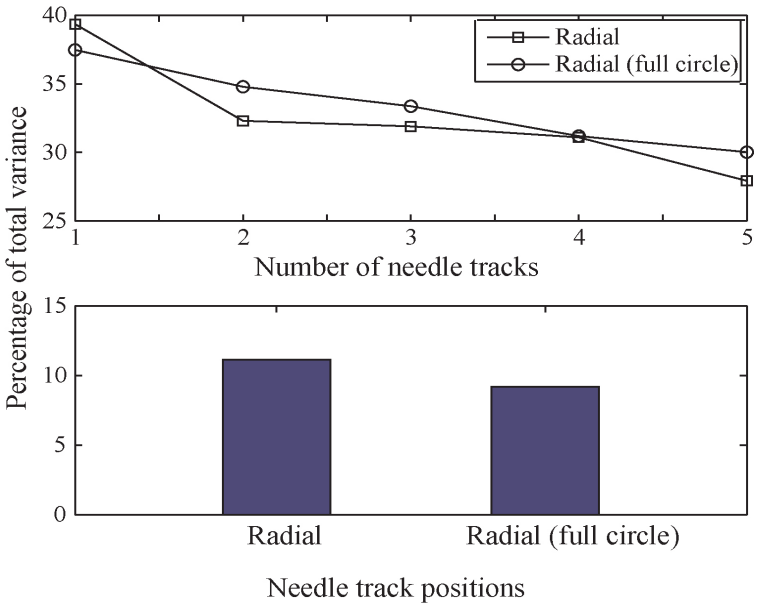


Figure 6.16: Variance comparison between two different types of radial approaches

minimal when the number of tracks is increased from four to five. Thus, the (minor) statistical benefits of increasing the number of tracks beyond this point are likely to be offset by the disadvantages of increased invasiveness. This indeed brings us to the same conclusion rached by Wong *et al.* [142] for the case of cervical cancers – with polarographic measurement data, the authors determined that "five measurements with 20-30 measurements per track is optimal to sample a cervix cancer to obtain a reliable and reproducible oxygenation status of the tumor"[142].

## 6.5 Effect of Hypoxia on Radiation Response

The oxygenation status of a tumor is generally considered to be an important intrinsic factor in determining radiation response, where viable hypoxic cells are

more resistant to radiation than well-oxygenated cancer cells [120]. It has been observed that the hypoxia usually acts as a dose limiting factor in the case of radiation therapy, requiring a higher radiation dose to obtain the same radiation damage as that of a well oxygenated tumor. In a tumor, spatial distribution of the vasculature, as well as the diffusion and consumption process make the oxygen distribution very heterogeneous (spatially and temporally) in nature, resulting in a wide range of radiation sensitivities. Hence, the hypoxia-dependent limitations of radiotherapy necessitate consideration of the spatial distribution of hypoxia within a tumor in order to estimate cancer cell survival fraction due to irradiation. Here, this effect of heterogenous oxygen distribution is analyzed using a modified linear quadratic model (MLQ) by considering the tissue specific hypoxia, simulated and quantified in previous sections (by calculating the percentage of area).

### 6.5.1 Mathematical Model

As explained in the introductory chapter, the linear quadratic (LQ) model is the most commonly used approach for studying the survival response of tumor cells to radiotherapy and the concomitant clinical results [122]. In the LQ model, the survival fraction of cells after a single radiation dose of $D$ (Gy) is given by,

$$S = \exp\left(-\alpha D - \beta D^2\right), \tag{6.6}$$

where $\alpha$ and $\beta$ are the radiosensitivity parameters chosen from Titz and Jeraj [124]. This choice of parameters (Table 6.5) gives a survival fraction of 48% at a dose $D = 2$ Gy, under well-oxygenated (normoxic) conditions. However, this radiosensitivity may vary based on the oxygenation status of the cell, in which hypoxic cells are considered to be more resistant to radiation [120]. This effect of

various oxygen levels on the radiosensitivity can be quantified in a LQ model using the concept of "oxygen enhancement ratio ($OER$)" or "oxygen modification factor ($OMF$)" [3, 145, 34, 124], defined as,

$$\begin{aligned} OMF &= \frac{1}{OER_m} OER(pO_2) \\ &= \frac{1}{OER_m} \left[ \frac{(OER_m pO_2(x) + K_m)}{(pO_2(x) + K_m)} \right], \end{aligned} \tag{6.7}$$

where $pO_2(x)$ is the oxygen concentration at position $x$, $OER_m$ is the maximum value under well-oxygenated conditions and $K_m$ is the $pO_2$ at which half maximum ratio is achieved) [124] (see Table 6.5 for parameter values). Consequently, the modified LQ (MLQ) model that incorporates the oxygenation effects can be written as,

$$S_{ox} = \exp\left(-\alpha \cdot OMF \cdot D - \beta (OMF \cdot D)^2\right). \tag{6.8}$$

In general, the $OER$ can be a function of radiation dose, and in fact, there is experimental evidence indicating that maximal oxygen enhancement varies in the range 2.5 to 3 with differences in radiation dosage [145, 34]. This can be simply included in the MLQ model by considering different $OER$s for the radiosensitivity parameters $\alpha$ and $\beta$, i.e. $OER_\alpha$ and $OER_\beta$. However, since a normalized $OER$ ($OMF$) is considered here, the introduction of these separate functions will not produce a significant difference in the final survival fraction. Thus, an assumption of $OER_\alpha = OER_\beta$ is made in the current simulations (Please note that the introduction of $OER_\alpha$ and $OER_\beta$ will not make any significant changes in the final result).

Here, this MLQ model is used to study the effects of heterogeneous distribution of oxygen on radiotherapy outcome. To this end, the cell survival fraction is calculated while varying the dosage D for different oxygen profiles. The comparisons are made for six different cases, assuming: (a) the entire tumor is normoxic ($pO_2$=60

Table 6.5: Numerical values of the parameters used MLQ model [124]

| Parameters | Symbol | Value |
|---|---|---|
| Radiosensitivity | $\alpha$ ($Gy^{-1}$) | 0.3 |
| Radiosensitivity | $\beta$ ($Gy^{-2}$) | 0.03 |
| $pO_2$ at which half maximum ratio is achieved | $K_m$ (mm Hg) | 3 |
| Maximum $OER$ | $OER_m$ | 3 |

mm Hg), (b) the entire tumor is anoxic ($pO_2$=0 mm Hg), (c) the entire tumor is moderately hypoxic ($pO_2$=5 mm Hg), (d) a twofold profile, either hypoxic or normoxic at each grid point ($pO_2 \leq$5 mm Hg and $pO_2 >$5 mm Hg), (e) a histogram of oxygen distribution with a bin width of 5 mm Hg ($5(i-1) \leq pO_2 \leq 5i$, i=1, 2, 3, ..., 20), see Figure 6.17, and (f) fully heterogeneous oxygen distribution (the value of $pO_2$ at each grid point). For the cases (d) to (f), where the oxygen distribution is not uniform, the final survival fraction is calculated by taking the weighted average of the survival fractions at each compartment or grid points [34],

$$SF_{ox} = \frac{\Sigma_{i,j} w_{i,j} S_{ox}(pO_2(i,j))}{\Sigma_{i,j} w_{i,j}}. \tag{6.9}$$

Although the focus of this study is to analyze the effects of heterogenous oxygen concentration on the total radiation dosage, various fractionation schemes as well as temporal changes in hypoxia can be also studied by introducing this $OMF$ factor into the generalized linear quadratic model (see Chapter 5).

### 6.5.2 Radiation Response

Here, the survival fractions are calculated using the MLQ model (Equation 6.9) by considering various profiles of oxygen distributions as given in the above section.

Figure 6.17 shows the results of the MLQ model (iii), the oxygenation profiles as histograms of width 5 mm Hg (i), and the oxygen modification factor ($OMR$) as a function of the oxygen concentration (ii). These results indicate that the oxygen concentration significantly affects the $OER$; this is due to the fact that $OMF$ increases rapidly to its normalized value (one) as the partial pressure of oxygen is increased from zero to about 30 mm Hg (most of the cells in the tumor are under 30 mm Hg). Hence, considering the sensitivity of the heterogeneous distribution of oxygen at each grid point (or each cell), a much higher dosage is required to get the same survival fraction of cells compared to the other four cases (Figure 6.17-iii). One should note that this level of dosage is even higher than the case of a fully hypoxic tumor. However, this may be due to the assumption that the fully hypoxic tumor has a uniform oxygen distribution of 5 mm Hg (moderate hypoxia), while for the heterogeneous case most of the cells have an oxygen concentration less than 5 mm Hg. Furthermore, this is clear from the figure where the dosage level curve for a heterogeneous distribution is almost coincident with the curve for complete anoxia (but lying slightly below). The reason for this similarity is due to the radio-resistance of severe hypoxic cells (cells with less than 5 mm Hg), which is theoretically quantified using the OMF curve (Figure 4 b). This OMF curve increases to its peak value with a relatively small increase in oxygen concentration (0-10 mm Hg) and hence cells with severe hypoxia give rise to similar survival effects as that of anoxic cells. These results indicate the importance of the effects of the oxygenation status in estimating the radiation response of the tumor cells.

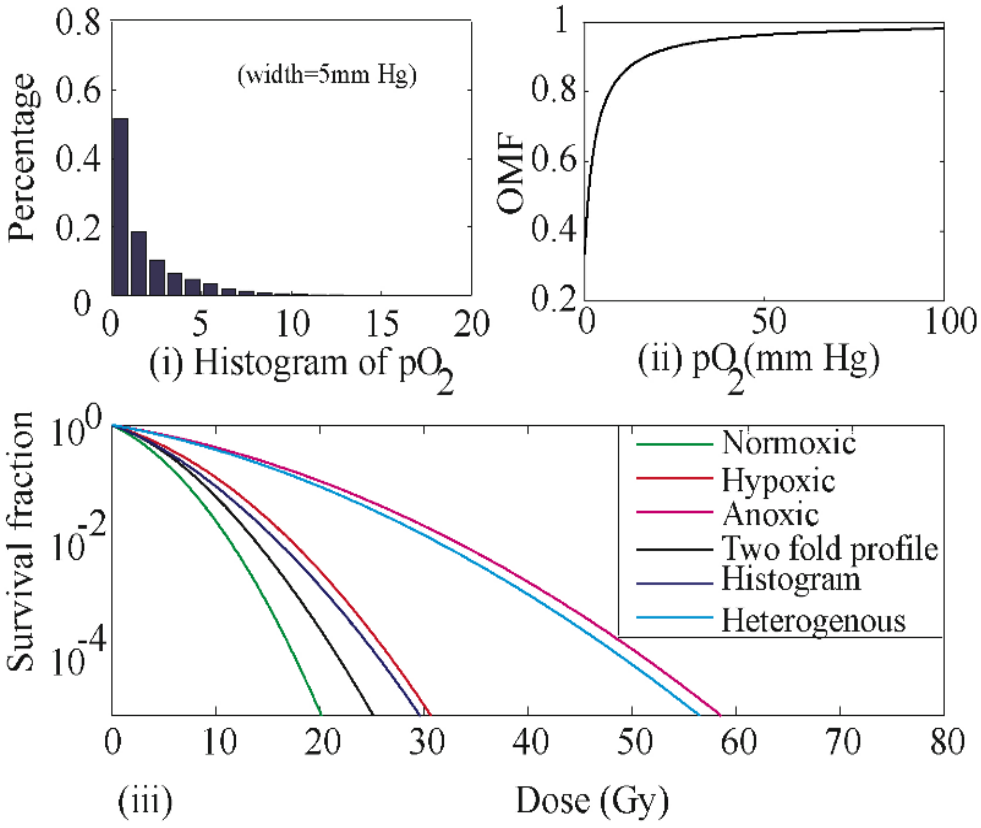


Figure 6.17: (a) Simulated oxygen distribution as histograms of width 5 mm Hg (for a representative case), (b) oxygen modification factor (OMR) as a function of the oxygen concentration, and (c) Survival fraction for different cases of oxygen profiles considering the oxygen distribution of a representative case

Moreover, the accuracy of this estimation is closely dependent on the detailed quantification of oxygen distribution inside the tumor rather than classifying it into hypoxic or non-hypoxic compartments.

## 6.6 Short Summary

In this chapter, we discuss a simple diffusion model which can satisfactorily estimate the oxygenation maps of a heterogeneous tumor with a given vascular network. Using this mathematical model it was shown that an estimate can be made of average tumor hypoxia which appears to be less sensitive to the characteristics of the vascular network and initial intravascular $pO_2$ values as compared to the variations in O2 consumption. Thus this approach can be used to quantify average tumor hypoxia knowing only the distribution of tumor vessels. With the help of variance components analysis, it was found that the polarographic electrode measurements accurately quantify the oxygenation status of the tumor microenvironment. The studies show that five uniformly distributed equidistant, measurement tracks with 20-30 measurements per track give the optimum balance between accuracy and invasiveness. The radiation response under various oxygenation conditions has also been analyzed using a simple model for the radiation effect and the results show that, consideration of the heterogeneous distribution of oxygen plays an important role in the accurate prescription of radiation dosage. This type of theoretical study may be used to provide an alternative method of estimating hypoxia distribution in solid tumors which may help in the prediction of therapeutic responses in order to avoid over and under treatment, and help in the design of optimal, patient-specific and accurate invasive estimation methods.

# Chapter 7

# Interstitial Fluid Pressure: Effects of Heterogenous Vascular Distributions

## 7.1 Introduction

The success of cancer detection and treatments highly depends on the effective delivery of pharmacological or immunological substances into the tumor. Normally, these substances are delivered through the vascular system and reach the tumor tissue by penetrating through the vessel wall, which occurs by both convection and diffusion. They then move through the tumor interstitial space to the target site, also driven by convection and diffusion [53]. However, in the case of solid tumors, it has been observed that this delivery of drug molecules (or even nutrients) is limited by several pathophysiological and microenvironmental barriers [53]. As we have seen in the Introduction, one of the most important microenvironmental factors

that affects drug delivery within solid tumors is elevated interstitial fluid pressure (IFP) [53], which arises as a result of abnormal tumor vasculature and lack of functional lymphatics. In previous works, it has been shown that in a uniformly perfused tumor, the IFP is uniformly elevated throughout the tumor except near the boundary, where the pressure drops down to that of the normal tissue, and that this hinders the delivery therapeutic drug molecules [53].

This chapter aims to analyze the effects of a heterogenous vascular distribution on tumor IFP and IFV (interstitial fluid velocity) profiles by using the vascular distributions obtained from stained biopsy samples. It is evident that the spatial and temporal evolution of tumor vasculature also affect various transport properties of the tissue, resulting in an increase or decrease in tumor IFP [52]. Here, we also seek to include the dynamics of tumor vasculature and its effects on the tumor IFP, both with and without antiangiogenic therapy using a simple mathematical framework.

## 7.2 Modeling Interstitial Fluid Pressure and Velocity

Interstitial fluid pressure is found to be elevated in most solid tumors. This elevated IFP is usually a result of the abnormal structure and function of tumor blood vessels and lymphatic system. The elevated IFP serves as barrier to the delivery of anti-cancer drugs [54], and therefore is a significant impediment to the successful treatment of the tumor. Due to its clinical importance and also to gain insights into the mechanism and implications of elevated IFP, researchers like Jain and Baxter [53] have developed mathematical models to simulate the IFP as well as the fluid

and macromolecular transport within solid tumors.

The mathematical model proposed by Jain and Baxter [53] studies the variation of IFP with respect to different transport properties of the vessel wall and interstitium. The movement of fluid or solute within any tissue is usually composed of two main components – the transport through the vessel wall, and the flow within the interstitial matrix. The movement across the vessel wall is governed by Starling's principle, which states that the forces responsible for filtration or absorption of fluid are the hydrostatic and osmotic pressure gradients between the capillary and interstitial space. Mathematically, we write an equation for the volume flux, which is given by

$$J_v = L_p S \left( p_c - p_i - \sigma_T (\pi_c - \pi_i) \right), \tag{7.1}$$

where $L_p$ is the hydraulic conductivity of the capillary wall, $S$ is the surface area of the vessel, $p_c$ and $p_i$ are capillary and interstitial hydrostatic pressures, $\pi_c$ and $\pi_i$ are capillary and interstitial osmotic pressures and $\sigma_T$ is the osmotic reflection coefficient of plasma protein. In tumor tissues, it is usually assumed that the osmotic pressure of capillary and interstitium are almost equal (i.e. $\pi_c \approx \pi_i$) [54] and hence the volume flux can be rewritten as a function of capillary pressure (or microvascular pressure (MVP)) as simply

$$J_v = L_p S \left( p_c - p_i \right). \tag{7.2}$$

In normal tissues the excess fluid that filter through the capillary wall is reabsorbed by the lymphatic system. However, in tumors the lymphatics are structurally and functionally degraded or sometimes even absent [53] and hence the excess fluid that leaks out of the abnormal blood vessels remains trapped within the tumor. This fluid buildup within the tumor eventually increases the interstitial

fluid pressure until it reaches an equilibrium with the capillary pressure. Now, assuming flow through the interstitial matrix can be treated as a flow through porous media, the interstitial fluid velocity (IFV) can be defined using Darcy's law. Darcy's law states that the fluid velocity $u_i$ is proportional to the applied pressure gradient and hence IFV can be written as:

$$u_i = -K\nabla p_i, \tag{7.3}$$

where $K$ is the hydraulic conductivity of the interstitial matrix. Since Starling's law gives a source of fluid, and there is no sink due to the lack of lymphatics, conservation of mass takes the following form:

$$\nabla \cdot u_i = \frac{J_v}{V}, \tag{7.4}$$

where $V$ is the volume of the tumor. Substituting Equation 7.3 and Equation 7.2 into Equation 7.4 leads to:

$$\nabla^2 p_i = \frac{L_p S}{KV}(p_i - p_c). \tag{7.5}$$

Using the previous rescaling parameters (Section 7.1.2) $x = L\tilde{x}$ ( for example, $L = R$ is the radius of the tumor) and $p_i = p_c\tilde{p}_i$, the above equation for IFP can be rewritten in a non-dimensionalized form as:

$$\nabla^2 \tilde{p}_i = \alpha_m^2(\tilde{p}_i - 1), \tag{7.6}$$

where $\alpha_m = L\sqrt{\frac{L_p S}{KV}}$, represents the ratio of vascular permeability to the interstitial permeability or, in other words, it is the ratio of rate of fluid movement across the vessel wall to the rate of flow through the interstitial matrix. This equation for pressure is then solved with a zero boundary condition at the periphery using the parameter values given in Table 7.1.

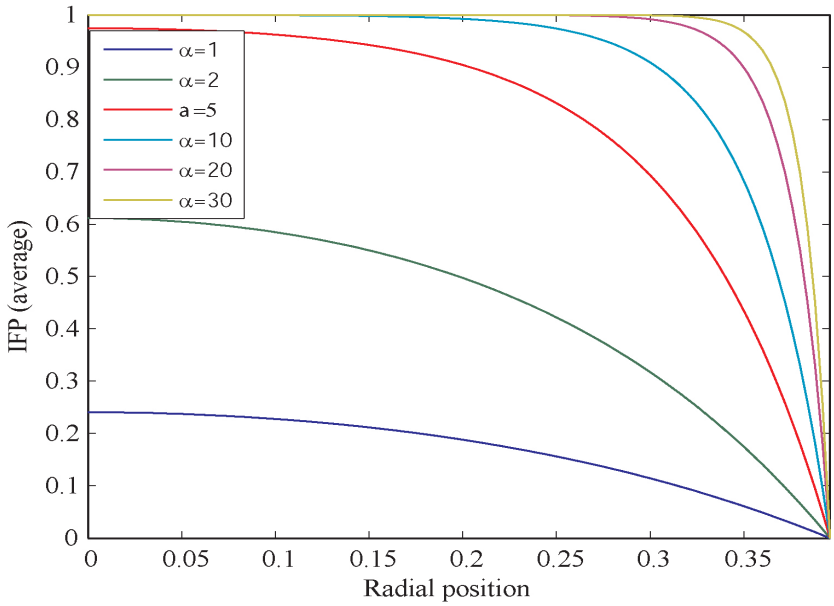


(a) Radial profile of interstitial fluid pressure

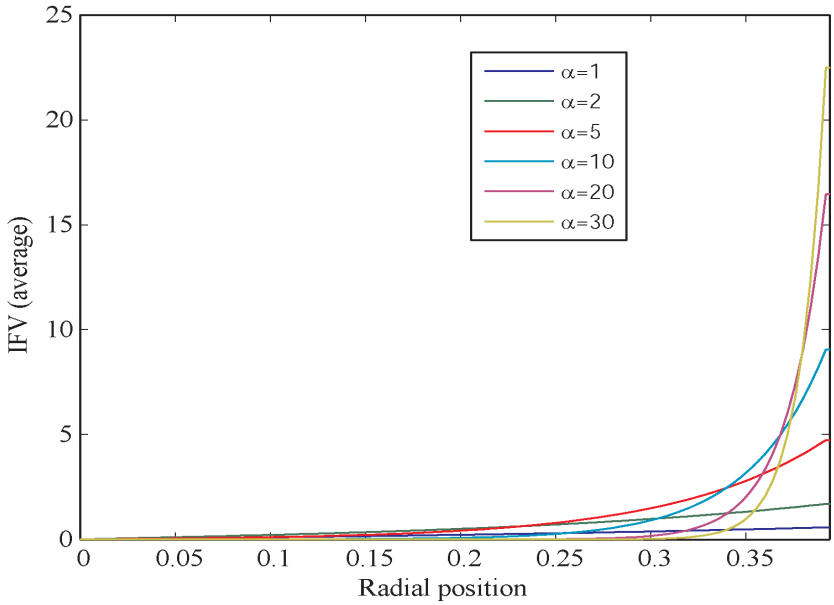


(b) Radial profile of interstitial fluid velocity

Figure 7.1: Radial profiles of interstitial fluid pressure and interstitial fluid velocity

Table 7.1: Parameter values for the model

| Symbol | Value | Reference |
|---|---|---|
| $R$ (cm) | 0.4 | see text |
| $L_p$ (cm $s^{-1}mmHg^{-1}$) | $1.86\times10^{-6}$ | [54] |
| $K$(cm$^2$ $s^{-1}mmHg^{-1}$) | $2.5\times10^{-7}$ | [54] |
| $S/V$ (cm$^{-1}$) | 200 | [54] |
| MVP ($p_c$) (mm Hg) | 5 - 34 | [54] |
| $\sigma_T$ | 0.82 | [9] |
| $\sigma$ | 0.91 | [9] |
| $P$(cm s$^{-1}$) | $5.73\times10^{-7}$ | [9] |
| $D_L$ (cm$^2$s) | $1.3\times10^{-8}$ | [9] |

Figure 7.1 shows the radial profiles of IFP and IFV for different values of $\alpha_m$ in the case of a homogenous tumor. The ratio $\alpha_m$ may increase (decrease) due to a decrease (increase) in hydraulic conductivity of the interstitial matrix and/or an increase (decrease) in tumor radius, hydraulic conductivity of the vessel wall or exchange surface area per unit volume. It can be seen that for low values of $\alpha_m$, the IFP profiles are flat due to the low filtration through the vessel walls. As the values of $\alpha_m$ increase, the IFP within the tumor increases, resulting in a sudden drop near the boundary. Consequently, IFV remains low and uniform for small values of $\alpha_m$ and increases to a higher value near the boundary of the tumor [53], leading to an outward convective flow which acts as a barrier to drug delivery.

## 7.3 Effects of Vascular Distribution on IFP and IFV

Here, we consider the effects of a heterogenous vascular distribution on the profiles of tumor IFP and IFV. To obtain the heterogenous vasculature, we have used the biopsy images of glioma xenografts stained for perfused vasculature which were earlier (Chapter 6) used to study the spatial distribution of hypoxia [92]. To include this heterogeneity into the IFP profiles, the equation for the pressure profile (Equation 7.6) is further modified by assuming that the fluid filtration occurs only at vascular regions. Hence, the modified equation can be written as

$$\nabla^2 \tilde{p_i} = M(x)\alpha_m^2(\tilde{p_i} - 1), \tag{7.7}$$

where $M(x)$ represents the spatial distribution of vasculature obtained from the stained images. After the discretization, the matrix $M$ is composed of two values, namely 1 and 0, denoting the presence and absence of the vasculature, respectively [146].

Figure 7.2 shows the distribution of IFP and IFV for three different heterogenous vascular distributions. It can be clearly seen from the figure that the spatial distribution of vasculature plays a vital role in the shape and values of IFP and IFV profiles making them heterogenous in nature as well. As one observes, the areas with high vascular density contribute more to the pressure profile and even determine the shape of the profile. This difference in the IFP and IFV profiles due to different vascular distributions is illustrated in Figure 7.3, which shows the average radial profiles for three different samples. On the other hand, the variation of $\alpha_m$, the ratio of vascular permeability to the interstitial permeability, gives a similar trend as that of the homogenous case and is shown in Figure 7.4 for Sample 1. The

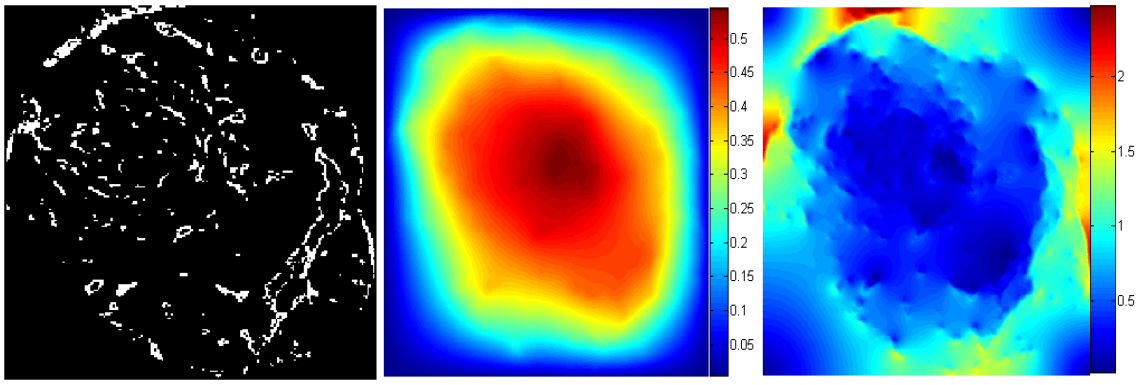


(a) Vessel distribution (b) Pressure profile (c) Velocity profile

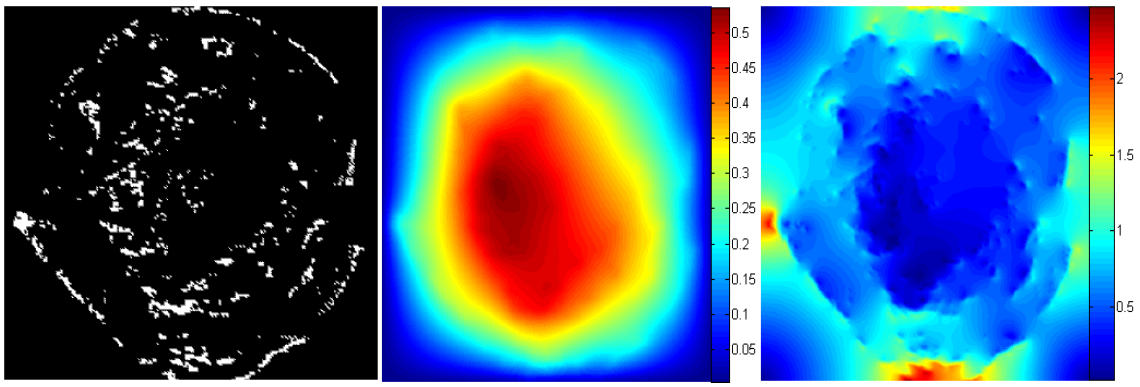


(d) Vessel distribution (e) Pressure profile (f) Velocity profile

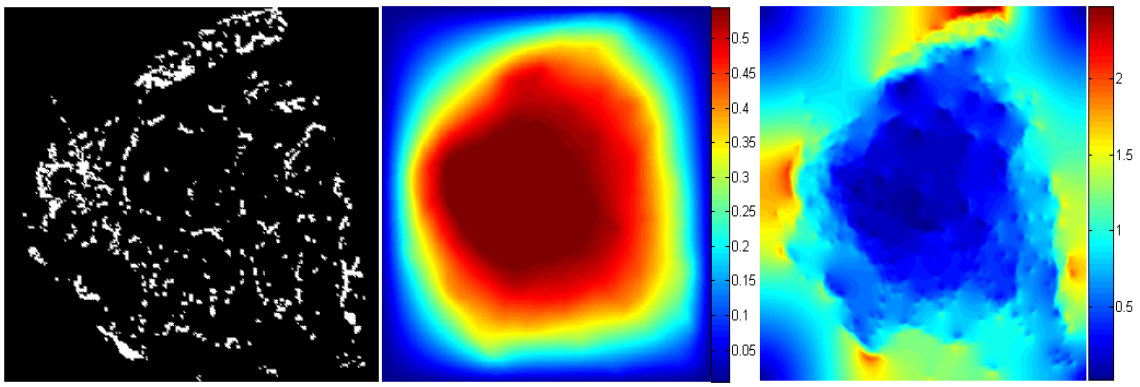


(g) Vessel distribution (h) Pressure profile (i) Velocity profile

Figure 7.2: Profiles of IFP and IFV with heterogenous vasculature (samples 1-3)

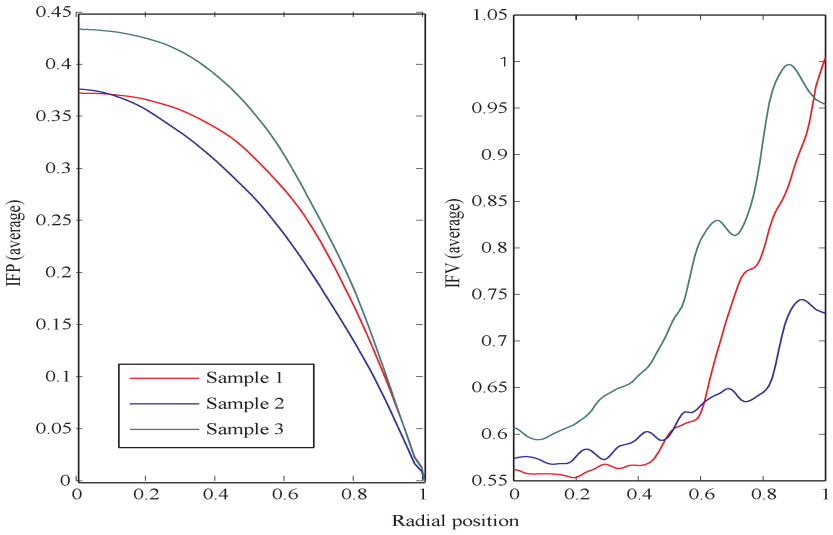


Figure 7.3: IFP and IFV profiles for various vascular distributions (Samples 1-3)

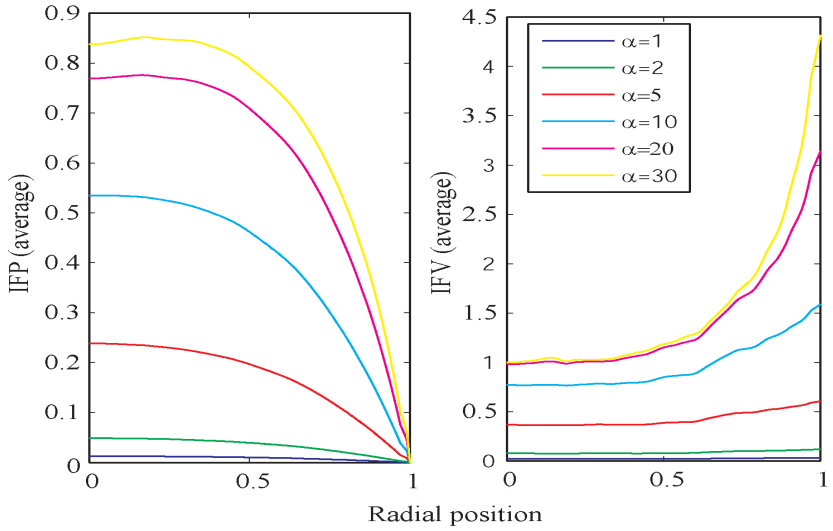


Figure 7.4: IFP and IFV profiles as a function of $\alpha_m$

differences in the magnitude of predicted IFP and IFV from the previous models [53] as well as the above homogenous case is mainly due to the consideration of regions with low vascular density and hence low filtration, which is often the case for tumors seen in patents and *in vivo* experiments.

Evidently, it is clear from the above results that the heterogenous nature of tumor vasculature changes the IFP and IFV profiles, both qualitatively and quantitatively. At the same time, these changes in IFP also affect the transport properties of the tumor which in turn will affect the delivery of drugs and other pharmacological molecules into the tumor, which will be discussed in future works.

## 7.4 Modeling the Dynamics of Tumor Vasculature

In reality, the heterogenous nature of tumor vasculature significantly influences tumor IFP, IFV and the distribution of drugs within the tumor. This is mainly due to the abnormal tumor vascular distribution, which results in the spatial and temporal dependence of various transport parameters. Mathematically, the influence of tumor vessels is usually characterized using a single parameter $\alpha_m$. In the above steady state analysis of biopsy data, we have incorporated this spatial dependence of the parameter $\alpha_m$ by assuming it to be nonzero only in the areas of blood vessels. However, it might be more meaningful if it also depends on the nature of the blood vessels as it is known that tumor vessels are generally structurally and functionally abnormal thus making $\alpha_m$ functionally heterogenous [54]. Unfortunately, at this moment we do not have any functional information of tumor blood vessels to study the variation of these parameters and their effects on IFP or IFV. Nevertheless, an

alternative approach to analyze this concept is through a comprehensive mathematical model, which could accommodate evolution of tumor vasculature and their role in changing tumor IFP. One of such mathematical model is proposed here in this section.

Several models have appeared in the literature to describe the process of angiogenesis and the distribution of vascular networks [4, 68, 22, 20]. Most of these models study the interactions among endothelial cells, cancer cells and the extracellular matrix through a set of partial differential equations. These interactions may be due to a direct relationship or through various tactic components such as chemotactic or haptotactic influences by angiogenic factors or fibronectin gradients and the extracellular matrix. Here, the vascular networks are modeled using a phenomenological model proposed by Kohandel *et al.* [59] and in accordance with the model, we assume that the tumor vessels grow in response to the pro-angiogenic cytokines secreted by the cancer cells under the influence of a changing tumor microenvironment.

In the coarse-grain model developed by Kohandel *et al.* [59], the heterogenous vascular structures are represented by islands of vascular and non vascular networks with specific values. Typically these values measure the degree of normality of blood vessels within the tissue. As observed experimentally, most of the tumor vessels are structurally and functionally abnormal resulting in spatially and temporally heterogenous networks with poor delivery of oxygen and other nutrients [52]. In the present model, the delivery capability of the blood vessels are also phenomenologically modeled through the values taken by the vessel structures. If we denote the average blood vessel distribution by $m(x,t)$, the governing equation

for local vessel density can be written as,

$$\frac{\partial m(x,t)}{\partial t} = D_m \nabla^2 m(x,t) + g(m), \tag{7.8}$$

where $D_m$ is the diffusion constant and $g(m)$ denotes the local vessel growth.

Following Kohandel *et al.* [59], $g(m)$ is chosen to be $g(m) = \alpha m + \beta m^2 + \gamma m^3$ with $\alpha = -I$, $\beta = 3I$ and $\gamma = -2I$; where $I$ is a positive constant. This set of values allows the above vessel Equation 7.8 to have two stable fixed points 0 and 1, representing the the islands of non-vascular and normal vascular structures, respectively. Here, the simulations are done taking a random initial configuration for vascular density with values ranging from 0 to 1. A detailed stability analysis of the vessel equation is given in Section 7.3.2.

### 7.4.1 Interaction with cancer cells

As previously discussed, the uncontrolled growth of cancer cells often requires a constant supply of oxygen and other nutrients. This is achieved through the up-regulation of tumor angiogenesis by an excess production of pro-angiogenic factors. There is also substantial evidence that the tumor vessels thus created have higher vascular density than in corresponding normal tissue [134]. In the model (Equation 7.8) by Kohandel *et al.* [59], this effect is incorporated through the tactic and direct interactions between tumor vessels and cancer cells. Consequently, equation 7.8 can be reformulated as,

$$\frac{\partial m(x,t)}{\partial t} = D_m \nabla^2 m + m(\alpha + \beta m + \gamma m^2) + \alpha_2 c(x,t) m + \beta_2 \nabla \cdot (m \nabla c(x,t)). \tag{7.9}$$

Here, $\alpha_2$ and $\beta_2$ are positive constants and $c(x,t)$ denotes the density of cancer cells. The third term on the right hand side represents upregulation of tumor

angiogenesis in response to the increasing demand of cancer cells and the last term denotes the directed movement of blood vessels. As a result of the increased tumor angiogenesis due to the increase in cancer cell density (third term), this reformulated vessel equation 7.9 has higher stable fixed points than the normal case, indicating an increase in tumor vascular density (details are given in the stability analysis section). Thus in the present model, the abnormal tumor vessels are distinguished from normal vessels using their density values.

The cancer cell density, $c(x,t)$ is governed by another reaction-diffusion equation given by,

$$\frac{\partial c(x,t)}{\partial t} = D_c \nabla^2 c + \rho c \left(1 - \frac{c}{c_{lim}}\right) + \alpha_1 c m(x,t) + \beta_1 \nabla \cdot (c \nabla m(x,t)), \qquad (7.10)$$

where $D_c$ is the diffusion constant for cell density, $\rho$ is the growth rate and $\alpha_1$ and $\beta_1$ are positive constants. Here, the second term represents the logistic growth dynamics (which have been discussed in detail in Chapter 3) and the third term represents the increased cell growth as a result of tumor angiogenesis. Finally, the fourth term in this equation represents the directed movements of tumor cells [59].

### 7.4.2 Stability Analysis

In the present coarse-grain model for vasculature (Equations 7.8– 7.10), the steady state values of $m$ generally denote the nature of blood vessels within the tissue. While the values of $m$ close to one indicate a normal blood vessel, less perfused, abnormal tumor vessels are usually denoted using much higher values ranging from 1.2 to 1.8 [59].

Consider the following dimensionless equations for the vascular distribution un-

| Symbol | $\tilde{\alpha_1}$ | $\tilde{\beta_1}$ | $\tilde{D_m}$ | $\tilde{\alpha}$ | $\tilde{\beta}$ | $\tilde{\gamma}$ | $\tilde{\alpha_2}$ | $\tilde{\beta_2}$ | $\tilde{A_i}$ |
|---|---|---|---|---|---|---|---|---|---|
| Value | 1.2 | 0.02 | 0.005 | -1 | 3 | -2 | 0.7 | 0.8 | 0.3 |

Table 7.2: Numerical values of the (nondimensionalized) parameters ($D_c = 0.035$ mm$^2$/day and $\rho = 0.16$ (1/day)) [59]

der steady state:

$$\begin{aligned} c\,(1-c) + \tilde{\alpha_1} c m(x,t) &= 0, \\ m(\tilde{\alpha} + \tilde{\beta} m + \tilde{\gamma} m^2) + \tilde{\alpha_2} c(x,t) m &= 0, \end{aligned} \tag{7.11}$$

which has a trivial fixed point $c^* = 0$ and the nontrivial fixed point

$$c^* = 1 + \tilde{\alpha_1} m, \tag{7.12}$$

which we associate with the tumor case. For this value of $c^*$, and setting $\tilde{\alpha} = -1$, $\tilde{\beta} = 3$ and $\tilde{\gamma} = -2$, we obtain a trivial fixed point $m^* = 0$ and following nontrivial fixed points,

$$m^* = \frac{(3 + \tilde{\alpha_1}\tilde{\alpha_2}) \pm \sqrt{8(\tilde{\alpha_2} - 1) + (3 + \tilde{\alpha_1}\tilde{\alpha_2})^2}}{4}. \tag{7.13}$$

For the parameter values $\tilde{\alpha_1} = 1.2$ and $\tilde{\alpha_2} = 0.7$ [59], this reduces to

$$m^* = 1.83, 0.08 \tag{7.14}$$

where the value 1.83 represent the case of a tumor.

### 7.4.3 Anti-angiogenic Therapy: Effects on IFP

We have already seen that the IFP is elevated in most solid tumors due to the presence of irregular vasculature and the absence of functional lymphatics [54].

This elevated IFP as well as the spatially and temporally heterogenous nature of tumor vasculature further reduce the successful delivery of oxygen and anti-cancer drugs, contributing to the failure of cancer therapies which results in the tumor cells developing a more aggressive phenotype. Recent preclinical evidence shows that antiangiogenic therapy can lower the tumor IFP by changing tumor vessel transport properties through the passive pruning of leaky vessels and active remodeling of the tumor vasculature [52]. It is also observed that these lower IFP will further increase the interstitial convection within the tumor, creating a window of opportunity for the better delivery of various anti-cancer drugs. The primary aim of this section is to study these dynamic changes in IFP after treatment with antiangiogenic therapy by using the above mathematical model.

**Modeling Antiangiogenic Therapy**

Although the delivery of antiangiogenic therapeutic agents occurs through a complex transport mechanism, for the purpose of the present study (to analyze the dynamics of IFP) we simply assume that at the time of treatment these agents are homogenously present within the tumor. As the antiangiogenic therapy destroys or remodels tumor blood vessels, its effects can be incorporated into the mathematical model by adding a term $-A(t)m(x,t)$ to the equation for evolution of blood vessels m(x,t), Equation 7.9 [59]. Mathematically, the addition of this term changes the stable fixed points of the system to a lower value. If this value is close to one, it denotes the presence of normal vasculature, however if it is close to zero (for stronger dosage), it indicates the disappearance blood vessels. The equation now reads:

$$\frac{\partial m(x,t)}{\partial t} = D_m \nabla^2 m + m(\alpha + \beta m + \gamma m^2) + \alpha_2 c(x,t) m + \beta_2 \nabla(m.\nabla c(x,t)) - A(t)m. \tag{7.15}$$

where $A(t) = \sum A_i f\left(\frac{t-t_i}{\tau_a}\right)$ is the temporal profile of the therapy with $\tau_a = 2$ days. To study the effects of antiangiogenic therapy, it is given as three doses with an interval of 2 days, starting on day six (when the radius reaches around 1 mm).

For computational convenience the system of equations governing the dynamics of tumor cell density, and the vascular distributions are nondimensionalized in the following manner. Time and space are rescaled as $t = \tilde{t}/\rho$ and $x = \sqrt{D_c/\rho}\tilde{x}$, respectively, and the cell density is rescaled as $c = c_{lim}\tilde{c}$ (note that $m$ is already a dimensionless variable which represents the average distribution of blood vessels). The system of equations after nondimensionalization is given below (after dropping tildes in $x$, $t$ and $c$).

$$\begin{aligned}
\frac{\partial c(x,t)}{\partial t} &= \nabla^2 c + c\,(1-c) + \tilde{\alpha_1} cm(x,t) + \tilde{\beta_1}\nabla\cdot(c\nabla m(x,t)), \qquad (7.16)\\
\frac{\partial m(x,t)}{\partial t} &= \tilde{D_m}\nabla^2 m + m(\tilde{\alpha} + \tilde{\beta} m + \tilde{\gamma} m^2) + \tilde{\alpha_2} c(x,t)m + \tilde{\beta_2}\nabla\cdot(m\nabla c(x,t)) - \tilde{A}(t)m,
\end{aligned}$$

where $\alpha_1$, $\alpha$, $\beta$, $\gamma$ and $A_i$ are scaled with $\rho$ (shown in tildes), $\beta_1$ and $D_m$ are scaled with $D_c$ and $\tilde{\beta_2} = \beta_2 c_{lim}/\rho$, $\tilde{\alpha_2} = \alpha_2 c_{lim}/\rho$ (once again we will drop the tildes in the subsequent steps for notational convenience).

Finally, the formulation of the model for system of equations (Equation 7.16) is completed be prescribing proper initial and boundary conditions. While simulation of the cell density equation is carried out using a Gaussian initial condition and a no-flux boundary condition, the equation for vascular density starts with a random initial configuration and a no-flux boundary condition. The parameters for this analysis are taken from Kohandel *et al.* [59] and are listed in Table 7.2.

### A Dynamic Model for Tumor IFP

In previous work [53, 54], it has been shown that the ratio $\alpha_m$ controls the shape of both IFP and IFV profiles and that it depends more on the variation in hydraulic conductivity, $L_p$ than on any other parameters. The model also considers $L_p$ to be homogeneous and constant over the entire tumor, which is not an accurate assumption since there is experimental evidence that clearly shows that $L_p$ is spatially and temporally heterogenous [54], resulting in a heterogeneous $\alpha_m$. We seek to include this spatial and temporal variation in our dynamical model by using the following empirical formulae for the dimensionless variable $\alpha_m$, which depend on the distribution of the vasculature.

$$\alpha_m(x,t) = \underbrace{\phi_1 m(x,t) \exp\left(\phi_2(m(x,t)-1)\right)}_{\text{Implicit time dependence}}, \tag{7.17}$$

where $\phi_1$ ($\phi_1 = 2.5$) and $\phi_2$ ($\phi_2 = 5$) are estimated in such a way that the parameter $\alpha_m$ lies within the range of the experimental values of $\alpha_m$ [54].

The justification for having a functional dependence of $\alpha_m$ on $m(x,t)$ (the average vessel distribution) is as follows: when $m$ is increased above some baseline value, this represents the case of a tumor, and so $L_p$ (and hence $\alpha_m$) should correspondingly increase. The experimental values suggests $L_p$ is about 50 times higher in tumor vessels than normal vessels, and that during anti-angiogenic therapy $L_p$ is reduced 5 fold [54]. We simply use these experimental estimates to make an "educated guess" at a formula that fits with the values of $\alpha_m$ for the different cases. The formula must give $\alpha_m = 0$ when $m = 0$ (no blood vessels and hence no source), and monotonically increase, such that the values of $m$ corresponding to the tumor case should give values of $\alpha_m$ in the range of 7- 20 [54]; thus making it as a function of space and time.

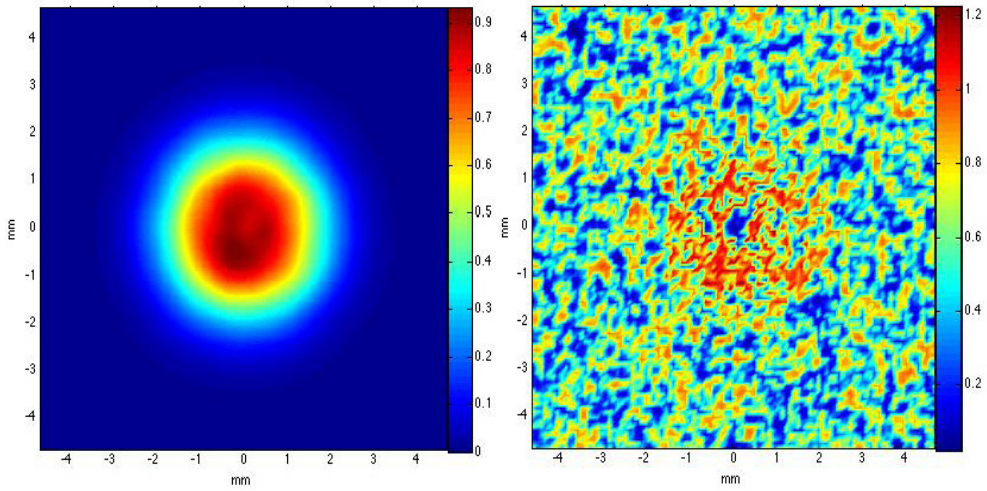


(a) Cell density (no treatment)




(b) Vascular profile (no treatment)

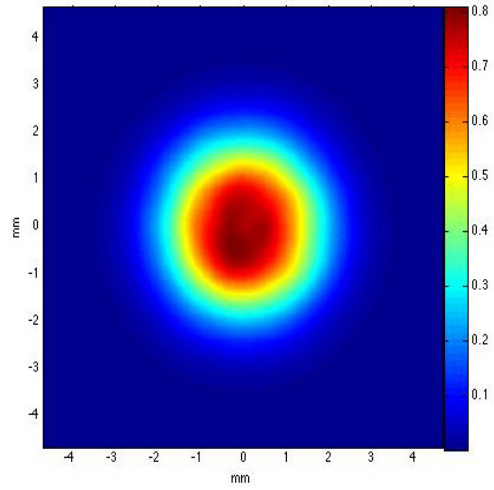


(c) Cell density (after treatment)

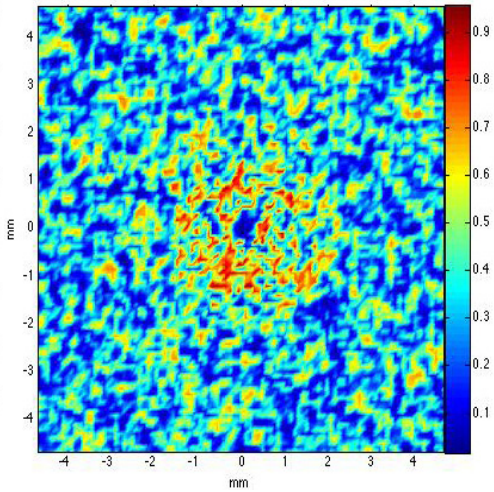


(d) Vascular profile (after treatment)

Figure 7.5: Effects of antiangiogenic therapy on cell density and vascular profile

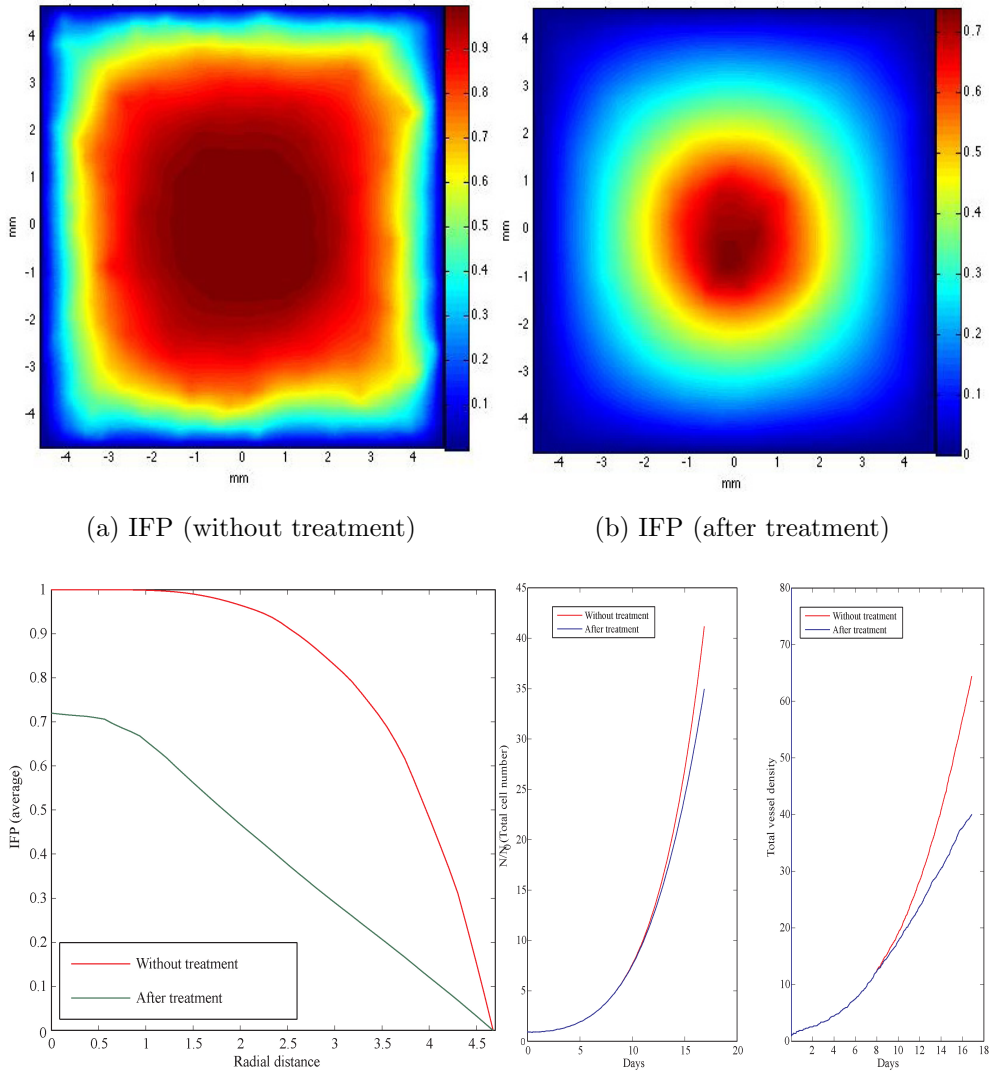


(a) IFP (without treatment)

(b) IFP (after treatment)

(c) IFP (radial profile)

(d) Change in cells and vessel

Figure 7.6: Effects of antiangiogenic therapy on IFP

**Effects on Tumor IFP**

Here, we present a mathematical model that studies the evolution of tumor vasculature and tumor cells and their relationship with the change in IFP. The equations for vasculature phenomenologically represents the nature of tumor vessels [52]. The abnormality in the tumor vessels is incorporated into the present model through the values that $m$ take, where higher values of vascular density are associated with tumor vasculature than with normal vascular distribution.

Figure 7.5 shows the spatial distribution of cancer cells (Figure 7.5 (a))and vasculature (Figure 7.5(b)) without any treatment. The dynamics of cell density, vasculature, as well as oxygen distribution has already been discussed by Kohandel *et al.* [59] in a recent publication. However, here we have included additional terms $(\beta_2 \nabla \cdot (m \nabla c))$ and $(\beta_2 \nabla \cdot (c \nabla m))$ which were previously assumed to be zero. These terms represent the spatiotemporal and directed movement of tumor vessels and tumor cells within the tumor [96]. This directed movement moves the blood vessels towards the tumor boundary and is usually seen in experimental solid tumors where the tumor starts recruiting new vessels through angiogenesis. From Figure 7.5 (b), it can be seen that the vessels located near the boundary of the tumor are of higher density than other spatial locations, especially the central part of the solid tumor. As a result of thism the tumor cells at the center are starved for oxygen and often develop hypoxic regions, which in turn promotes increased angiogenesis, creating leaky and tortuous tumor vessels. This abnormal structure of the tumor vasculature with irregular and leaky blood vessels often accounts for its abnormal function, which results in increased the tumor IFP to much higher values than seen in the normal tissues (Jain 2007).

Figure 7.6 (a) and (c) show the spatial distribution of IFP within and around

the tumor boundary and the change in IFP with radial distance from the center of the tumor volume, respectively. Note that, we have used an empirical formula for $\alpha_m$ which is a function of the vessel density $m(x,t)$ and is thus a heterogeneous variable throughout the spatial domain contrary to Jain *et al.* [54]. Since $\alpha_m$ is a function of $m$, this will also account for changes in various transport properties that arise with changes in the tumor microenvironment. Here, the values for $\alpha_m$ vary from 0 to 9.6, depending on the spatial location. It can be seen from Figure 7.6 (a) and (c) that the IFP is uniformly high within the tumor (of radius 1.5 to 2 mm approximately) and then drops suddenly near the boundary towards zero when it reaches normal tissue. These are consistent with the results obtained by various other researchers by using different values of $\alpha_m$ for normal and tumor tissues [54].

The effect of antiangiogenic therapy on tumor cells and vascular distribution is shown in Figures 7.5 (c) and (d). Note that the color bar indicates the cell and vessel density in the figure and is different from the no treatment case (Figure 7.5 (a) and (b)). In general, the administration of antiangiogenic therapy partially reduces the vessel density $m$, leading to a minor delay in the tumor growth as shown in Figure 7.3 (d). Here, lowering the values of $m$ corresponds to pruning the abnormal vessels and functionally normalizing them. However, since the application of antiangiogenic therapy also affects the normal vessels (density close to 1), care should be taken in prescribing the accurate amount of dosage so as to obtain a balance between the normal vessels and normalized vessels (or a "normalization window") [52]. Here, the dosage parameter $A_i$ is fixed in such a way that the total vessel density is reduced by about 50% of that of the untreated case, as is usually observed in experimental settings [54].

As the antiangiogenic therapy decreases overall vessel density which is distributed heterogeneously throughout the tumor, it also changes the transport prop-

erties within the tumor. The functional dependence of the parameter $\alpha_m$ through the empirical equation, Equation 7.17, successfully incorporates these changes into the present mathematical model. After the therapy, a decrease in the values of vessel density lowers the parameter $\alpha_m$ to a range of 0 to 2, which represents the case of a normal tissue [54]. This change in $\alpha_m$ lowers IFP within the tumor by up to 75%, and is consistent with clinical findings [54] (data from PMH). Figures 7.3 (a), (b), and (c) show these changes in IFP with and without the application of antiangiogenic therapy.

## 7.5 A Short Summary

Recently, there have been much experimental and clinical findings suggesting various prognostic and therapeutic implications of elevated IFP within solid tumors [54, 75, 52]. As elevated tumor IFP negatively affects most of the diagnostic and therapeutic strategies in controlling a growing tumor; analysis of IFP and other possible methods through which this might be lowered, is of critical importance. In this chapter, we have used a mathematical model to gain insight into the various mechanisms that contribute to the elevation of tumor IFP. Most of the transport properties that affect IFP are directly or indirectly related to the abnormal tumor vasculature that is created as a result of upregulated angiogenesis. Since these vascular networks are spatially and temporally heterogenous in nature, the mathematical model is modified accordingly to simulate accurate tissue specific pressure and velocity profiles. Here, we have also presented a simple mathematical model for the evolution of tumor cells and vasculature and proposed an empirically derived model for IFP that implicitly incorporates the spatial and temporal changes in the vascular network. This updated mathematical model is then used to study

the role of antiangiogenic therapy in lowering IFP, and we observe the creation of a "normalization window" for effective drug delivery.

# Chapter 8

# Conclusions and Future Directions

## 8.1 Concluding Remarks

The incorporation of necessary biological or clinical information regarding the evolution of cancer and its treatments play a vital role in the accuracy of related mathematical models and their predictive capabilities. The success of a sensible mathematical model also depends on the modeling strategies through this important information included. In this thesis, we have presented a simple and novel contribution to the rapidly growing area of Mathematical Oncology by improving the predictive capability of the traditional mathematical models using appropriate and relevant data obtained through various imaging modalities.

Brain tumors are one of the most aggressive and devastating types of tumors with a minimal survival rate, even after treatment with multilevel therapeutic strategies which include surgery, radiotherapy, chemotherapy and/or antiangiogenic therapy. However, as it has been observed in various clinical trials, careful planning and optimal scheduling of these aforementioned multi-modality treatment strategies

may further increase the survival rates of patients with brain tumors. In light of the need for a well established, cost effective methodology for testing hypothesis and drawing relevant conclusions and making well grounded conjectures, we presented a simple mathematical model in Chapter 5 that studies the effects of radiotherapy with/without sequencing with a chemotherapeutic drug named Temozolomide. In the case of radiation therapy, previous mathematical models in the literature have tended to neglect the spatial factor in determining the cell survival status, which is often an important issue. Using previously developed radiotherapeutic models, it is also very difficult or rather impossible to compare the effects of various fractionation schedules and doses, in order to determine better treatment protocols under various different circumstances. The mathematical model presented here has succeeded in incorporating the spatial effects as well as the effects of various dosage schedules with the help of a generalized linear quadratic model. The developed model is then used to estimate the clinically relevant radiotherapeutic parameters and the model predictions are further validated with the help of a series of clinical trial data taken from the literature. Using this model, we have also attempted to make some suggestions and draw conclusions regarding different sequencing options, which might need further experimental confirmation.

While the above model has provided some clinically relevant understanding of radio- and chemotherapeutic effects, it would be more beneficial and accurate if we could incorporate the effects of other significant microenvironmental factors such as hypoxia and interstitial fluid pressure, which negatively impact these therapeutic outcomes. Chapters 6 and 7 mainly focused on the modeling of these microenvironmental factors independently in order to gain more insight into their interaction with the tumor cells and treatment strategies.

The analysis and estimation of tissue specific hypoxia, one of the typical and

critical hallmarks of advanced tumors are carried out in Chapter 6. Here, the developed model successfully generated the oxygenation maps of various tumor cross sections by using its corresponding heterogenous vascular distribution. Images of these vascular distributions were previously obtained through a series of staining and immunohistochemical analysis of the tumor tissue. The simulated oxygen distribution is then quantified using two different estimation approaches with the aim of comparing these techniques; and the obtained values are further validated against the available biomarker findings. The results of these analyses were highly consistent with the previously published clinical studies in the literature. The successful implementation of this image based modeling approach reveals that it is possible to estimate average hypoxia without any invasive or expensive techniques but by simply knowing the distribution of vasculature within the area of interest. The implications of hypoxia in calculating overall survival results is also discussed here based on the estimated oxygenation mappings, and it was found that consideration of the heterogeneous distribution of oxygen plays an important role in the accurate prescription of radiation dosage.

While hypoxia increases the radio-resistance of cancer cells, elevated tumor IFP decreases the delivery of anticancer drugs into the tumor tissue. In the literature, there are a variety of studies that have analyzed the issue of elevated IFP and the effects of its relative changes, but mostly by assuming the tissue to be a homogenous. However, since the structurally and functionally abnormal vasculature has a very significant effect in elevating tumor IFP, Chapter 7 aimed at incorporating this heterogeneity into the homogeneous mathematical model. The resulting IFP profiles generated using the known vascular distribution obtained from biopsy images, clearly showed that the tumor IFP varies depending on the distribution of vasculature and in each case it is spatially heterogenous. Moreover, the tumor

vasculature evolves over time, depending on the increasing demands of rapidly proliferating cancer cells resulting in a temporal change in IFP within the tumor. In Chapter 7, we also presented a phenomenological mathematical modeling approach, using which we discussed these temporal changes in tumor vasculature as well as in tumor IFP. Using this model, we have provided a theoretical explanation of the experimental finding of more efficient drug delivery to the tumor after administration antiangiogenic therapy.

In conclusion, we have presented a mathematical model for the evolution of brain tumors and used it to study the effects of chemotherapy and radiotherapy. Although, we discussed the modeling of microenvironmental factors independently in Chapters 6 and 7, the ultimate goal of this brain tumor project is to incorporate these and various other effects (discussed below) into the main growth model, which will be the final step of this ongoing project. Moreover, once such a model is developed, it can also be used to predict the survival status of individual patients by incorporating the patient-specific parameters, which could be obtained through various diagnostic protocols such as image analysis of patient biopsies and sequence analysis of MRIs or CT scans. Developing this comprehensive, individualized mathematical model that is supplemented with patient-specific data would greatly help clinicians to provide the best possible treatment protocol to individual patients.

## 8.2 Future Possibilities

The refinement of mathematical models is an ongoing process through which we include more and more relevant details into the model which further increases its predictive capability, taking us few more steps closer to the clinical findings. The models presented in this thesis can also be modified further in various ways and a

few of these future modifications may be of following types.

One of the important modifications which is worthwhile incorporating is the modeling of clinically relevant vascular networks which vary spatially as well as temporally. The inclusion of these vascular networks will allow one to incorporate the blood flow into the current model which will be further helpful in various theoretical and clinical contexts such as in the prediction of the temporal evolution of tumor hypoxia and tumor IFP. It will also help in quantifying variations in interstitial and intravascular transport of nutrients and anti-cancer drugs, and in the planning of optimal delivery (conventional as well as carrier mediated) of anticancer drugs. Another concept that might be useful to incorporate while modeling these vascular networks is the effect of pro-angiogenic and anti-angiogenic growth factors in the upregulation of tumor angiogenesis, which is one of the ongoing project that we are currently involved.

In Chapter 6, we have seen a simple mathematical model for simulating the tissue oxygenation map, where due to the lack of necessary details we were unable to consider the tissue heterogeneity in the intra-tumor transport of oxygen. However, this can be modified easily by considering the diffusion coefficient for oxygen molecules to be a function of the spatial variable. It might be also of interest to include heterogeneity in considering tumor cells, since every tumor consists of cells with several phenotypic and genotypic characteristics, which may have varying effects on proliferation, migration, or even on the tumor response to different anticancer treatments [48]. As we have seen, cancer is a heterogeneous disease often requiring complex alterations of a normal cell to drive it to malignancy and ultimately to a metastatic state. These alterations are largely due to aberrant expression of a set of genes or pathways such as p53 pathways and hypoxia pathways rather than a single gene and thus it might be helpful to incorporate these details

into the current mathematical models to understand various mechanisms involved in the regulation and deregulation of these pathways and how they relate to tumor progression.

Another possible direction is to consider tumor growth from a cancer stem cell point of view. Recently, there has been mounting evidence that suggests the involvement of cancer stem like cells in initiating and maintaining brain tumors. According to this hypothesis, the failure of chemotherapy and radiotherapy could be partially due to the resistance of cancer stemlike cells to these treatments. From a modeling perspective, gliomas can be considered to be heterogeneous tumors consisting of different populations of cancer stem like, progenitor and fully differentiated cells with varying sensitivities towards cytotoxic therapies. A spatio-temporal mathematical model can be developed similar to the one we presented in Chapter 5 to study the effects of cell heterogeneity on the outcome of various treatment protocols, including antiangiogenic therapy.

One of the major issues in incorporating all these details into a single mathematical model is the complexity of various spatial and temporal scales. This multi-scale complexity of cancer progression warrants a multi-scale modeling approach to produce truly predictive mathematical models. In order to capture all the dynamics of tumor progression, we need to couple processes that are occurring at widely disparate length and time scales. There are several articles in the literature that provide frameworks for building multi-scale cancer progression models. Following these earlier works, it would be possible to develop a detailed mathematical model capable of studying the variations in vascular density, blood flow, IFP, nutrient supply (in particular, oxygen distribution) within and around a growing tumor, under the appropriate length and time scales. It would be also very interesting to examine the changes in tumor microenvironment during the course of delivery of

various anticancer drugs through different delivery schemes. This type of approach could be useful in modeling cancer stem cell heterogeneity. The nature of this interdisciplinary area of mathematics necessitates an effective way of communication between the experts in different areas of science, such as biology, medicine and mathematics. A clear and efficient visualization platform is one of various ways through which this can be achieved. It also gives an effective way to analyze and study the results of our multi-scale analysis at specific time points, especially when we are dealing with simulations involving three or more dimensions.

# References


[1] Cocosco C A, Kollokian V, Kwan R K S, and Evans A C. Brain web: online interface to a 3D MRI simulated brain database . *NeuroImage*, 5:S425, 1997.

[2] J. Adam. A simplified mathematical model of tumor growth. *Mathematical Biosciences*, 81(2):229–244, 1986.

[3] T. Alper and P. Howard-Flanders. Role of oxygen in modifying the radiosensitivity of E. coli B. *Nature*, 178:978–979, Nov 1956.

[4] A. R. Anderson and M. A. Chaplain. Continuous and discrete mathematical models of tumor-induced angiogenesis. *Bull. Math. Biol.*, 60:857–899, Sep 1998.

[5] R. P. Araujo and D. L. McElwain. A history of the study of solid tumour growth: the contribution of mathematical modelling. *Bull. Math. Biol.*, 66:1039–1091, Sep 2004.

[6] P. Armitage and R. Doll. The age distribution of cancer and a multi-stage theory of carcinogenesis. *Br. J. Cancer*, 8:1–12, Mar 1954.

[7] D. Balding and D. L. McElwain. A mathematical model of tumour-induced capillary growth. *J. Theor. Biol.*, 114:53–73, May 1985.

[8] K. Bartha and H. Rieger. Vascular network remodeling via vessel cooption, regression and growth in tumors. *J. Theor. Biol.*, 241:903–918, Aug 2006.

[9] L. T. Baxter and R. K. Jain. Transport of fluid and macromolecules in tumors. I. Role of interstitial pressure and convection. *Microvasc. Res.*, 37:77–104, Jan 1989.

[10] G. Berg, E. Blomquist, and E. Cavallin-Sthl. A systematic overview of radiation therapy effects in brain tumours. *Acta Oncol*, 42:582–588, 2003.

[11] P. Black. Management of malignant glioma: role of surgery in relation to multimodality therapy. *J. Neurovirol.*, 4:227–236, Apr 1998.

[12] D. J. Brenner, L. R. Hlatky, P. J. Hahnfeldt, E. J. Hall, and R. K. Sachs. A convenient extension of the linear-quadratic model to include redistribution and reoxygenation. *Int. J. Radiat. Oncol. Biol. Phys.*, 32:379–390, May 1995.

[13] R. G. Bristow and R. P. Hill. Hypoxia and metabolism. Hypoxia, DNA repair and genetic instability. *Nat. Rev. Cancer*, 8:180–192, Mar 2008.

[14] D. M. Brizel, G. L. Rosner, J. Harrelson, L. R. Prosnitz, and M. W. Dewhirst. Pretreatment oxygenation profiles of human soft tissue sarcomas. *Int. J. Radiat. Oncol. Biol. Phys.*, 30:635–642, Oct 1994.

[15] D. M. Brizel, G. L. Rosner, L. R. Prosnitz, and M. W. Dewhirst. Patterns and variability of tumor oxygenation in human soft tissue sarcomas, cervical carcinomas, and lymph node metastases. *Int. J. Radiat. Oncol. Biol. Phys.*, 32:1121–1125, Jul 1995.

[16] P. K. Burgess, P. M. Kulesa, J. D. Murray, and E. C. Alvord. The interaction of growth rates and diffusion coefficients in a three-dimensional mathematical model of gliomas. *J. Neuropathol. Exp. Neurol.*, 56:704–713, Jun 1997.

[17] A. C. Burton. Rate of growth of solid tumours as a problem of diffusion. *Growth*, 30:157–176, Jun 1966.

[18] H. M. Byrne and M. A. Chaplain. Mathematical models for tumour angiogenesis: numerical simulations and nonlinear wave solutions. *Bull. Math. Biol.*, 57:461–486, May 1995.

[19] H. M. Byrne and M. A. J. Chaplain. Modelling the role of cell-cell adhesion in the growth and development of carcinomas. *Mathematical and Computer Modelling*, 24(12):1 – 17, 1996.

[20] M. Chaplain and A. Anderson. Mathematical modelling of tumour-induced angiogenesis: network growth and structure. *Cancer Treat. Res.*, 117:51–75, 2004.

[21] M. A. Chaplain. The mathematical modelling of tumour angiogenesis and invasion. *Acta Biotheor.*, 43:387–402, Dec 1995.

[22] M. A. Chaplain and A. R. Anderson. Mathematical modelling, simulation and prediction of tumour-induced angiogenesis. *Invasion Metastasis*, 16:222–234, 1996.

[23] M. A. Chaplain, S. M. Giles, B. D. Sleeman, and R. J. Jarvis. A mathematical analysis of a model for tumour angiogenesis. *J Math Biol*, 33:744–770, 1995.

[24] M. A. Chaplain, S. R. McDougall, and A. R. Anderson. Mathematical modeling of tumor-induced angiogenesis. *Annu Rev Biomed Eng*, 8:233–257, 2006.

[25] W. Y. Chen, P. R. Annamreddy, and L. T. Fan. Modeling growth of a heterogeneous tumor. *J. Theor. Biol.*, 221:205–227, Mar 2003.

[26] S. Chuang. Mathematic models for cancer chemotherapy: pharmacokinetic and cell kinetic considerations. *Cancer Chemother Rep*, 59:827–842, 1975.

[27] O. Clatz, P.Y. Bondiau, H. Delingette, M. Sermesant, S.K. Warfield, G. Malandain, and N. Ayache. Brain tumor growth simulation, Apr 2004. available at `http://hal.inria.fr/docs/00/07/14/01/PDF/RR-5187.pdf`.

[28] O. Clatz, M. Sermesant, P. Y. Bondiau, H. Delingette, S. K. Warfield, G. Malandain, and N. Ayache. Realistic simulation of the 3-D growth of brain tumors in MR images coupling diffusion with biomechanical deformation. *IEEE Trans Med Imaging*, 24:1334–1346, Oct 2005.

[29] D. L. Collins, A. P. Zijdenbos, V. Kollokian, J. G. Sled, N. J. Kabani, C. J. Holmes, and A. C. Evans. Design and construction of a realistic digital brain phantom. *IEEE Trans Med Imaging*, 17:463–468, Jun 1998.

[30] J. Cook, D. E. Woodward, P. Tracqui, and J. D. Murray. Resection of gliomas and life expectancy . *J. Neurooncol.*, 24:131, 1995.

[31] G. C. Cruywagen, D. E. Woodward, P. Tracqui, G. T. Bartoo, J. D. Murray, and E. C. Jr Alvord. The modelling of diffusive tumors . *J. Biol. Syst.*, 3:937–945, 1995.

[32] W. J. Curran, C. B. Scott, J. Horton, J. S. Nelson, A. S. Weinstein, D. F. Nelson, A. J. Fischbach, C. H. Chang, M. Rotman, and S. O. Asbell. Does extent of surgery influence outcome for astrocytoma with atypical or anaplastic foci (AAF)? A report from three Radiation Therapy Oncology Group (RTOG) trials. *J. Neurooncol.*, 12:219–227, Mar 1992.

[33] A. Dasu, I. Toma-Dasu, and M. Karlsson. Theoretical simulation of tumour oxygenation and results from acute and chronic hypoxia. *Phys Med Biol*, 48:2829–2842, Sep 2003.

[34] A. Dasu, I. Toma-Dasu, and M. Karlsson. The effects of hypoxia on the theoretical modelling of tumour control probability. *Acta Oncol*, 44:563–571, 2005.

[35] L. M. DeAngelis. Brain tumors. *N. Engl. J. Med.*, 344:114–123, Jan 2001.

[36] L. M. DeAngelis. Chemotherapy for brain tumors–a new beginning. *N. Engl. J. Med.*, 352:1036–1038, Mar 2005.

[37] L. M. DeAngelis, P. C. Burger, S. B. Green, and J. G. Cairncross. Malignant glioma: who benefits from adjuvant chemotherapy? *Ann. Neurol.*, 44:691–695, Oct 1998.

[38] M. W. Dewhirst, I. C. Navia, D. M. Brizel, C. Willett, and T. W. Secomb. Multiple etiologies of tumor hypoxia require multifaceted solutions. *Clin. Cancer Res.*, 13:375–377, Jan 2007.

[39] H. O. Fadnes, R. K. Reed, and K. Aukland. Interstitial fluid pressure in rats measured with a modified wick technique. *Microvasc. Res.*, 14:27–36, Jul 1977.

[40] J. F. Fowler. The linear-quadratic formula and progress in fractionated radiotherapy. *Br J Radiol*, 62:679–694, Aug 1989.

[41] S. A. Frank and M. A. Nowak. Cell biology: Developmental predisposition to cancer. *Nature*, 422:494, Apr 2003.

[42] R. A. Gatenby and E. T. Gawlinski. The glycolytic phenotype in carcinogenesis and tumor invasion: insights through mathematical models. *Cancer Res.*, 63:3847–3854, Jul 2003.

[43] R. A. Gatenby and R. J. Gillies. Glycolysis in cancer: a potential target for therapy. *Int. J. Biochem. Cell Biol.*, 39:1358–1366, 2007.

[44] J. L. Gevertz and S. Torquato. Modeling the effects of vasculature evolution on early brain tumor growth. *J. Theor. Biol.*, 243:517–531, Dec 2006.

[45] H. P. Greenspan. On the growth and stability of cell cultures and solid tumors. *J. Theor. Biol.*, 56:229–242, Jan 1976.

[46] C. Guiot, P. G. Degiorgis, P. P. Delsanto, P. Gabriele, and T. S. Deisboeck. Does tumor growth follow a "universal law"? *J. Theor. Biol.*, 225:147–151, Nov 2003.

[47] Eric J. Hall. *Radiobiology for the Radiologist*. Lippincott Williams & Wilkins, 4th edition, September 1993.

[48] D. Hanahan and J. Folkman. Patterns and emerging mechanisms of the angiogenic switch during tumorigenesis. *Cell*, 86:353–364, Aug 1996.

[49] N. H. Holford and L. B. Sheiner. Pharmacokinetic and pharmacodynamic modeling in vivo. *Crit Rev Bioeng*, 5:273–322, 1981.

[50] E. C. Holland. Glioblastoma multiforme: the terminator. *Proc. Natl. Acad. Sci. U.S.A.*, 97:6242–6244, Jun 2000.

[51] J. A. Hudson and D. B. Carter. Analysis of factors affecting tissue Oxygen tension. *Proc. R. Soc. Lond., B, Biol. Sci.*, 161:247–274, Dec 1964.

[52] R. K. Jain. Normalization of tumor vasculature: an emerging concept in antiangiogenic therapy. *Science*, 307:58–62, Jan 2005.

[53] R. K. Jain and L. T. Baxter. Mechanisms of heterogeneous distribution of monoclonal antibodies and other macromolecules in tumors: significance of elevated interstitial pressure. *Cancer Res.*, 48:7022–7032, Dec 1988.

[54] R. K. Jain, R. T. Tong, and L. L. Munn. Effect of vascular normalization by antiangiogenic therapy on interstitial hypertension, peritumor edema, and lymphatic metastasis: insights from a mathematical model. *Cancer Res.*, 67:2729–2735, Mar 2007.

[55] B. Jansson and I. Revesz. Analysis of the growth of tumor cell populations. *Mathematical Biosciences*, 19:131–154, 1974.

[56] W. T. Jenkins, S. M. Evans, and C. J. Koch. Hypoxia and necrosis in rat 9L glioma and Morris 7777 hepatoma tumors: comparative measurements using EF5 binding and the Eppendorf needle electrode. *Int. J. Radiat. Oncol. Biol. Phys.*, 46:1005–1017, Mar 2000.

[57] M. C. Kavanagh, A. Sun, Q. Hu, and R. P. Hill. Comparing techniques of measuring tumor hypoxia in different murine tumors: Eppendorf pO2 Histograph, [3H]misonidazole binding and paired survival assay. *Radiat. Res.*, 145:491–500, Apr 1996.

[58] A. G. Knudson. Mutation and cancer: statistical study of retinoblastoma. *Proc. Natl. Acad. Sci. U.S.A.*, 68:820–823, Apr 1971.

[59] M. Kohandel, M. Kardar, M. Milosevic, and S. Sivaloganathan. Dynamics of tumor growth and combination of anti-angiogenic and cytotoxic therapies. *Phys Med Biol*, 52:3665–3677, Jul 2007.

[60] M. Kohandel, S. Sivaloganathan, and A. Oza. Mathematical modeling of ovarian cancer treatments: sequencing of surgery and chemotherapy. *J. Theor. Biol.*, 242:62–68, Sep 2006.

[61] R. W. Kwan, A. C. Evans, and G. B. Pike. An extensible MRI simulator for post-processing evaluation. *Proc. 4th Int. Conf. on Visualization in Biomedical Computing*, 96:135–140, 1996.

[62] A. K. Laird. Dynamics of tumor growth. *Br. J. Cancer*, 13:490–502, Sep 1964.

[63] D. A. Larson and W. M. Wara. Radiotherapy of primary malignant brain tumors. *Semin Surg Oncol*, 14:34–42, 1998.

[64] H. A. Levine, B. D. Sleeman, and M. Nilsen-Hamilton. Mathematical modeling of the onset of capillary formation initiating angiogenesis. *J Math Biol*, 42:195–238, Mar 2001.

[65] A. S. Ljungkvist, J. Bussink, J. H. Kaanders, and A. J. van der Kogel. Dynamics of tumor hypoxia measured with bioreductive hypoxic cell markers. *Radiat. Res.*, 167:127–145, Feb 2007.

[66] S. Lonardi, A. Tosoni, and A. A. Brandes. Adjuvant chemotherapy in the treatment of high grade gliomas. *Cancer Treat. Rev.*, 31:79–89, Apr 2005.

[67] B. B. Ma, R. G. Bristow, J. Kim, and L. L. Siu. Combined-modality treatment of solid tumors using radiotherapy and molecular targeted agents. *J. Clin. Oncol.*, 21:2760–2776, Jul 2003.

[68] N. V. Mantzaris, S. Webb, and H. G. Othmer. Mathematical modeling of tumor-induced angiogenesis. *J Math Biol*, 49:111–187, Aug 2004.

[69] J. H. Mao, K. A. Lindsay, A. Balmain, and T. E. Wheldon. Stochastic modelling of tumorigenesis in p53 deficient mice. *Br. J. Cancer*, 77:243–252, 1998.

[70] W. P. Mason and J. G. Cairncross. Drug Insight: temozolomide as a treatment for malignant glioma–impact of a recent trial. *Nat Clin Pract Neurol*, 1:88–95, Dec 2005.

[71] A. Matzavinos, C. Y. Kao, J. E. Green, A. Sutradhar, M. Miller, and A. Friedman. Modeling oxygen transport in surgical tissue transfer. *Proc. Natl. Acad. Sci. U.S.A.*, 106:12091–12096, Jul 2009.

[72] S. R. McDougall, A. R. Anderson, M. A. Chaplain, and J. A. Sherratt. Mathematical modelling of flow through vascular networks: implications for tumour-induced angiogenesis and chemotherapy strategies. *Bull. Math. Biol.*, 64:673–702, Jul 2002.

[73] D. L. S. McElwain and P. J. Ponzo. A model for the growth of a solid tumor with non-uniform oxygen consumption. *Math. Biosci*, 35:267–279, 1977.

[74] S. Michelson, K. Ito, H. T. Tran, and J. T. Leith. Stochastic models for subpopulation emergence in heterogeneous tumors. *Bull. Math. Biol.*, 51:731–747, 1989.

[75] M. Milosevic, A. Fyles, D. Hedley, and R. Hill. The human tumor microenvironment: invasive (needle) measurement of oxygen and interstitial fluid pressure. *Semin Radiat Oncol*, 14:249–258, Jul 2004.

[76] R. A. Morantz and J. W. Walsh. *Brain tumors*. Informa Health Care, 1993.

[77] J. D Murray. *The Mathematical Biology I and II,Interdisciplinary Applied Mathematics 3rd edn.* Berlin: Springer, 2003.

[78] C. Neider, U. Nestle, M. Niewald, K. Walter, and K. Schnabel. Hyperfractionated reirradiation for malignant glioma. *Front Radiat Ther Oncol*, 33:150–157, 1999.

[79] D. F. Nelson, W. J. Curran, C. Scott, J. S. Nelson, A. S. Weinstein, K. Ahmad, L. S. Constine, K. Murray, W. D. Powlis, and M. Mohiuddin. Hyperfractionated radiation therapy and bis-chlorethyl nitrosourea in the treatment of malignant glioma–possible advantage observed at 72.0 Gy in 1.2 Gy B.I.D. fractions: report of the Radiation Therapy Oncology Group Protocol 8302. *Int. J. Radiat. Oncol. Biol. Phys.*, 25:193–207, Jan 1993.

[80] P. Nilsson, H. D. Thames, and M. C. Joiner. A generalized formulation of the 'incomplete-repair' model for cell survival and tissue response to fractionated low dose-rate irradiation. *Int. J. Radiat. Biol.*, 57:127–142, Jan 1990.

[81] M. Nordsmark, J. Loncaster, C. Aquino-Parsons, S. C. Chou, M. Ladekarl, H. Havsteen, J. C. Lindegaard, S. E. Davidson, M. Varia, C. West, R. Hunter, J. Overgaard, and J. A. Raleigh. Measurements of hypoxia using pimonidazole and polarographic oxygen-sensitive electrodes in human cervix carcinomas. *Radiother Oncol*, 67:35–44, Apr 2003.

[82] M. Nordsmark, J. Loncaster, S. C. Chou, H. Havsteen, J. C. Lindegaard, S. E. Davidson, M. Varia, C. West, R. Hunter, J. Overgaard, and J. A. Raleigh. Invasive oxygen measurements and pimonidazole labeling in human cervix carcinoma. *Int. J. Radiat. Oncol. Biol. Phys.*, 49:581–586, Feb 2001.

[83] L. Norton. A Gompertzian model of human breast cancer growth. *Cancer Res.*, 48:7067–7071, Dec 1988.

[84] L. Norton and R. Simon. Tumor size, sensitivity to therapy, and design of treatment schedules. *Cancer Treat Rep*, 61:1307–1317, Oct 1977.

[85] L. Norton and R. Simon. The Norton-Simon hypothesis revisited. *Cancer Treat Rep*, 70:163–169, Jan 1986.

[86] L. Norton, R. Simon, H. D. Brereton, and A. E. Bogden. Predicting the course of Gompertzian growth. *Nature*, 264:542–545, Dec 1976.

[87] P. Nyberg, T. Salo, and R. Kalluri. Tumor microenvironment and angiogenesis. *Front. Biosci.*, 13:6537–6553, 2008.

[88] J. A. O'Donoghue. The response of tumours with Gompertzian growth characteristics to fractionated radiotherapy. *Int. J. Radiat. Biol.*, 72:325–339, Sep 1997.

[89] P. L. Olive, J. P. Banth, and C. Aquino-Parsons. Measuring hypoxia in solid tumours–is there a gold standard? *Acta Oncol*, 40:917–923, 2001.

[90] J. C. Panetta. A mathematical model of breast and ovarian cancer treated with paclitaxel. *Math Biosci*, 146:89–113, Dec 1997.

[91] J. B. Plotkin and M. A. Nowak. The different effects of apoptosis and DNA repair on tumorigenesis. *J. Theor. Biol.*, 214:453–467, Feb 2002.

[92] G. Powathil, M. Kohandel, M. Milosevic, and S. Sivaloganathan. Modeling the spatial distribution of tumor hypoxia: a comparison between biomarkers and polarographic electrode technique. *Int. J. Radiat. Oncol. Biol. Phys.*, 2009 (Submitted).

[93] G. Powathil, M. Kohandel, S. Sivaloganathan, A. Oza, and M. Milosevic. Mathematical modeling of brain tumors: effects of radiotherapy and chemotherapy. *Phys Med Biol*, 52:3291–3306, Jun 2007.

[94] X. S. Qi, C. J. Schultz, and X. A. Li. An estimation of radiobiologic parameters from clinical outcomes for radiation treatment planning of brain tumor. *Int. J. Radiat. Oncol. Biol. Phys.*, 64:1570–1580, Apr 2006.

[95] J. A. Raleigh, S. C. Chou, G. E. Arteel, and M. R. Horsman. Comparisons among pimonidazole binding, oxygen electrode measurements, and radiation response in C3H mouse tumors. *Radiat. Res.*, 151:580–589, May 1999.

[96] S. Ramanujan, G. C. Koenig, T. P. Padera, B. R. Stoll, and R. K. Jain. Local imbalance of proangiogenic and antiangiogenic factors: a potential mechanism of focal necrosis and dormancy in tumors. *Cancer Res.*, 60:1442–1448, Mar 2000.

[97] I. Ramis-Conde, D. Drasdo, A. R. Anderson, and M. A. Chaplain. Modeling the influence of the E-cadherin-beta-catenin pathway in cancer cell invasion: a multiscale approach. *Biophys. J.*, 95:155–165, Jul 2008.

[98] M. W. Retsky, D. E. Swartzendruber, R. H. Wardwell, and P. D. Bame. Is Gompertzian or exponential kinetics a valid description of individual human cancer growth? *Med. Hypotheses*, 33:95–106, Oct 1990.

[99] P. F. Rijken, H. J. Bernsen, J. P. Peters, R. J. Hodgkiss, J. A. Raleigh, and A. J. van der Kogel. Spatial relationship between hypoxia and the (perfused) vascular network in a human glioma xenograft: a quantitative multiparameter analysis. *Int. J. Radiat. Oncol. Biol. Phys.*, 48:571–582, Sep 2000.

[100] R. Rockne, E. C. Alvord, J. K. Rockhill, and K. R. Swanson. A mathematical model for brain tumor response to radiation therapy. *J Math Biol*, 58:561–578, Apr 2009.

[101] R. K. Sachs, P. Hahnfeld, and D. J. Brenner. The link between low-LET dose-response relations and the underlying kinetics of damage production/repair/misrepair. *Int. J. Radiat. Biol.*, 72:351–374, Oct 1997.

[102] R. K. Sachs, I. Shuryak, D. Brenner, H. Fakir, L. Hlatky, and P. Hahnfeldt. Second cancers after fractionated radiotherapy: stochastic population dynamics effects. *J. Theor. Biol.*, 249:518–531, Dec 2007.

[103] RK Sachs, LR Hlatky, and P Hahnfeldt. Simple ode models of tumor growth and anti-angiogenic or radiation treatment. *Mathematical and Computer Modelling*, 33:1297–1305, Jun 2001.

[104] T. W. Secomb, R. Hsu, M. W. Dewhirst, B. Klitzman, and J. F. Gross. Analysis of oxygen transport to tumor tissue by microvascular networks. *Int. J. Radiat. Oncol. Biol. Phys.*, 25:481–489, Feb 1993.

[105] T. W. Secomb, R. Hsu, E. T. Ong, J. F. Gross, and M. W. Dewhirst. Analysis of the effects of oxygen supply and demand on hypoxic fraction in tumors. *Acta Oncol*, 34:313–316, 1995.

[106] B. H. Shahine, C. E. Ng, and G. P. Raaphorst. Modelling of continuous low dose rate and accelerated fractionated high dose rate irradiation treatments in a human glioma cell line. *Int. J. Radiat. Biol.*, 70:555–561, Nov 1996.

[107] Y. Shibamoto, Y. Nishimura, K. Tsutsui, K. Sasai, M. Takahashi, and M. Abe. Comparison of accelerated hyperfractionated radiotherapy and con-

ventional radiotherapy for supratentorial malignant glioma. *Jpn. J. Clin. Oncol.*, 27:31–36, Feb 1997.

[108] D. L. Silbergeld and M. R. Chicoine. Isolation and characterization of human malignant glioma cells from histologically normal brain. *J. Neurosurg.*, 86:525–531, Mar 1997.

[109] G D Smith. *Numerical solution of partial differential equations.* Oxford Applied Mathematics and computing Science Series, 1985.

[110] L. Sontag and D. E. Axelrod. Evaluation of pathways for progression of heterogeneous breast tumors. *J. Theor. Biol.*, 232:179–189, Jan 2005.

[111] A. Stephanou, S. R. McDougall, A. R. A. Anderson, and M. A. J. Chaplain. Mathematical modelling of flow in 2D and 3D vascular networks: applications to anti-angiogenic and chemotherapeutic drug strategies. *Mathematical and Computer Modelling*, 41(10):1137–1156, 2005.

[112] C. L. Stokes and D. A. Lauffenburger. Analysis of the roles of microvessel endothelial cell random motility and chemotaxis in angiogenesis. *J. Theor. Biol.*, 152:377–403, Oct 1991.

[113] R. Stupp, M. Gander, S. Leyvraz, and E. Newlands. Current and future developments in the use of temozolomide for the treatment of brain tumours. *Lancet Oncol.*, 2:552–560, Sep 2001.

[114] R. Stupp, W. P. Mason, M. J. van den Bent, M. Weller, B. Fisher, M. J. Taphoorn, K. Belanger, A. A. Brandes, C. Marosi, U. Bogdahn, J. Curschmann, R. C. Janzer, S. K. Ludwin, T. Gorlia, A. Allgeier, D. Lacombe, J. G. Cairncross, E. Eisenhauer, and R. O. Mirimanoff. Radiotherapy

plus concomitant and adjuvant temozolomide for glioblastoma. *N. Engl. J. Med.*, 352:987–996, Mar 2005.

[115] R. Stupp and D. C. Weber. The role of radio- and chemotherapy in glioblastoma. *Onkologie*, 28:315–317, Jun 2005.

[116] K. R. Swanson, E. C. Alvord, and J. D. Murray. A quantitative model for differential motility of gliomas in grey and white matter. *Cell Prolif.*, 33:317–329, Oct 2000.

[117] K. R. Swanson, C. Bridge, J. D. Murray, and E. C. Alvord. Virtual and real brain tumors: using mathematical modeling to quantify glioma growth and invasion. *J. Neurol. Sci.*, 216:1–10, Dec 2003.

[118] D. E. Swartzendruber, M. W. Retsky, R. H. Wardwell, and P. D. Bame. An alternative approach for treatment of breast cancer. *Breast Cancer Res. Treat.*, 32:319–325, 1994.

[119] I. F. Tannock. Oxygen diffusion and the distribution of cellular radiosensitivity in tumours. *Br J Radiol*, 45:515–524, Jul 1972.

[120] I. F. Tannock, R. P. Hill, R. G. Bristow, and L. Harrington. *The Basic Science of Oncology*. McGraw-Hill Professional, 4 edition, August 2004.

[121] H. D. Thames. An 'incomplete-repair' model for survival after fractionated and continuous irradiations. *Int. J. Radiat. Biol. Relat. Stud. Phys. Chem. Med.*, 47:319–339, Mar 1985.

[122] H. D. Thames and J. H. Hendry. *Fractionation in Radiotherapy*. Taylor & Francis Ltd, illustrated edition edition, July 1987.

[123] R. H. Thomlinson and L. H. Gray. The histological structure of some human lung cancers and the possible implications for radiotherapy. *Br. J. Cancer*, 9:539–549, Dec 1955.

[124] B. Titz and R. Jeraj. An imaging-based tumour growth and treatment response model: investigating the effect of tumour oxygenation on radiation therapy response. *Phys Med Biol*, 53:4471–4488, Sep 2008.

[125] L. Toma-Dasu, A. Waites, A. Dau, and J. Denekamp. Theoretical simulation of oxygen tension measurement in tissues using a microelectrode: I. The response function of the electrode. *Physiol Meas*, 22:713–725, Nov 2001.

[126] I. P. Tomlinson and W. F. Bodmer. Failure of programmed cell death and differentiation as causes of tumors: some simple mathematical models. *Proc. Natl. Acad. Sci. U.S.A.*, 92:11130–11134, Nov 1995.

[127] I. P. Tomlinson, M. R. Novelli, and W. F. Bodmer. The mutation rate and cancer. *Proc. Natl. Acad. Sci. U.S.A.*, 93:14800–14803, Dec 1996.

[128] P. Tracqui, G. C. Cruywagen, D. E. Woodward, G. T. Bartoo, J. D. Murray, and E. C. Alvord. A mathematical model of glioma growth: the effect of chemotherapy on spatio-temporal growth. *Cell Prolif.*, 28:17–31, Jan 1995.

[129] M. J. Trotter, D. J. Chaplin, R. E. Durand, and P. L. Olive. The use of fluorescent probes to identify regions of transient perfusion in murine tumors. *Int. J. Radiat. Oncol. Biol. Phys.*, 16:931–934, Apr 1989.

[130] C. Turner, A. R. Stinchcombe, M. Kohandel, S. Singh, and S. Sivaloganathan. Characterization of brain cancer stem cells: a mathematical approach. *Cell Prolif.*, Jun 2009.

[131] S. Turner and J. A. Sherratt. Intercellular adhesion and cancer invasion: a discrete simulation using the extended Potts model. *J. Theor. Biol.*, 216:85–100, May 2002.

[132] P. Vaupel. Hypoxia and aggressive tumor phenotype: implications for therapy and prognosis. *Oncologist*, 13 Suppl 3:21–26, 2008.

[133] P. Vaupel and L. Harrison. Tumor hypoxia: causative factors, compensatory mechanisms, and cellular response. *Oncologist*, 9 Suppl 5:4–9, 2004.

[134] P. Vaupel, F. Kallinowski, and P. Okunieff. Blood flow, oxygen and nutrient supply, and metabolic microenvironment of human tumors: a review. *Cancer Res.*, 49:6449–6465, Dec 1989.

[135] M. D. Walker, T. A. Strike, and G. E. Sheline. An analysis of dose-effect relationship in the radiotherapy of malignant gliomas. *Int. J. Radiat. Oncol. Biol. Phys.*, 5:1725–1731, Oct 1979.

[136] L. M. Wein, J. E. Cohen, and J. T. Wu. Dynamic optimization of a linear-quadratic model with incomplete repair and volume-dependent sensitivity and repopulation. *Int. J. Radiat. Oncol. Biol. Phys.*, 47:1073–1083, Jul 2000.

[137] R. A. Weinberg. *The Biology of Cancer*. Garland Science, 1 edition, June 2006.

[138] N. Weiss, F. Miller, S. Cazaubon, and P. O. Couraud. [Part I: Biology of the blood-brain barrier.]. *Rev. Neurol. (Paris)*, May 2009.

[139] M. Werner-Wasik, C. B. Scott, D. F. Nelson, L. E. Gaspar, K. J. Murray, J. A. Fischbach, J. S. Nelson, A. S. Weinstein, and W. J. Curran. Final report of a phase I/II trial of hyperfractionated and accelerated hyperfractionated

radiation therapy with carmustine for adults with supratentorial malignant gliomas. Radiation Therapy Oncology Group Study 83-02. *Cancer*, 77:1535–1543, Apr 1996.

[140] G. B. West, J. H. Brown, and B. J. Enquist. A general model for ontogenetic growth. *Nature*, 413:628–631, Oct 2001.

[141] D. Wodarz and N.L. Komarova. *Computational biology of cancer*. World Scientific, 2005.

[142] R. K. Wong, A. Fyles, M. Milosevic, M. Pintilie, and R. P. Hill. Heterogeneity of polarographic oxygen tension measurements in cervix cancer: an evaluation of within and between tumor variability, probe position, and track depth. *Int. J. Radiat. Oncol. Biol. Phys.*, 39:405–412, Sep 1997.

[143] J. R. Wood, S. B. Green, and W. R. Shapiro. The prognostic importance of tumor size in malignant gliomas: a computed tomographic scan study by the Brain Tumor Cooperative Group. *J. Clin. Oncol.*, 6:338–343, Feb 1988.

[144] D. E. Woodward, J. Cook, P. Tracqui, G. C. Cruywagen, J. D. Murray, and E. C. Alvord. A mathematical model of glioma growth: the effect of extent of surgical resection. *Cell Prolif.*, 29:269–288, Jun 1996.

[145] B. G. Wouters and J. M. Brown. Cells at intermediate oxygen levels can be more important than the "hypoxic fraction" in determining tumor response to fractionated radiotherapy. *Radiat. Res.*, 147:541–550, May 1997.

[146] J. Wu, S. Xu, Q. Long, M. W. Collins, C. S. Knig, G. Zhao, Y. Jiang, and A. R. Padhani. Coupled modeling of blood perfusion in intravascular, interstitial spaces in tumor microvasculature. *J Biomech*, 41:996–1004, 2008.